Stockholm University

Master Thesis

Degree Project in
Geology 60 hp

Early top-W-directed imbrication in Upper Pennine Bündnerschiefer in the eastern Central Alps

Vidar Jakobsson

Stockholm 2022

Department of Geological Sciences
Stockholm University
SE-106 91 Stockholm

Abstract

The Austroalpine domain was formed by Cretaceous top-to-the-W-directed nappe stacking. However, the Paleogene accretion that formed the underlying Pennine domain has traditionally been described by N-S movements, neglecting an E-W component. This study is set up to investigate what role E-W movements played in forming the Upper Pennine domain in the eastern Central (Swiss) Alps. A field study was conducted in the basal Upper Pennine nappe, Avers Bündnerschiefer, with the Juf Gabbro – a rigid mafic unit sitting at the base of the Avers Bündnerschiefer, as the study area. The Juf Gabbro was mapped using a five-fold deformation-intensity scheme. The Juf Gabbro's internal structure is defined by heterogeneously deformed E-W striking metagabbro lenses surrounded by calcschist. Structural data show a D1 phase of penetrative WNW-trending stretching lineation with top-WNW shear-sense indicators – marking the Juf Gabbros and adjacent calcschists main tectonometamorphic imprint. The main foliation is E-W striking and dips moderately to the NNE, and the D1 phase is then folded by subparallel to E-W trending D2 fold axes. These kinematics of the D1 and D2 phases are coherent with the early Cretaceous to Paleogene E-W kinematics of the overlying Upper Pennine and Austroalpine nappes (Platta, Arosa and Err nappes; Handy et al., 1996). The top-SE Avers-Turba mylonite zone crosscuts the E-W striking foliation, constraining the timing of the main tectonometamorphic event to older than the oldest age of top-SE shearing at > 45 Ma (Ring & Glodny, 2021).

Moreover, the top-WNW kinematics have previously been described in the Madris metabasalt (Ring & Glodny, 2021). This metabasalt has experienced blueschist metamorphism of 9 – 12 kbar and 380 – 420 °C (Ring, 1992), widely accepted as the metamorphic grade of Avers Bündnerschiefer. The Juf Gabbro show a mineral assemblage of Calcic-amphibole-talc-chlorite-epidote with no high-P relicts. The point-counting results and pale, colourless pleochroism in chlorite, epidote and Calcic-amphibole suggest an Al-Mg rich bulk composition, which is consistent with a previous study by Oberhänsli (1978). The Al-Mg-rich bulk composition is suggested for the lack of high-P relicts in the Juf Gabbro – concluding that the main tectonometamorphic imprint of Juf Gabbro occurred under blueschist facies condition.

In contrast to the rest of Avers Bündnerschiefer, the Juf Gabbro remain largely unaffected by the later orogenic events and therefore reflects the early kinematics of the entire tectonic nappe. This study suggests that top-WNW imbrication during the early Paleogene formed the Upper Pennine domain (Avers Bündnerschiefer). Avers Bündnerschiefer was already a tectonically cohesive unit once influenced by the top-N kinematics, which marks the traditional model of forming the Avers Bündnerschiefer (Schmid et al., 1996).

Contents

1. Introduction

Mountain belts form in a convergent setting by thickening the continental lithosphere, forming up to twice the thick crust in the orogen as in the surrounding continental plate. The development of an orogen involves multiple stages (e.g., subduction, continental collision, and gravitational collapse), with each stage leaving behind different tectonometamorphic fabrics. The continental-collision stage facilitates the exhumation and surfacing of rocks while retaining mineralogical and structural information from metamorphic pressure (P) and temperature (T) paths. Rocks exhume through erosion or synconvergent extension within the orogen, promoting a vertical thinning event. Several mechanisms may cause vertical thinning: (1) Thickening at the base of a convergent wedge causing a gravitational collapse in the upper crust leading to normal faulting and thinning (Platt, 1986). (2) During oblique convergence, episodical plate divergence allows for exhumation (Malusà et al., 2011), and (3) orogen-parallel spreading at mid-crustal levels during nappe stacking (Schmid et al., 1996). (4) Post-convergent modification of the newly thickened crust includes an orogen-parallel extension (Selverstone, 2005).

Lithologies' main tectonometamorphic imprints infer deformational processes. However, differences in rheology and fluid availability cause rocks to deform heterogeneously, and therefore lithologies that share the same tectonic history may retain tectonometamorphic imprints differently. An example of this kind of phenomenon was demonstrated by Régnier et al. (2003). The authors showed that parts of the metasedimentary sequence of Cine nappe in western Turkey had undergone metamorphism during Paleogene with a maximum P-T of 7kbar and > 500°C while recording top-S kinematics associated with an overlying shear zone. In contrast, the same sequence 20-30km north of the shear zone recorded a Neoproterozoic tectonometamorphic imprint with a maximum P-T of 8-11 kbar and 600 – 650 °C with top-N kinematics. This demonstrates that a tectonometamorphic overprint can be vastly heterogeneous, and some lithologies reequilibrates more readily, metamorphically and structurally, while others retain early tectonometamorphic imprints. Therefore studying different lithological entities within the same tectonic unit may reveal clues to multiple metamorphic and deformational stages in an orogenic cycle.

An orogens' tectonic history can be constrained by studying its different tectonic units (nappes). The term 'nappe' describes a resurfaced tectonic unit that has been detached from its substrate and moved considerably (>5km). Mapping nappes different lithologies' structural and metamorphic properties allows for the reconstruction of metamorphic P-T and the kinematics of the main deformational event, whose timing may be constrained through geochronological dating methods.

The Alps is a well-studied orogen where orogenic processes reveal nappe movement ranging from E-W to N-S. The current "state of the art" tectonic model for the Tertiary (hereafter referred to as 'Paleogene') development was put forward by Schmid et al. (1996). This model is based on geophysical surveying and paleogeographic reconstructions and strongly emphasises top-N/NW-thrusting sustaining material's progressive accretion into the orogenic wedge. However, the model's significant constraint is that the timing of events is restricted to the Bergell intrusion at 32-30 Ma, crosscutting nappe boundaries in the Eastern Alps.

Moreover, the model has been criticised for being two-dimensional, thus neglecting most tangential (out-of-plane) motions (Ring & Glodny, 2021).

1.1 Architecture of the Alps

The Alpine literature divides the Alps into a Western, a Central, and a Southern part, with the Jura mountains to the NW and the Austroalpine nappe complex to the Eastern Alps (hereafter referred to as ANC) (figure 1.1). This study focuses on the Central Alps – geographically bound by the Simplon fault in the west (figure 1.1), the Swiss Molasse to the north, the Austroalpine nappe complex to the east, and the Insubric Line to the south.

The primary alpine tectonic domains are introduced tectonostratigraphically from top to bottom (figure 1.1): The ANC is a part of the Adria margin. The Penninic domain underlies the ANC and comprises a heterogeneous oceanic mix (Upper and Lower Pennine) with a micro-continent located between (Middle Pennine), all accreted into orogenic wedges. Lastly, the Helvetic domain is a part of the distal European margin, forming the tectonostratigraphic base (figure 1.1).

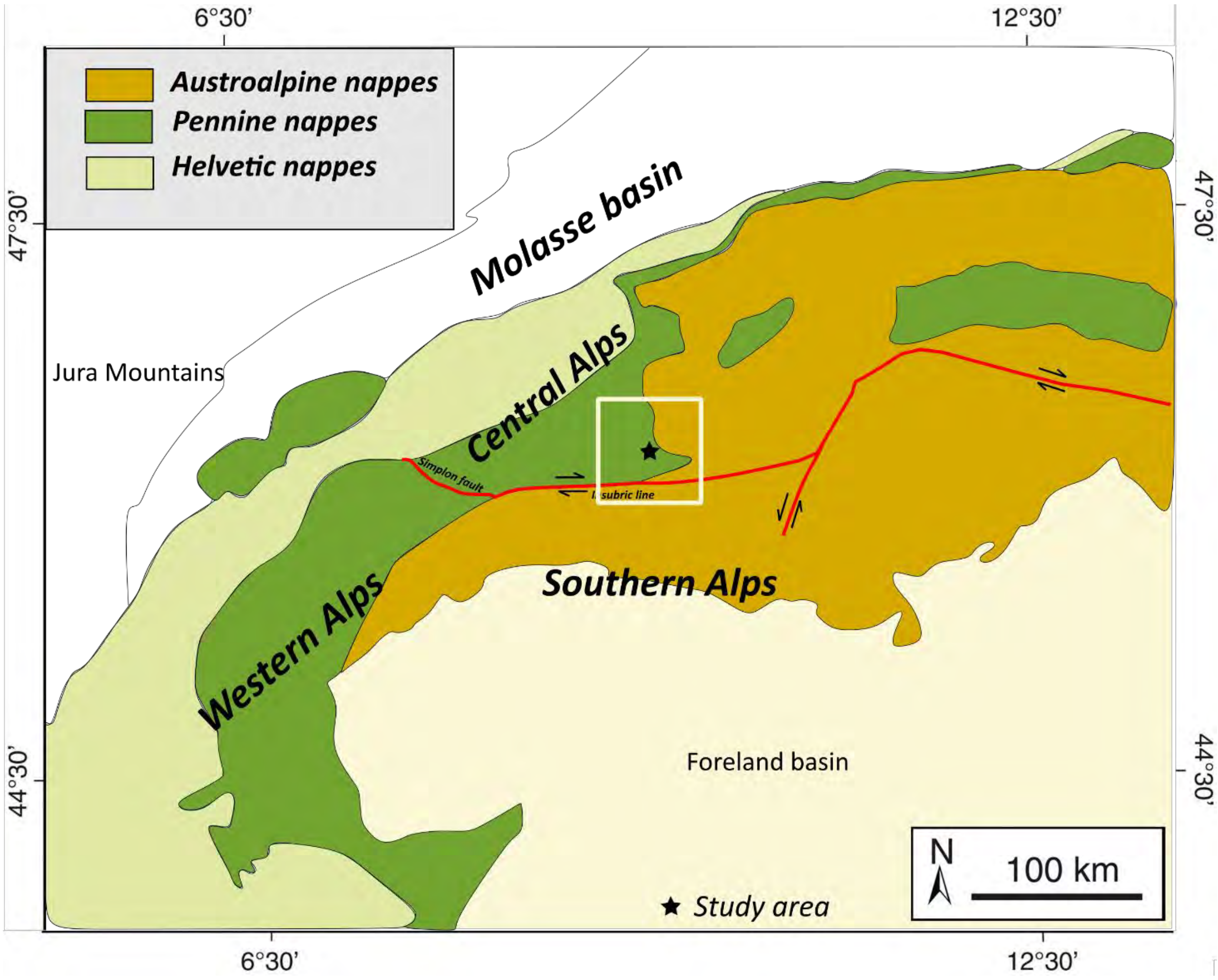

Figure 1.1 is showing the general architecture of the Alps, with figure 1.2 outlined as the white square and the study area marked as a star. Modified from Price et al.,(2018).

1.2 Formation of the Alps

The Alpine history was initiated by closing the Melliata-Hallstatt ocean (figure 1.2), forming the ANC. A subduction stage followed this, including the subduction and accretion of the Upper Pennine domain – Piemont Liguria Ocean, the Middle Pennine domain – Brianconnais microplate, and the Lower Pennine domain – Valais Ocean (figure 1.2). At last, the European margin entered the subduction zone, marking the onset of the continent-continent collision. The main events are described below in chronological order.

1.21 The Subduction stage

The Alpine story started with the closure of the Meliata-Hallstatt Ocean in the Early Cretaceous (figure 1.2) (Schmid et al., 1996). The closure caused synconvergent thrust wedge propagation toward the margin between the Adriatic and European plates, followed by orogen-parallel strike-slip movement (Dallmeyer et al., 1998) (Schmid et al., 1996). By the late Cretaceous, the ANC had formed, acting as a rigid orogenic lid for the coming events (Dallmeyer et al., 1998). The late Cretaceous ended with an extensional phase involving a series of normal faults and folding of the ANC (Schmid et al., 1996). Platt (1986) attributed the extension to a gravitational collapse caused by the over-thickened orogenic wedge. Furthermore, during the late Cretaceous hyperextended domains of the western Piemont-Liguria Ocean entered the oblique easterly dipping subduction zone under the Adriatic plate (Carminati & Doglioni, 2012) and (Mohn et al., 2014).

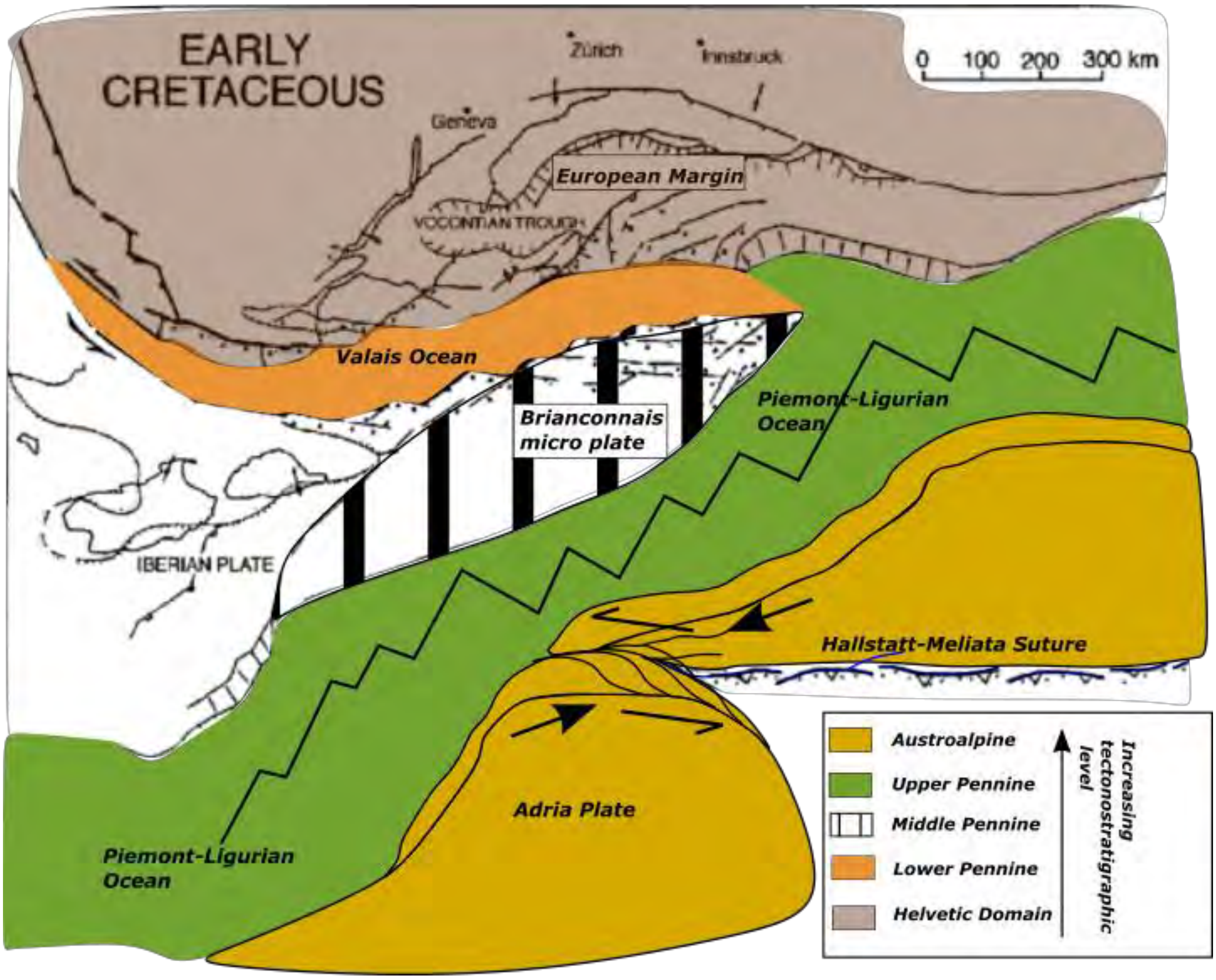

Figure 1.2 shows the position of the three oceans (Hallstatt-Meliata, Ligurian-Piemonte, and Valais Ocean) in the Early Cretaceous, by the time that Hallstatt-Meliata closed (adjusted from Chanell and Kozur 1997). The different alpine domains are illustrated in the image.

Schmid et al.'s (1996) tectonic model defines the Paleogene convergence as being dominated by N-S shortening, which formed the Pennine nappe pile due to progressive accretion against one or two low-angled, southerly-dipping subduction zones (Froitzeheim et al., 2006 and 2008). The first accretionary wedge (Upper Pennine, Avers Bündnerschiefer) formed from the closure of the Piemont-Ligurian Ocean, followed by a second wedge facilitated by the subduction and accretion of the Brianconnais microcontinent (Middle Pennine domain) and the Valais Ocean (Lower Pennine domain) under the Adriatic plate during Paleocene (Schmid et al. 1996) (Price et al. 2018) (Ring, 1992). Remnants of the Piemont-Ligurian and the Valais oceans are seen as subducted slabs beneath the Adriatic microplate in the tomographic images by Lippitsch et al. (2003).

1.22 The continental collision stage

The continental collision was initiated by the subduction of the distal European margin (Helvetic domain) in the Early Eocene (~ 50 Ma) (Schmid et al., 2004), with the Adriatic plate overriding the European margin. This convergence involved oblique N-S shortening inferred by the N/NW thrusting at the insubric line (figure 1.1) (Schmid & Kissling, 2000). The oblique convergence was more significant in the Central Alps than in the Western Alps, resulting in the western plate's periodic divergence away from the trench. Malusà et al. (2015) suggest that the plate divergence influences the high-pressure units' exhumation.

Since the mid-Paleogene, the major tectonic events have been driven by radiogenic heat, causing a barrovian metamorphic overprint of the Pennine zone and promoting the Adriatic indenter to move north and modifying the orogen through (1) Strike-slip faulting along the Southern Alps margin; (2) fold and thrusting to the north in the Jura Mountains (Ring & Glodny, 2021; Price et al., 2018).

1.3 Tectonic setting of the eastern Swiss Alps

This report will focus on the eastern Central Alps, with the study area being the Avers Bündnerschiefer in the south-eastern Swiss Alps. Below, the relevant unit's lithologies are described from top to bottom in the following order: The ANC, the Austroalpine-Upper Pennine suture, the Upper Pennine unit focusing on the Avers Bündnerschiefer, and a brief introduction to the Middle and Lower Pennine units.

The ANC (figure 1.2) comprises a Mesozoic cover sequence resting noncomformably on a crystalline voluminous silicic to intermediate Variscan orthogneisses. The Err nappe is a distal part of the ANC which comprises mostly shales, limestones and sandstone (Handy et al., 1996). These sequences were deformed by crustal-scale transtensional strike-slip faulting that juxtaposed crustal and mantle structural levels during the northwest Adriatic passive margin formation in the Mesozoic (figure 1.2) (Price et al., 2018). The boundary between the Autroalpine and Pennine domain comprises the Arosa unit (figure 1.3): A chaotically faulted tectonic melánge composed of imbricate slices of Austroalpine, Upper and Middle Pennine rocks in a matrix of Upper Pennine origin – making up the suture between the Pennine and Austroalpine domains (Price & Wernicke, 2022) (Ring & Glodny, 2021). It stretches 400km N-S to strike, and the north-south structural overlap is exposed along nearly 150km in eastern Switzerland (Price et al., 2018).

The Upper Pennine domain (figure 1.2) comprises Piemont-Liguria crustal and sedimentary elements modified during the Late Cretaceous to early Paleogene Subduction. Underlying the Arosa unit lies the Platta nappe comprising pillow basalts and limestones (Schmid et al., 2004). This study focuses on Avers Bündnerschiefer, directly underlying the Platta nappe, which comprises an extensive sequence of calcschists intercalated with serpentine, tholeiitic to alkali metagabbroic and metabasaltic rocks, and marble (Oberhänsli, 1978).

The Middle Pennine domain is derived from the Brianconnais microcontinent (figure 1.2). It comprises a Paleozoic crystalline basement (preserved in the Tambo-Suretta nappe) with a detached Paleozoic to Mesozoic cover of various platform sediments which forms the Schams and Falknis nappe (figure 1.3) (Schmid et al., 2004). The Schams nappe is wrapped around the front of the Tambo-Suretta nappe and squashed between the Platta and Avers nappe, traditionally interpreted as the Niemet-Beverin fold (Schmid et al., 1996). The Lower Pennine domain is derived from the Valais Ocean with deposits grading from late Cretaceous calcschist (Valais Bünderschiefer) to Paleogene North Pennine flysch with most deposits lacking Mesozoic oceanic lithosphere (figure 1.3) (Schmid et al., 2004). The southern margins of Tambo and Suretta got truncated by the Bergell intrusion in the early Oligocene (Gianola et al., 2014). Moreover, northwest of the Upper-Pennine nappes lies the Engadine line (figure 1.3), associated with NE extension and sinistral strike-slip between Bergell intrusion and St Moritz (Ring & Glodny, 2021).

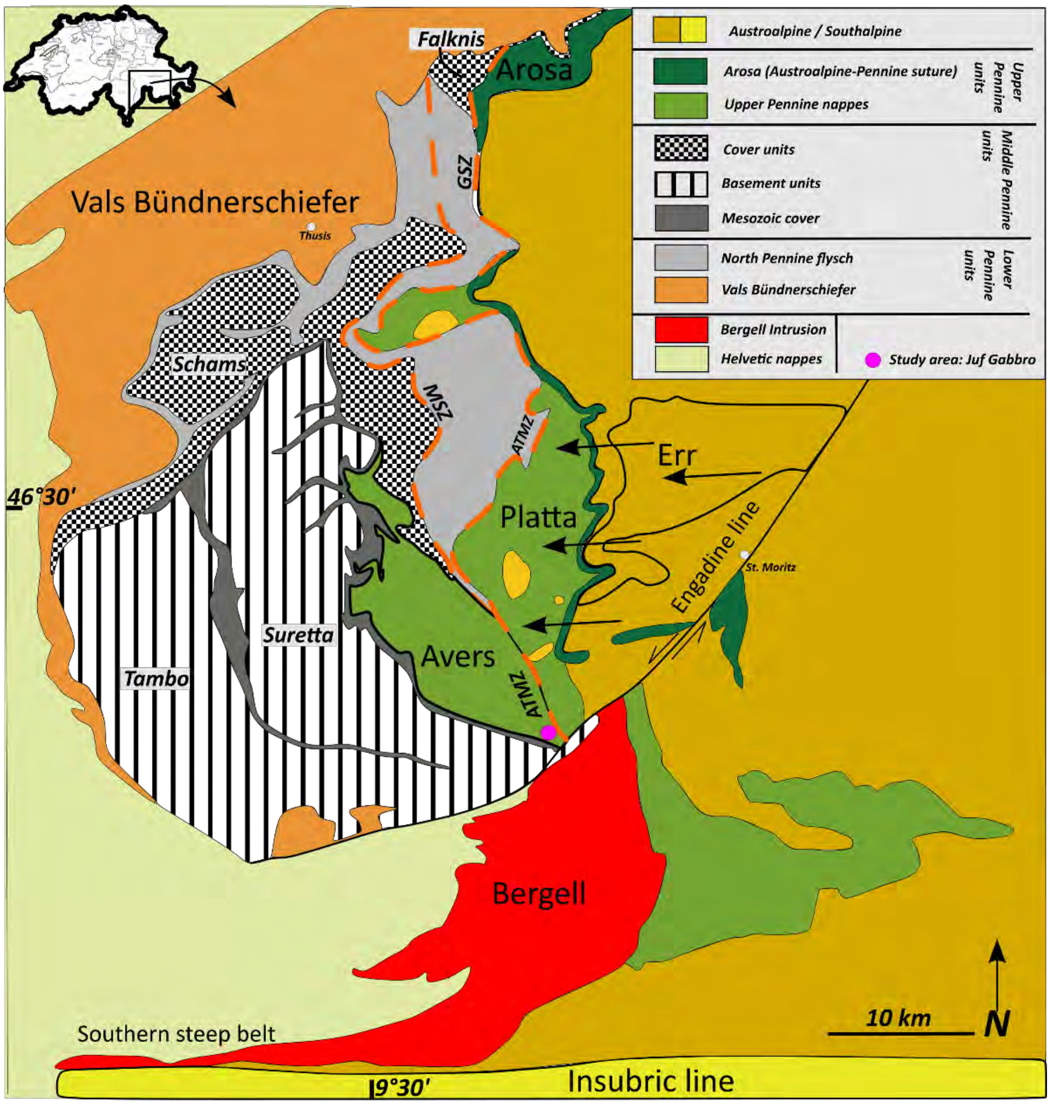

Figure 1.3 is a schematic drawing of the tectonic setting of the SE Swiss Alps (modified from Ring & Glodny, 2021 and Handy et al., 1996). The arrows are showing were tangential W-kinematics have priviously been described. The following major shear zones are shown: Turba-Avers mylonite zone (TAMZ), Martegnas shear zone (MSZ), and Gürgaletsch shear zone (GSZ) – which all show similar kinematics (Ring & Glodny, 2021).

1.4 Tectonometamorphic development of the eastern Swiss Alps

The earliest tectonometamorphic imprint of Alpine origin reflects the kinematics from the late Cretaceous top-W/WNW imbrication in the Adriatic plate (Dallmeyer et al., 1998). This phase exhibits W/WNW trending stretching lineations with top-to-the-W/WNW shear-sense indicators, which have been described in the Err, Arosa, and Platta nappe (Handy et al., 1996; Liniger & Nievergelt, 1990): Deformation in the Err nappe (figure 1.3) occurred under greenschist facies conditions with an estimated peak P-T of ~ 7kbar-300°C dated at 76-89 Ma (Handy et al., 1996). The trend of the stretching lineation is parallel with shallow-to-steeply-dipping E-W-trending fold hinges with N-dipping axial planes (Liniger & Nievergelt, 1990) (Handy et al., 1996). In the Arosa unit, the deformation is dated to roughly 50 Ma – interpreted as the late recrystallisation age of late top-W/WNW-directed imbrication (figure 1.3b) associated with the abandonment of the suture zone and fluid activity (Bachmann et al., 2009). Furthermore, the uppermost Pennine units (figure 1.3), Platta and Arosa, demonstrate low-grade metamorphism, increasing from N (~ 3 kbar, 250°C) to S (~5kbar, 350°C) (Trommsdorff & Evans, 1974) (Handy et al., 1996). The Err, Arosa, and Platta nappe's foliation is E-W striking, is cataclastically penetrated by a 40°-to the north-dipping fault system with an earlier N-thrusting component and an older sinistral extensional fractures in the Platta nappe (Liniger & Nievergelt 1990).

The Platta nappe is separated from the underlying Avers Bündnerschiefer by the top-SE displacing Avers-Turba mylonite zone (hereafter referred to as ATMZ, figure 1.3), causing a significant P-break of a minimum 9 kbar and a thermal gradient shift from <10°C/km to > 20°C/km (Ring & Glodny, 2021). This shear zone consists of mylonitic calcschist exhibiting SE-trending stretching lineations with top-to-the-SE shear-sense indicators. It stretches from the highly deformed contact between the Avers Bündnerschiefer and Schams nappe to the peak of Piz Turba (figure 1.3) – where it is folded by the ongoing N-S shortening (figure 1.5) (Liniger & Nievergelt, 1990; Ring & Glodny, 2021). These top-SE-kinematics are also described at the eastern boundary of the Schams nappe, bordering the ATMZ, and continuing into the Martegnas shear zone in the northeastern Schams nappe (figure 1.3) (Ring & Glodny (2021). Ring & Glodny (2021) noted that the top-SE-kinematics are subparallel to the axes of the isoclinal folds, which had previously been correlated with the Niemet-Beverin backfold by Schreurs (1993). Ring & Glodny (2021) interpreted the top-SE-kinematics as the return flow of the Pennine domain within the subduction channel along the upper backfolded limb (figure 1.4c) and dated the top-SE-kinematics to 45 – 34 Ma, constraining the age of the backfolding event. Furthermore, they note that the folds' upper contact must have been normal to the Earth's surface, making the ATMZ incompatible with the backthrusting model proposed by Schmid et al. (1996) – who attributed the backfolding to the N/NW-thrusting of the insubric line. The N-dipping mylonites associated with dextral strike-slip motion at the southern steep belt, south of the insubric line, infer this thrusting. Liati et al. (2000) dated acidic dykes crosscutting this mylonitic belt to 25 – 23 Ma, interpreting it as the end of the ductile thrusting.

The mafic rocks of Avers Bündnerschiefer, including the Juf Gabbro, have been studied by Oberhänsli (1978): The Juf Gabbro is described as an alumina-rich metagabbro, rich in epidote and clinozoisite, but exhibits igneous relics of porhyroclastic augite reflecting a deficiency in fluid availability. The 70 by 100-metre wide metabasalt in the Madris valley shows a glaucophane-garnet ± chloritoid mineral assemblage. This assemblage and high-Si phengite demonstrate that the Avers Bündnerschiefer experienced blueschist facies metamorphism at a mininum of 9-12 kbar and 380-420°C (Ring, 1992 and Engi et al., 2004). Furthermore, thin sodic-amphibole bearing lenses with sharp contacts appear within the retrograde-greenschist-calcschist. Oberhänsli interprets these sodic amphibole-bearing lenses as meta-tuffs. The meta-tuffs higher Fe^{3+} content promotes the stability of sodic amphiboles (riebeckite) in upper greenschist conditions (Oberhänsli, 1978 and Manzotti et al. 2020). Ring & Glodny (2021) describe the Madris-metabasalt and the Juf Gabbro as recording W-trending stretching lineation associated with top-to-the-W shear-sense indicators. However, the trend of the stretching lineations scatters from E-W to NW-SE-trending with Top-to-the-NW shear-sense indicators (Ring & Glodny, 2021). These E-W kinematics are neglected by the tectonic model of Schmid et al. (1996), which argues for the formation of Avers Bündnerschiefer by N-S shortening. The earlier E-W striking foliation is cut by the ATMZ (figure 1.5) and is, therefore, > 45 Ma in age. At the same time, the contact between Piz Turba and the Juf Gabbro has been

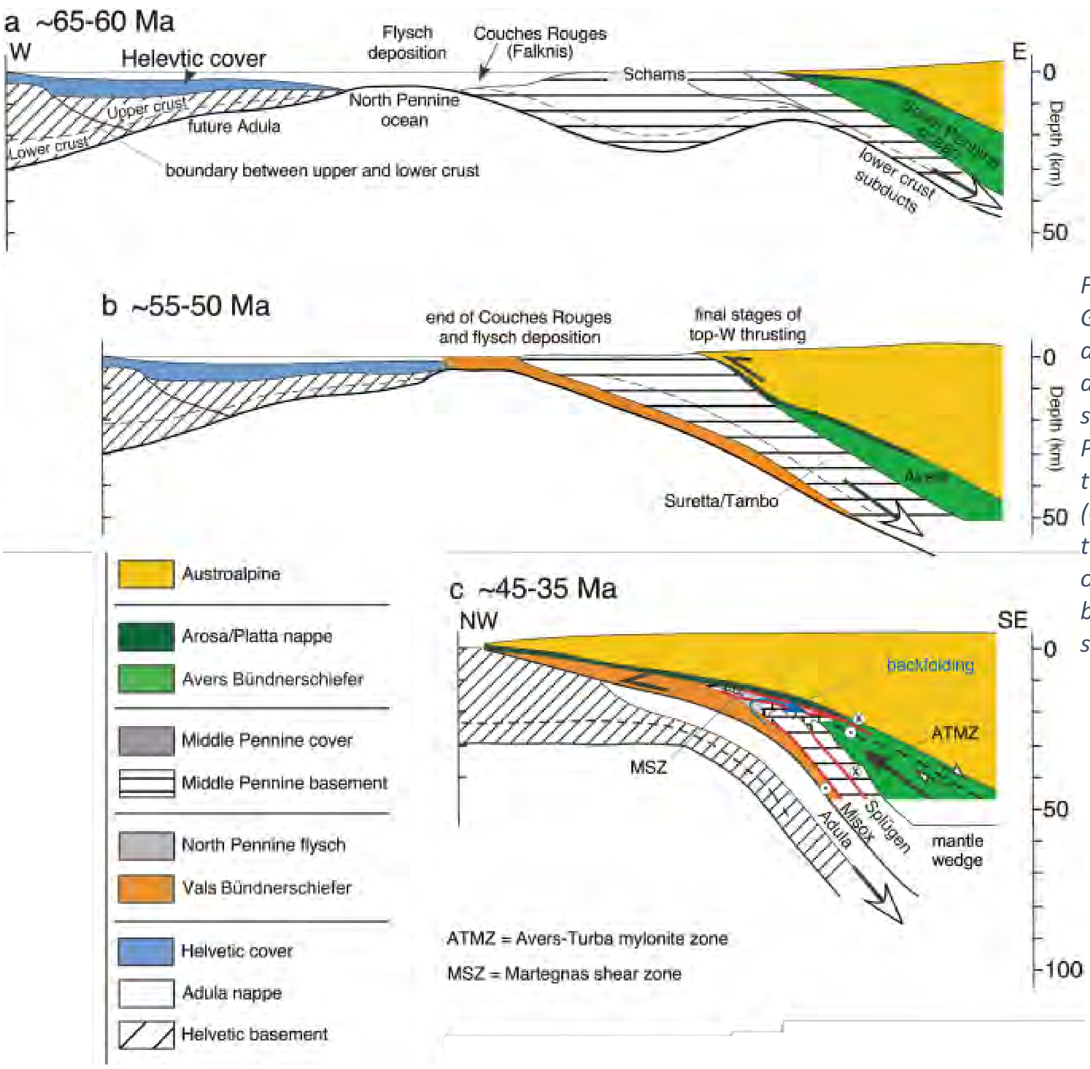

Figure 1.4 modified from Ring & Glodny (2021). Marking the different deformational stages of the Paleogene alpine history. (A) are showing the subduction and accretion of Upper Pennine units causing imbrication through top-W thrusting shown in (B). (C) marks the initial juxtaposition of the Austroalpine, and Pennine domain over the Helvetic domain causing the backfold associated with the top-SE shearing of ATMZ.

overprinted by a steeply NE-dipping dextral-oblique-slip normal fault providing an E-W extension (Ring & Glodny, 2021).

Price et al.'s (2018) analysis of cooling ages showed that a significant portion of the Pennine domain in the Central Alps exhumed during the main phase of the Alpine nappe development between ~ 35 – 18 Ma by normal-sense movement relative to the Austroalpine allochthon. The authors demonstrated a minimum displacement of 70 km between the Pennine footwall and the Austroalpine hanging wall. The displacement is suggested by Ring & Glodny (2021) to be accomplished by the top-SE ATMZ (responsible for 40 km), Martgnas shear zone, and Gürgeletsch shear zone for the remaining 30 km. The recent literature by Price & Wernicke (2022), Price et al. (2018), and Ring & Glodny (2021) reinforce a hypothesis that the juxtaposition of the Pennine domain to the Austroalphine domain was caused by top-SE shearing (45 – 35 Ma) and top-E normal faulting (35 – 30 Ma), contrasting the previous top-N thrust motion implied by Schmid et al. (1996).

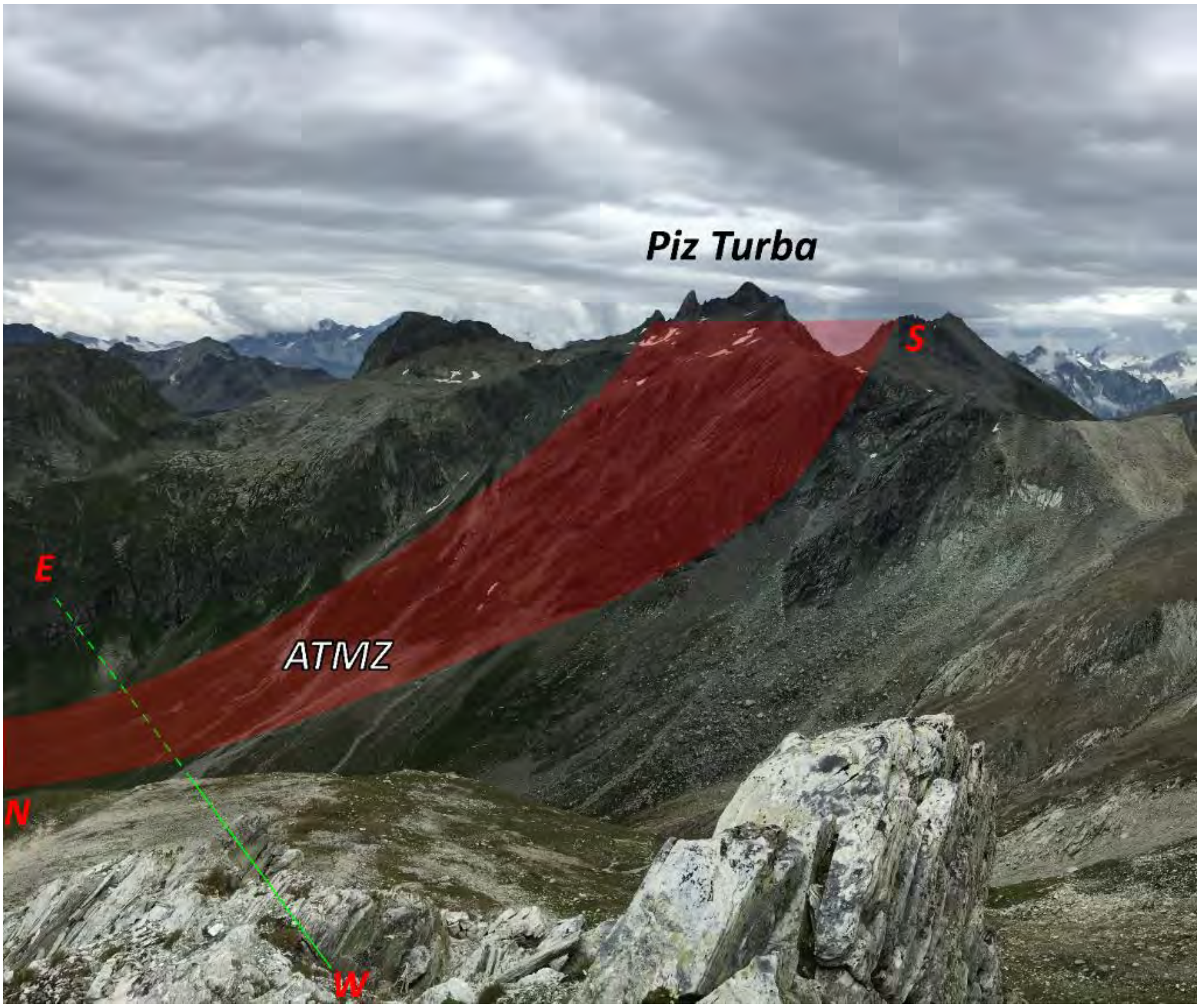

Figure 1.5 (photograph credit: Uwe Ring). The image is showing how Juf Gabbro's foliation is striking E-W (shown in green) and is crosscut by the top-SE-displacing ATMZ (shown in red). The ATMZ is folded towards the peak of Piz Turba.

1.5 Aim

The overarching aim of this study is to investigate how important tangential (out of plane) motion is for the Alps. More specifically, how far the Late Cretaceous to Early Paleogene top-W/WNW kinematics reaches down the tectonic pile. Are these early Alpine kinematics recorded in the Avers Bündnerschiefer? The rigid, fluid deficient Juf Gabbro – marking the base of the Avers nappe, was chosen as the study area with the assumption that it is less likely to be overprinted by later events (mainly the ATMZ, figure 1.5). Therefore, constraining Juf Gabbro's main deformational phase and assessing the metamorphic history will answer to what extent the top-W/WNW-directed imbrication is associated with the formation of the Upper Pennine Avers Bündnerschiefer. Furthermore, this study aims to map Juf Gabbro's internal architecture and whether its precursor rock includes one or several bulk compositions through a field study and a quantitative petrographical analysis.

2. Method

The field study was conducted by mapping out and describing the lithologies and their structural and contact relations while measuring the following structures with a compass: stretching lineation (trend and plunge), foliation (dip and dip-direction), Folding; axial plane (dip and dip-direction), fold axes (trend and plunge), faulting; fault planes (dip and dip-direction); and slicken striations (trend and plunge). Several measurements were recorded on each outcrop, whereof a representative average is reflected as a single measurement on the field map. Each outcrop's coordinates (longitude, latitude, and elevation) were retrieved through the GPS on a mobile phone device. Shear-sense data was obtained by analysing shear-sense indicators on surfaces parallel-to-subparallel to the stretching lineation. If an outcrop exhibited several shear-sense indicators, the displacement was determined by the sum of all indicators. All samples exhibiting stretching lineations were oriented before being removed from the outcrops by using a hammer and a chisel, to be later made into an oriented thin section.

The petrographic analysis was conducted with the help of a Nikon Eclipse E200 microscope and a PELCON Automatic Point Counter. Mineral modes were point counted using a sampling distance of 500µm for all thin sections besides sample MB2, in which thin layers were carefully point counted using a 100µm sampling distance. Moreover, samples containing mylonitic foliation and carbonate+quartz-boudins were point counted separately in thin sections, to be later compared to a ratio of boudinage-to-matrix determined by point counting an image of the outcrop. The mineral modes resulting from the point counting were then converted into a molar proportion of each oxide using the stoichiometry of solid-solution end-member compositions provided by Holland and Powell (1998). Mg-end members were used for calcic-amphiboles, chlorite, and clinopyroxene, whereas Al-end members were used for the epidote group.

The structural data were analysed using equal area stereonet projections provided by IOGAS software. A field map was produced using the structural data, a semi-quantitative deformation intensity scheme (detailed in the result section) and lithological contact tracing. Dip data was converted into an apparent dip before being projected on a crossection. Deformational processes were inferred from the measured structural data.

3. Results

3.1 Study Area

The Study area is in SE Switzerland, at the end of the valley in Avers, Juf. The area is roughly 3km by 1.4km around the origin of the Juferrein, east of Juferhorn, Grauhörner, and Piotjoch. Field mapping resulted in the map (figure 3.1), where colours indicating lithologies and deformation intensity are drawn schematically, and each data point represents an outcrop. The colours showing the lithologies and deformation intensity stay consistent between the map and cross-sections. Some areas lack data density due to steep topography, rockfall cover, soil cover, or time for the project's scope.

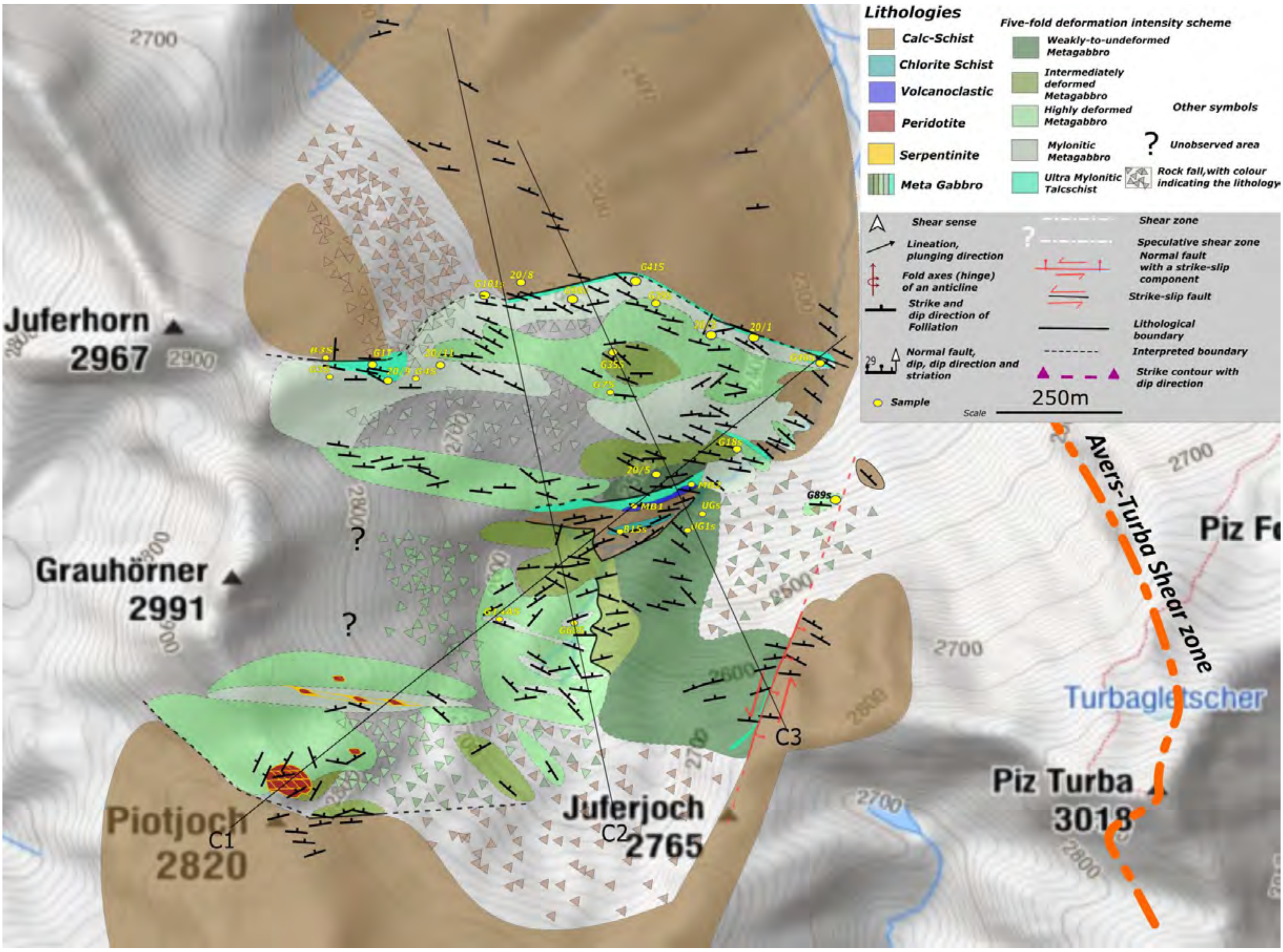

Figure 3.1. The field map with strike and dip-direction measurements of the foliation. Cross-sections 1-3 are shown on this map. Each data point on the map represents an outcrop, whilst the lithological and deformation-intensity zones along with their boundaries are schematically drawn where it lacks a thick, sharp boundary. The peridotite lenses SE of Grauhörner represents schematically show a boudinaged peridotite horizon within highly deformed to mylonitic metagabbro.

3.2 Lithologies

In this chapter, the four different lithologies will be introduced. The metagabbro covers the central part study area, with a peridotite located at Piotjoch in the SW, a metavolcanic layer in the middle, and the metagabbro is surrounded by a calcschist (figure 3.1). The different rock types are detailed below.

3.21 The metagabbro and the five-fold semi-quantitative deformation scheme

The metagabbro covers the most significant part of the study area (figure 3.1), surrounded by calcschist at the N, S, and SE contacts. The metagabbro is heterogeneously deformed and varies drastically in appearance depending on the deformational intensity. Hence, rocks of various deformational intensities are described to better understand the Juf Gabbro deformation. Below the five-fold semi-quantitative deformation intensity scheme is introduced:

- The weakly-to-undeformed metagabbro (figure 3.2a, b, and c) is greenish to pale-yellow with varying degrees of carbonation defined by a fine-grained sheen.
- The intermediately deformed metagabbro (figure 3.2d) shows a layering of a light greenish-yellow centimetre-scale foliation, separated by massive bodies of weakly deformed metagabbro (10 – 100 centimetres in thickness). Thereof intense deformation is concentrated in 10 – 20-centimetre-thick zones between the weakly deformed zones, noting the metagabbro's heterogeneous deformation. In the foliated zones, lineation is visible and measurable.
- The highly deformed metagabbro (figure 3.2e and f) has a laminated foliation with a fine-grained light yellowish-green stretched fabric with visible amphibole and quartz crystals and sheared boudins of carbonate and quartz. The rocks carbonate chemically weathers in a pitted way, containing centimetre-scale holes of eroded carbonate and quartz boudins.
- The mylonitic metagabbro (figure 3.2g and h) is a fine-grained rock, white to very light tones of green in colour with a tight millimetre-scale foliation. White, highly stretched plagioclase aggregates form a prominent lineation. Some layers include pitted weathering and sheared carbonate boudins.
- The ultra-mylonitic talc-schist is a fine-grained turquoise rock with a penetrative stretching lineation (figure 3.2h). It only outcrops at the contact between the metagabbro and calc-schist layers and is often covered by soil. The talc-schist deforms easily, splits well, and is scratchable by fingernails (figures 3.2h and 3.3h).

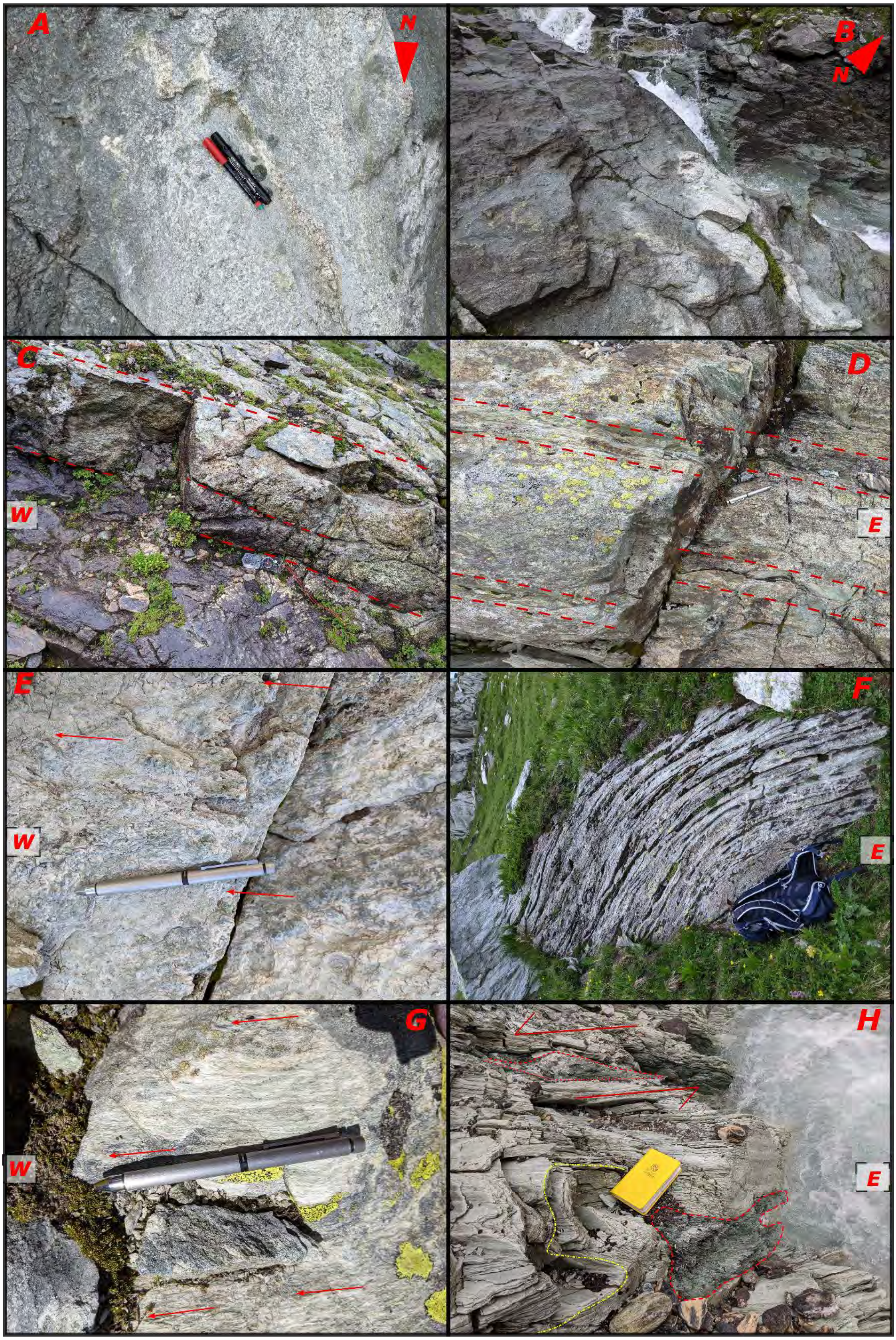

Figure 3.2. Field images demonstrate examples of the deformation intensity scheme. Image A and B are undeformed metagabbro. Image C is an example of a massive, weakly deformed metagabbro, showing distinguishable foliation planes. Image D is intermediately deformed, determined by the section of well-defined foliation planes separating the more massive parts. Image E is looking onto a foliation plane of the highly deformed metagabbro, here, note the visible porphyroblasts. Image F shows the foliation plane thickness of the highly deformed metagabbro. The arrows in E show the stretching lineation. Image F shows the tight foliation planes with pitted weathering, indicating the past presence of carbonate clusters. Both G-H details mylonitic metagabbro fabrics; image G arrows show how the stretching lineation is expressed on the tightly foliated planes. Image H show ultra-mylonitic lenses of talc schist (emphasised with red) within a folded mylonitic chlorite-rich metagabbro.

Calcschist

The brown calcschist exhibits a penetrative foliation, forming deformed zones between sheared boudinaged clusters of carbonate and quartz aggregates. These boudins range from 1 centimetre to 10 centimetres in width and are up to 4-centimetres-thick (figures 3.3a-b). The calcschist exhibits a mylonitic texture with quartz aggregates expressing the lineation at all locations and is outcropping at every contact with the metagabbro and within it as an isolated slice. The isolated calcschist slice includes a 3-metre-thick greenish layer with millimetre-scale foliation planes and continuous bands of folded carbonate and quartz aggregates (figure 3.3c).

The meta-volcanoclastic rock

The meta-volcanic outcrops a 3-metre-thick-200-metre-long lens, tectonically on top of the isolated calcschist slice. It is a highly deformed, fine-grained rock that exhibits a fine-grained blueish sheen with a micaceous sheen on each foliation surface. Parts of the meta-volcanic have millimetre-thick dark-green bands separating the centimetre-thick blue layers.

Peridotite

In the SW part of the field area, just NE of Piotjoch, a massive 40 by 40 metres body of rusty-dark-brown peridotite is outcropping at the southern end of the metagabbro (figure 3.3d). The peridotite is bounded by 10-centimetre-thick bands of thoroughly lineated dark green mylonitic serpentinite (figure 3.3e). These bands also penetrate the massive peridotite separating it into 4-metre-wide undeformed pods. The contact around the peridotite is traceable around its north, west, and eastern side. In contrast, the southern boundary is masked by a 4-metre-wide path between the peridotite and the calcschist.

Just north of the massive peridotite body, about 3-metre-thick peridotite and serpentine boudins are outcropping within the highly deformed and mylonitic metagabbro. These boudins are stretched-out layers of peridotite with serpentine layers asymmetrically shaping their contact with the metagabbro. In a mylonitic part of the metagabbro surrounding Grauhörner (figure 3.1), these boudins form a layer with metre-thick serpentine connecting the peridotite boudins (figure 3.3f).

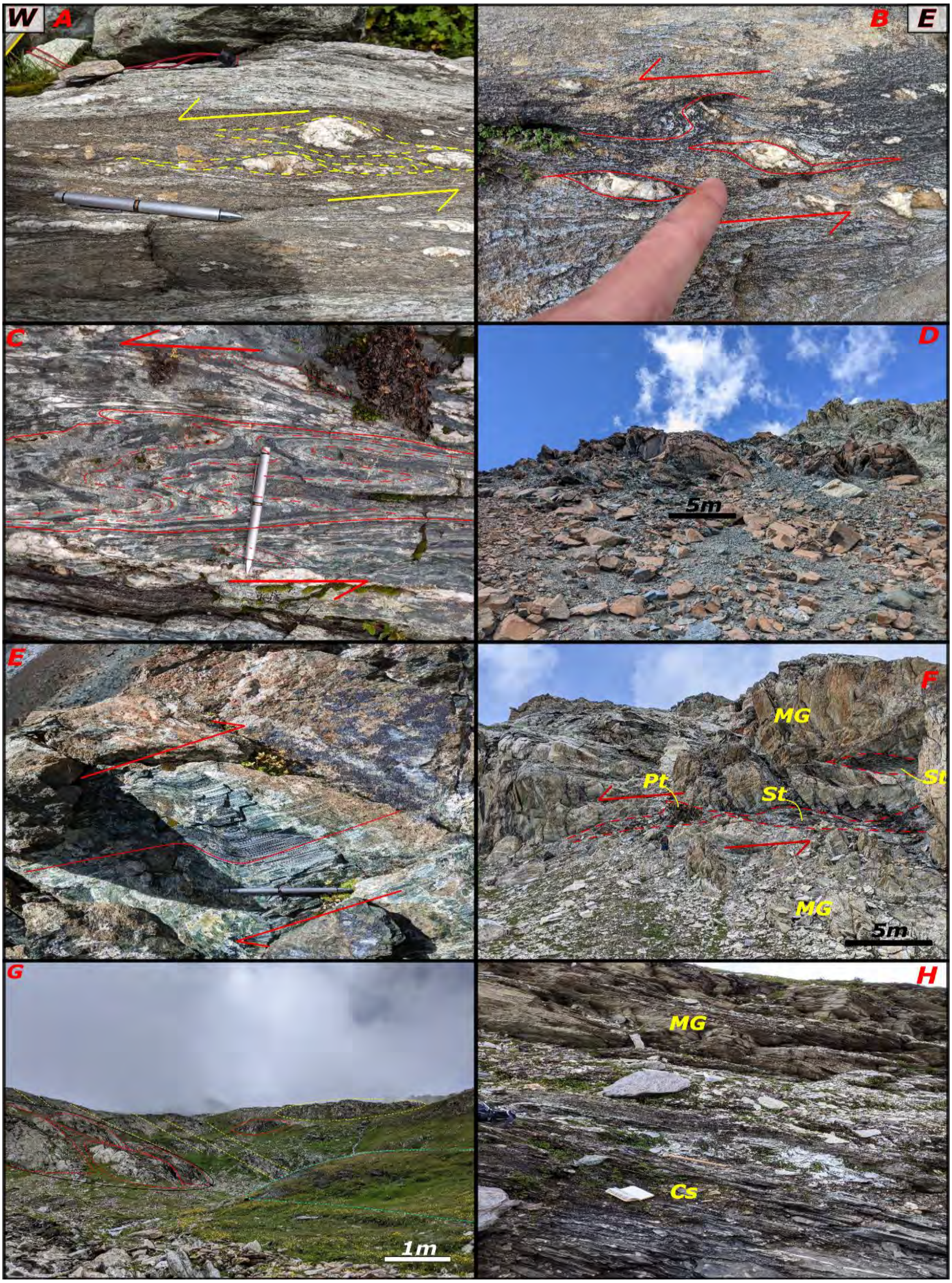

Figure 3.3. Field images of the different lithologies, shear-sense and lithological contacts. Bedrock annotations: MG = metagabbro, Pt= peridotite, St= serpentine, and Cs= calcschist. Figure a-b shows top-W sheared boudins of carbonate and quartz aggregates inside the calcschist. Figure c shows the chlorite schist with its sinistral (top-W) shear folded layers of quartz and carbonate aggregates. Figure d is an image of the massive peridotite located at Piotjoch. Figure e is a closer look at the mylonitic serpentine reflecting a dextral (top-NE) shear-sense, observed on top of the massive peridotite body north of Piotjoch. Figure f shows the layer of boudinaged peridotite reflecting top W shear-sense (Uwe Ring for scale). Figure g shows a field view (looking NNW) of the lensiodal pattern that is heterogeneously distributing the various metagabbro deformation intensities. Lenses are distributed with highly deformed foliation planes (yellow) in between; red dotted lenses are intermediately deformed, yellow is highly deformed, and turquoise is the ultra-mylonitic talc schist. This area is schematically drawn in cross-section 2 (figure 5). Figure h shows the contact between the calcschist with the metagabbro on top at the north-eastern contact.

3.3 Macroscopic Analysis

This chapter will introduce the large-scale features in the study area. The general geometry of the Juf Gabbro will be introduced and explained by the schematic cross-sections (figures 3.1-3.4).

3.31 Overall Architecture of the Juf Gabbro

The general architecture of the study area is dominated by an about 40° to-the-N-dipping gabbro body (Juf Gabbro) surrounded by calcschist. At the southern boundary of the gabbro body at Piotjoch (figure 3.1) is a rather large peridotite lens, which forms the Juf gabbro's tectonic base, shown in cross-section 1 (CS1) (figure 3.4). The most expansive mylonitic area is observed near the calcschist contact in the northern part of the study area, shown in cross-sections 2 and 3 (figures 3.5 and 3.6). Towards the southeast, the field area is cut by an oblique fault, the Juferjoch fault, which is assumed to be dipping steeply towards the east and is separating metagabbro and calcschist. The Juferjoch fault is visualised in the cross-sections CS3 and CS4 (figures 3.6 and 3.7) as a sharp boundary that crosscuts the foliation, stretching lineation, and folding.

The deformation intensity scheme applied while mapping the metagabbro shows a lensoidal pattern of heterogeneously deformed bedrock, highlighted in the cross-sections (CS1-CS4, figures 3.4-3.7). The weakly-to-undeformed and intermediately deformed metagabbro lenses are protruding as tall, 1-to-10-metre-wide blocks with steeply dipping foliation planes. The space between these massive blocks is occupied by lenses of highly deformed or mylonitic foliation planes, absorbing most deformation (figure 3.3g). These lenses are discontinuously outcropping in the field with lenses of different deformation intensity outcropping adjacent to one another, all extending in the E-W direction.

Amidst these heterogeneously deformed metagabbro lenses, there is an E-W striking, 400-metre-long and 20-metre-thick lens of mylonitic calcschist outcropping (figure 3.1) with a thin layer of meta-volcanoclastic rock lying on top: collectively, I will hereafter refer to these two lenses as 'the slice'. The slice is located in the central part of the Juf gabbro as a sheared-out lens, between undeformed-to-intermediately deformed metagabbro lenses with a talc-schist layer tectonically on top of it. This complexity is schematically visualised in the cross-sections CS2 and CS3 (figures 3.5 and 3.6). The central part of the metagabbro is where the heterogenuity of the lensoidal pattern is ubiquitous, with rocks of various deformation intensities occurring next to each other. This pattern is further explored in CS4, drawn parallel to the stretching lineation (figures 3.7 and 3.8). Many mylonitic rocks accommodate the space between the more massive (weakly-to-intermediately deformed) metagabbro, preserving parts of the more pristine gabbro (figures 3.7).

The cross-sections, CS2 and CS3 (figures 3.5 and 3.6), show the relative proportion of mylonitic metagabbro increasing from the calcschist slice towards the northern contact east of Juferhorn (figure 3.1). They also extenuate how the area is categorised by a low proportion of highly-to-intermediately-deformed metagabbro lenses extending E-W within a mylonitic metagabbro matrix. The contact between mylonitic and the highly deformed metagabbro is seldom exposed, making the area in between unknown. This is circumvented by assuming that the more easily eroded, porous, mylonitic material represents most of the area covered by grass. Regardless of whether that assumption is valid, the deformation intensity increases towards the northern contact. The northern contact encompasses the thickest-most-continuous ultra-mylonitic talc-schist layer stretches from the peak SE of Juferhorn to the river in the east (figure 3.1). This ultra-mylonitic talc-schist is only observed bordering the calcschist and the metagabbro.

At the eastern contact (figure 3.3h), thick WNW-ESE striking segments of highly-deformed-to-mylonitic metagabbro are tectonically intercalated with the calcschist. The shearing of both lithologies causes their juxtaposition as the softer calcschist is more easily deformed and therefore fills up the space between the gabbroic lenses, making the contact appear folded (figure 3.4). Due to the grass cover, the contact between the two lithologies is not outcropping uphill (figure 3.1).

The southern side of the study area (south of the slice) has suffered less intense deformation reflected by a higher proportion of massive undeformed-to-intermediately deformed metagabbro (figure 3.1). This is further extenuated by the calcschist-metagabbro contact at Piotjoch being intermediately deformed and lacking a ultra-mylonitic talc-schist layer (figure 3.4). A small proportion of mylonitic lenses are observed in the highly deformed metagabbro at the slope N of Juferjoch (schematically shown in figure 3.5) and NE of Piotjoch, associated with peridotite boudins bounded by mylonitic serpentine (figure 3.4).

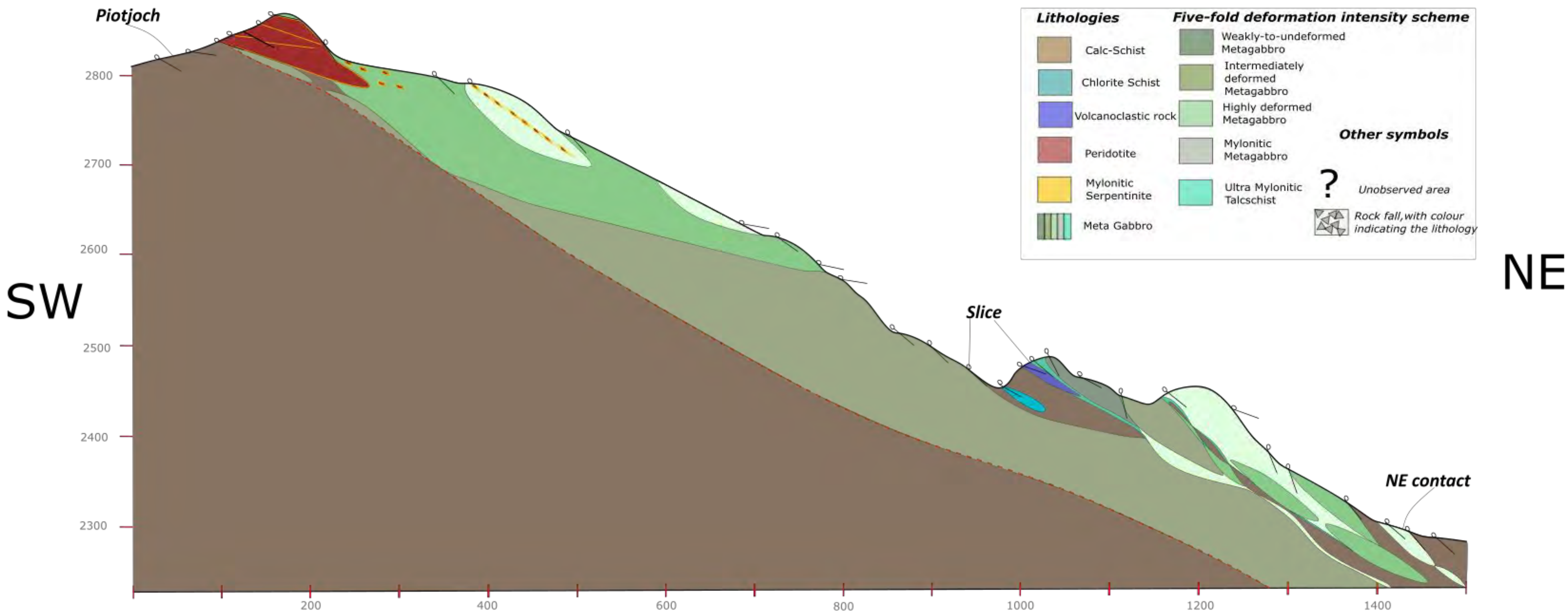

Figure 3.4. Cross-section 1 (CS1). The complex nature of heterogeneously deformed rock outcropping adjacent to another in the study area is visualized through sheared out the lensiodal structure. In the NE, the intercalation of the contact is visualized by small, sheared lenses of mylonitic calcschist and ultra-mylonitic metagabbro sheared into the main gabbroic body from the NE contact. Here, the calcschist is shearing into the metagabbro with talc layers bordering the metagabbro. The central meta gabbroic body is intermediately deformed, whereas the degree of deformation sharply increases towards the SW and NE boundaries. These highly deformed and mylonitic layers appear as E-W stretched out lenses. The peridotite is marking Juf Gabbro's tectonic base in the SW (but topographically on top) as a brittle massive-undeformed-pod - bounded by mylonitic serpentine layers. Moving northwards, there is a boudinaged peridotite horizon within mylonitic metagabbro, indicating top W movement (figure 3f). The slice is tectonically imbricated into a weakly deformed metagabbro surrounded by a plethora of metagabbro lenses of different deformational intensities. This is the most complicated part of the metagabbro with weakly deformed metagabbro juxtaposed mylonitic intensities towards the NE. All these lenses are striking E-W.

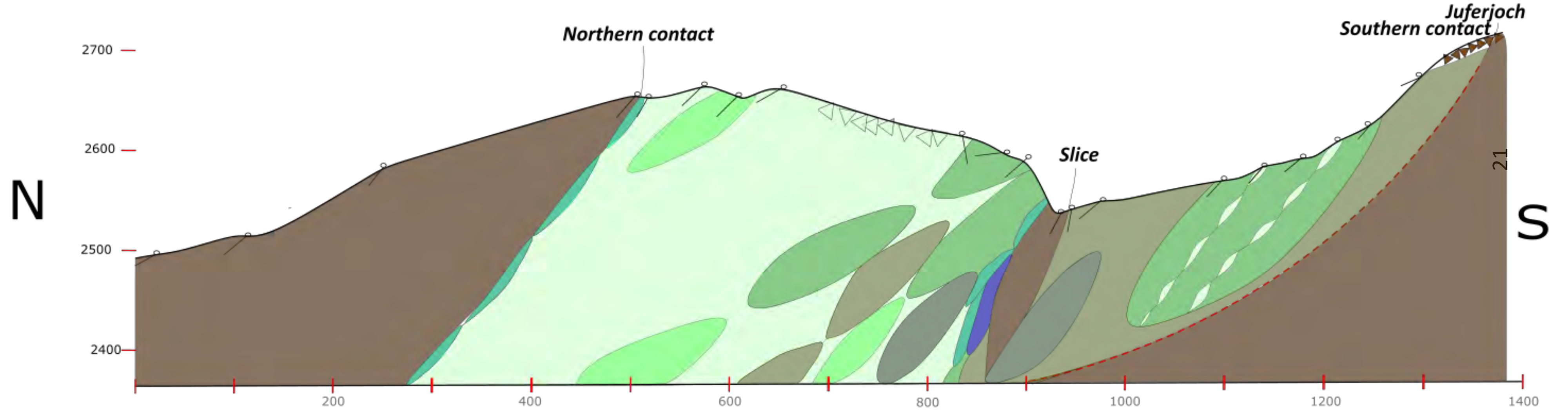

Figure 3.5. Cross-section 2 (CS2) is oriented N-S emphasises the deformation intensity increase towards the northern contact, where the border consists of ultra-mylonitic talc-schist lenses. In contrast, the southern contact at Juferjoch is only intermediately deformed and covered mainly by rockfall. The middle of the profile demonstrates the geometry of the slice with sheared talc-schist lenses tectonically on top. Mylonitic metagabbro are also present as thin sheared out lenses within the highly deformed metagabbro near the southern contact.

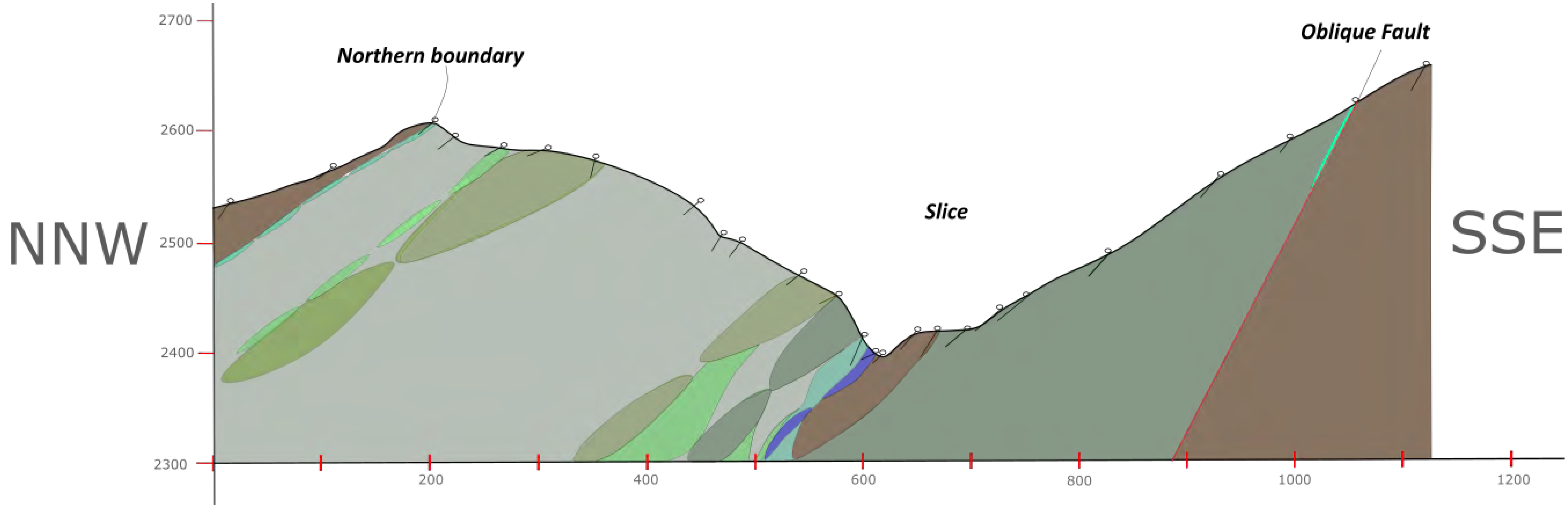

Figure 3.6. Cross section 3 (CS3) reveals how the metagabbro's internal structure comprises heterogeneously deformed sheared lenses. Between the thick northern mylonitic metagabbro and the southern weakly-to-undeformed metagabbro, multiple lenses of heterogeneously deformed metagabbro, the meta-volcanoclastic, and the calcschist occur. Most of the deformation i taken up by the ultra-mylonitic talc schist and the calcschist lenses leaving the surrounding metagabbro weekly-to-undeformed. The oblique fault in the SE marks a sharp contact between the metagabbro and the calcschist.

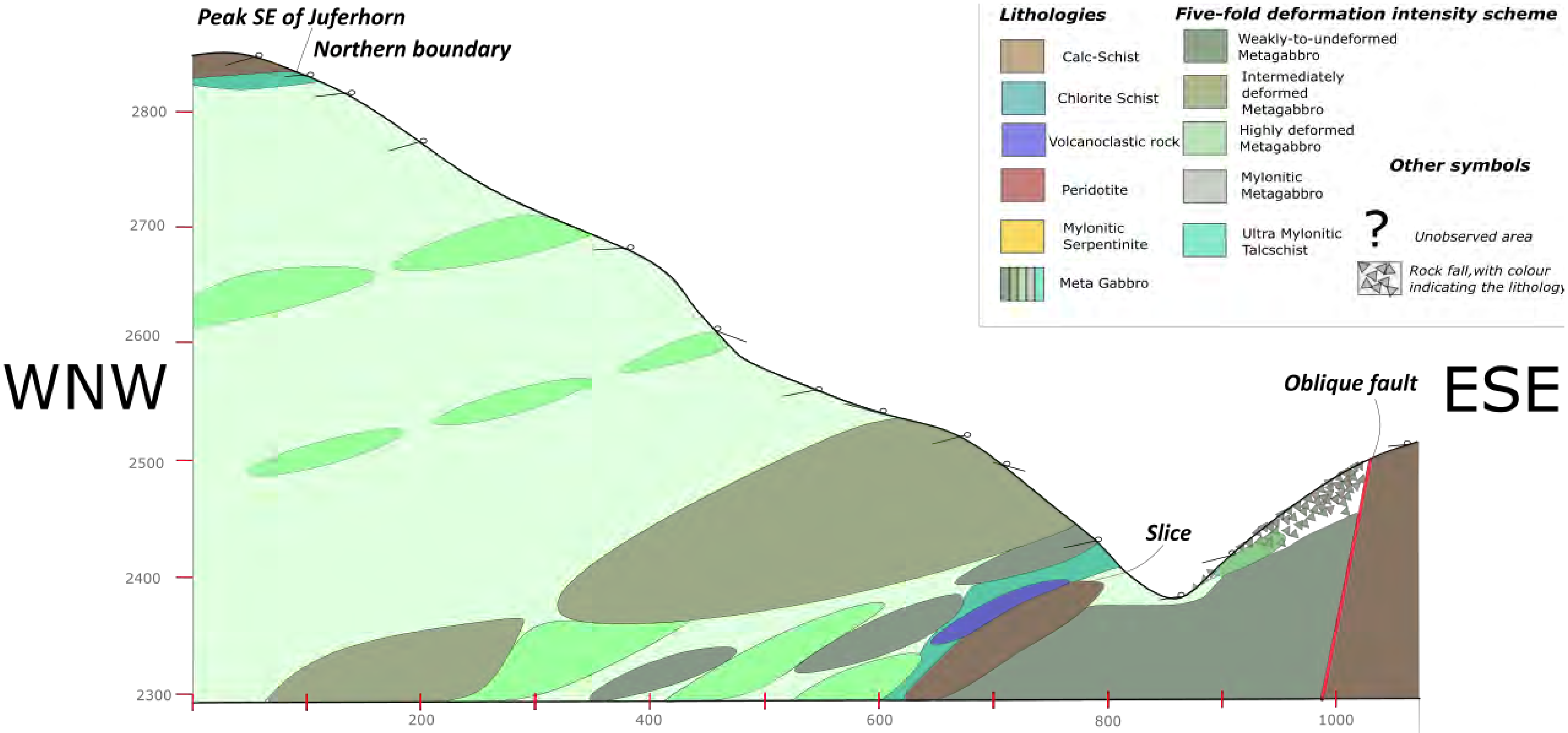

Figure 3.7. Cross-section 4 (CS4) is drawn parallel to the lineation and the strike of the foliation. Thus dips appear shallow. The cross-section extenuates the metagabbro's heterogeneous deformation in the form of lenses extended to the direction of transport (Top W). The mylonitic to ultra-mylonitic softer fabrics fill the spaces between more resistant, weakly-to-intermediately deformed metagabbro lenses. Furthermore, the slice and its heterogeneous complex lithologies surrounding it make up the same direction of transport: a top W ductile shear zone, which is also prevalent in the thicker northern mylonitic metagabbro. The thick weakly-to-undeformed metagabbro in the ESE is somewhat sheltered from the deformation but affected by the oblique fault shown as the sharp red boundary.

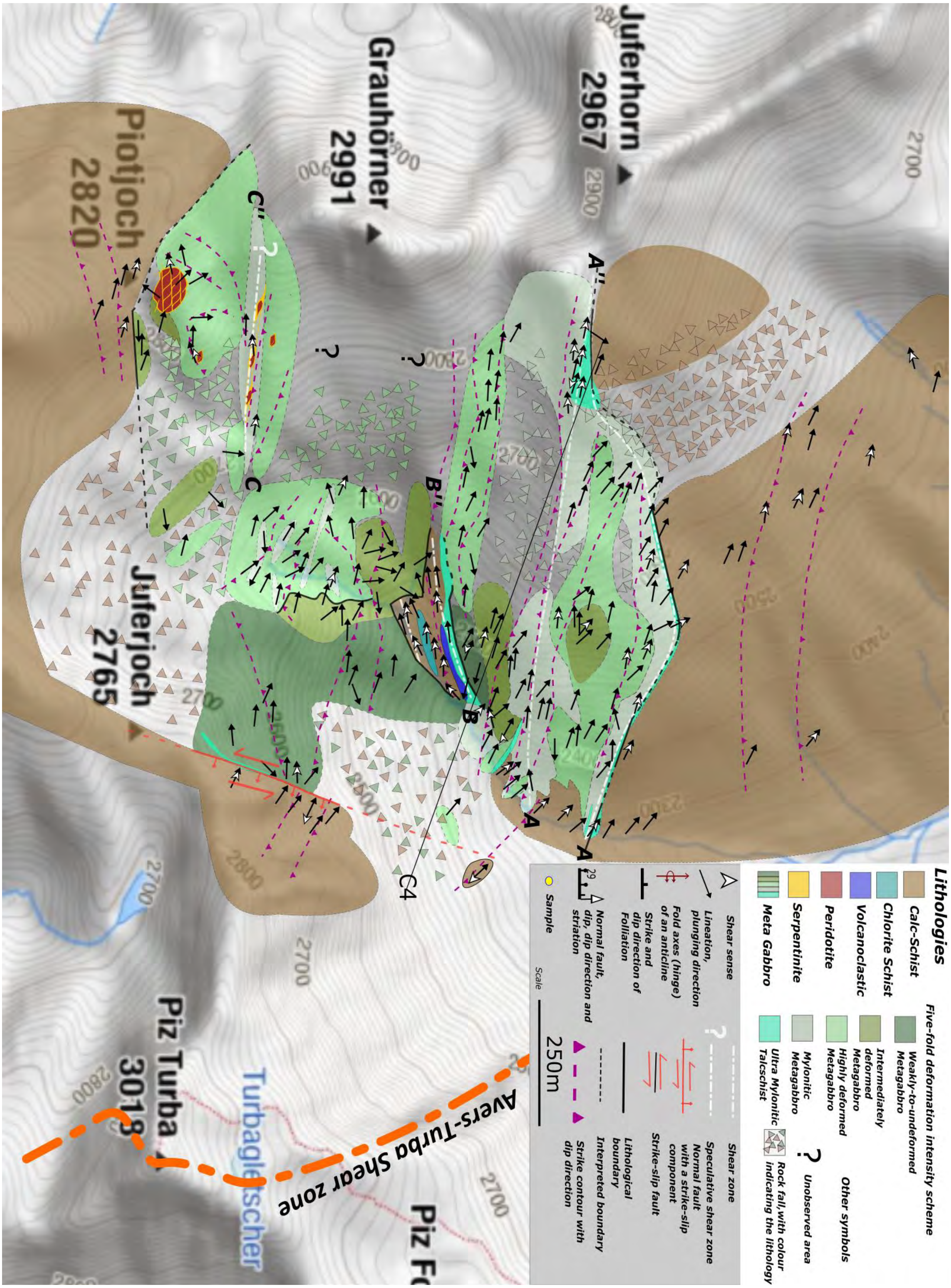

Figure 3.8. Lineation and shear-sense (retrieved from field observations and petrographic microscope analysis) data emplaced on the map.

3.4 Mesoscopic Analysis

In this chapter, all structures measured during fieldwork will be introduced. These structures (foliation, stretching lineation, shear-sense indicators, fold axes, axial planes, fault planes, and slicken striations) are described using stereonets and field images, of whom processes are inferred.

3.41 Foliation

Here, the primary foliation (S_1) is described as the first deformational phase observed (D1). The study area is dominated by an overarching trend of moderately NNE-dipping foliation planes (figure 3.9). This trend is the most consistent in the mylonitic metagabbro, the weakly-to-undeformed metagabbro, the slice, and the calcschist (figure 3.9 A, D-F). In contrast, the highly deformed and intermediately deformed metagabbro show a wider data spread (figure 3.9 B-C). The highly and intermediately deformed metagabbro make up outcrops that have been folded, noticed by the steep south-dipping foliation planes, and a spread towards intermediately-to-steep-NW-dipping foliation planes observed in the highly deformed metagabbro surrounding the massive peridotite at Piotjoch (figures 3.1, 3.9 B-C). Otherwise, the primary NNE-dipping trend is pervasive and is therefore interpreted as the main foliation. The mylonitic foliation reflects a substantial anisotropy with a slight variation in their preferred orientation: The mylonitic metagabbro and the calcschist is dipping moderately to the NNE (figure 3.9a and f). In contrast, the slice shows foliation planes dipping to the N-to-NNW (Figure 3.9E).

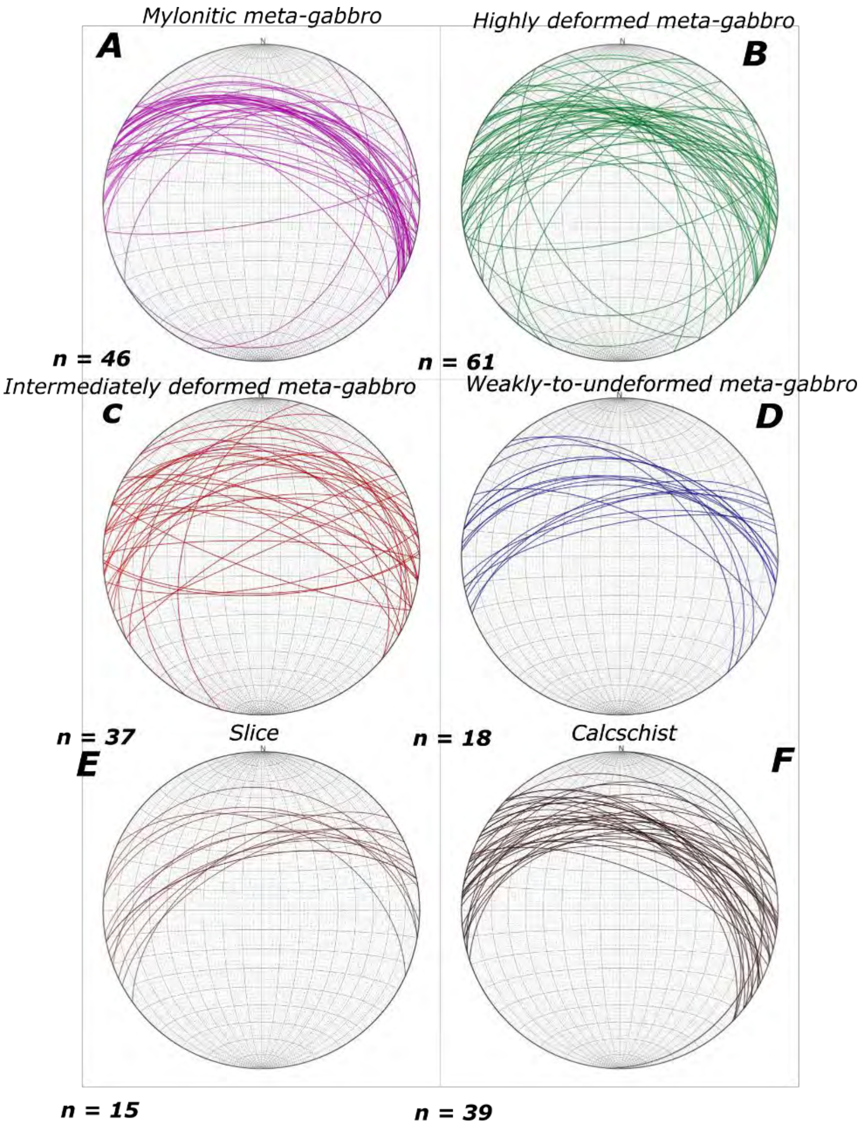

Figure 3.9. Stereonets use an equal area to project the foliation as great circles. The stereonets are divided according to deformation intensity and lithology, with the slice being an exception including meta-volcanoclastic, mylonitic chlorite-schist, and mylonitic calcschist.

3.42 Stretching lineation

Here, the stretching lineations are described as part of the D1-phase. The entire study area is dominated by shallowly WNW plunging (~ 290°) stretching lineations (figures 3.8 and 3.10), apparent in all lithologies regardless of their deformation intensities. There is some scatter of more steeply plunging NW trending stretching lineation in the highly deformed metagabbro and some in the intermediately deformed metagabbro. Some scattering is observed in the intermediately deformed metagabbro south of the slice and the heavily deformed metagabbro surrounding the massive peridotite at Piotjoch (figure 3.8). However, the primary trend still reflects WNW trending stretching lineation. Therefore, it is interpreted that the WNW trending lineation represents the main deformation stage. Like observed in the foliation data, the mylonitic rocks show the highest anisotropy. The slice is the only mylonitic area that diverts from the primary trend with more westerly trending stretching lineations (260°, figure 3.10e).

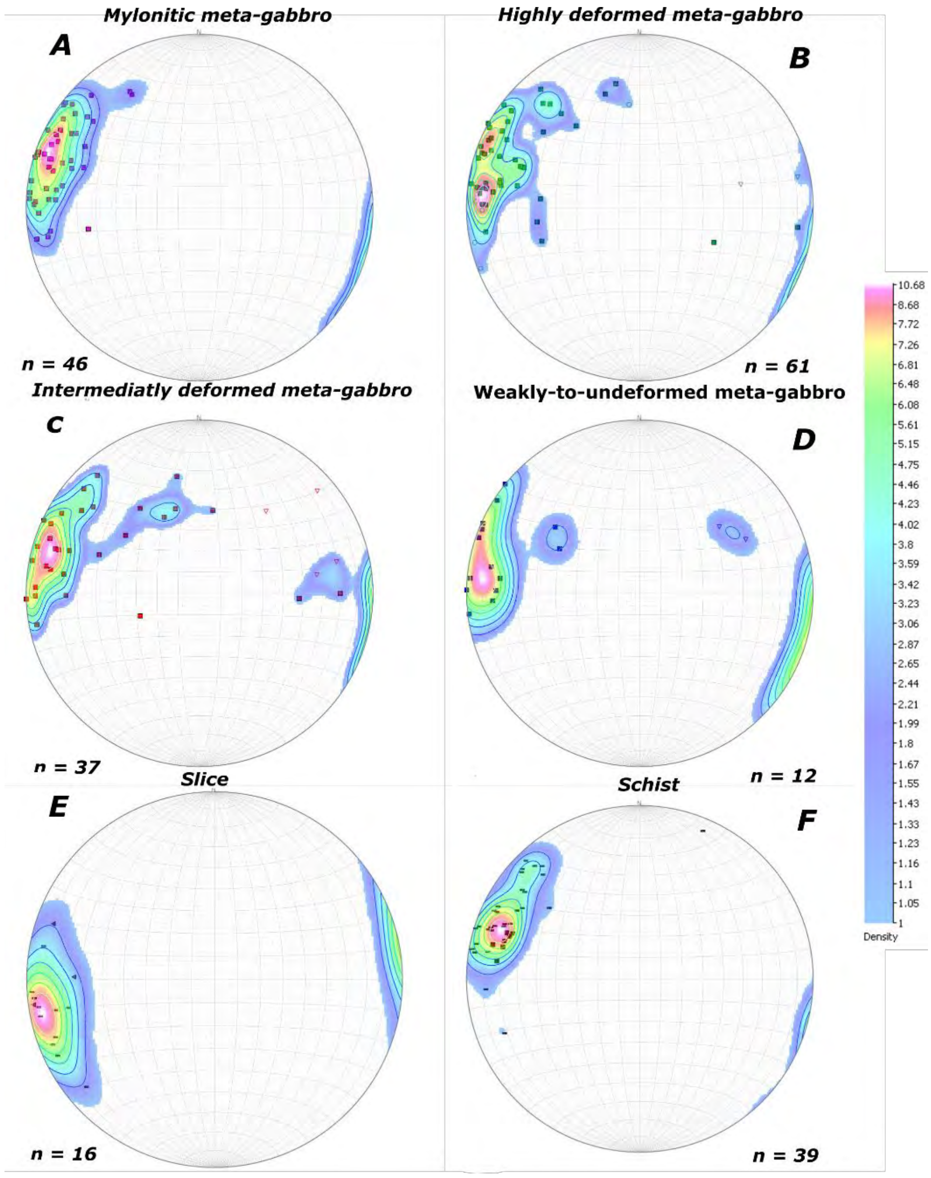

Figure 3.10. Stereonets using the equal area to project the lineation data. Contouring is done on the density of measurements based on an exponential function using IOGAS software.

3.43 Mylonitic fabrics and shear-sense

The following are examples of shear-sense indicators analysed in the field: (1) Asymmetrical eye-shaped carbonate and quartz boudins with a micaceous foliation stretching around it (figures 3.3a-c, and 3.11b). These range from 1 to 10-centimetre long but are mostly restricted to 1 to 2-centimetre boudins in the metagabbro. (2) Asymmetrically shaped lenses of intermediately deformed meta-gabbro outcrop with an apparent shear-sense (figures 3.3h-g, and 3.11a). (3) Asymmetrical shear folding (figure 3.3c), and (4) asymmetrical clusters and lenses of talc-schist proximal to the calcschist-metagabbro contact (figure 3.2h). (5) Lastly, the highly stretched serpentine crystal at Piojoch makes out the shear-sense of small-scaled normal faults(3.3 e). Observations show that shearing within the Juf Gabbro increases from the Juferjoch fault in the SSE towards the NNE (figure 3.8). A large proportion of the shear-sense indicators (81.1%) reflect top-to-the-WNW movement (table 3.1); therefore, it is interpreted that the shearing reflects top-to-the-WNW movement. It should be acknowledged that there is conflicting shear-sense observed on small-scale features such as shear bands and boudins in the northern (tectonically above the slice) part of the study area.

Shear sense		Coordinates	
Top W	Top E	Northing	Easting
	2	46°25'12"N	09°34'59"E
4	3	46°25'12"N	09°34'59"E
1		46°24'43.74"N	09°34'59.11"E
1		46°25'10"N	09°34'58"E
1		46°24'44.26"N	09°35'03.43"E
1		46°25'00.34"N	09°35'29.03"E
1		46°25'03.19"N	09°35'29.68"E
1		46°25'08,61"N	09°35'26.22"E
1	1	46°25'10.13"N	09°35'25.2"E
1		46°25'01.57"N	09°35'32.9"E
1		46°25'03.14"N	09°35'35.56"E
1		46°25'07.87"N	09°35'43.58"E
	1	46°24'59.72"N	09°35'27.68"E
1		46°24'37.13"N	09°34'45.88"E
		46°24'47.82"N	09°35'38.55"E
1		46°24'38.07"N	09°34'52.15"E
1		46°24'36,23"N	09°34'47.05"E
1		46°24'36.93"N	09°34'45.63"E
1		46°25'38.38"N	09°34'56.73"E
1		46°25'11,56"N	09°35'34.39"E
1		46°25'11.56"N	09°35'34.39"E
1		46°25'13.21"N	09°35'21.25"E
1		46°25'06.03"N	09°35'41.92"E
1		46°25'16.46"N	09°35'22.46"E
4	1	46°25'18.38"N	09°35'21.27"E
7	3	46°25'22"N	09°35'18.88"E
1		46°25'06.03"N	09°35'41.92"E
1		46°25'07.09"N	09°35'42.89"E
1		46°25'03.62"N	09°35'36.92"E
5	1	46°24'59.28"N	09°35'28.74"E
1		46°24'56.51"N	09°35'22.94"E
1		46°24'34.34"N	09°34'46.46"E
1		46°24'34.92"N	09°34'50.4"E
1		46°24'47.77"N	09°35'39.07"E
1		46°24'45.82"N	09°35'38.49"E
	1	46°25'00.83"N	09°35'45.73"E
1		46°24'49.01"N	09°35'39.1"E
1		46°25'17.64"N	09°35'16.76"E
1		46°24'58.56"N	09°35'27.03"E
1		46°24'58.25"N	09°35'26.31"E
1		46°24'57.27"N	09°35'24.32"E
1		46°24'57.09"N	09°35'24.59"E
1		46°24'57.27"N	09°35'20.74"E
1		46°25'27.81"N	09°35'35.73"E
Total Ratio	56 Top W	13 Top E	81.1% Top W

Table 3.1 showing shear-sense data retrieved from the field, as well as the coordinates to localities which exhibit shear-sense. Colours indicate what lithology the data was retrieved from which corresponds with the colours used on the map.

Mapping identified mylonitic to ultra-mylonitic zones: The most significant area is the northern mylonitic zone (A-A"), consisting of two parallel mylonitic belts stretching E-W (figure 3.8). These two belts stretch continuously- parallel with their stretching lineations, around the highly-and intermediately deformed metagabbro lenses from the river in the east to the peak southeast of Juferhorn. This zone is folded at the northern contact to the calcschist, and ultra-mylonitic talc-schist is observed associated with the calcschist contact (figure 3.8). Shear-sense indicators reflect top-to-the-WNW movement with some scatter observed to the ESE.

The second mylonitic zone (figure 3.8, B-B") is situated around the slice between the lenses of the weakly-to-undeformed and intermediately deformed metagabbro. It incorporates the slice and the ultra-mylonitic talc-rich metagabbro above the slice. The chlorite schist that is outcropping as a layer within the slice exhibit shear folds (figure 3b), which shows top W movement along with the carbonate-quartz boudins. The presence of shear-folded chlorite schist further corroborates shearing as the cause of the occurrence of the slice in the metagabbro. Lastly, a shear zone is present as a layer of mylonitic metagabbro with boudinaged peridotite around Grauhörner (figure 3.8, C-C"). These boudins and the mylonitic serpentine shear bands surrounding them reflect top-to-the-W movement.

Moreover, mylonitic rock and top-to-the-WNW shear-sense indicators are observed within the calcschist at Piotjoch. Thus, top-to-the-W/WNW shearing is observed both tectonically under and above the massive peridotite body at Piotjoch, indicating that the peridotite body must have been incorporated in the shear zone. The shear zone influencing the peridotite is not well constrained due to the highly topographic terrain surrounding Grauhörner. The top-to-the-W shear-sense indicators are overprinted by top-to-the-SE shear-sense indicators in the calcschist east of the Juferjoch Fault (figure 3.8).

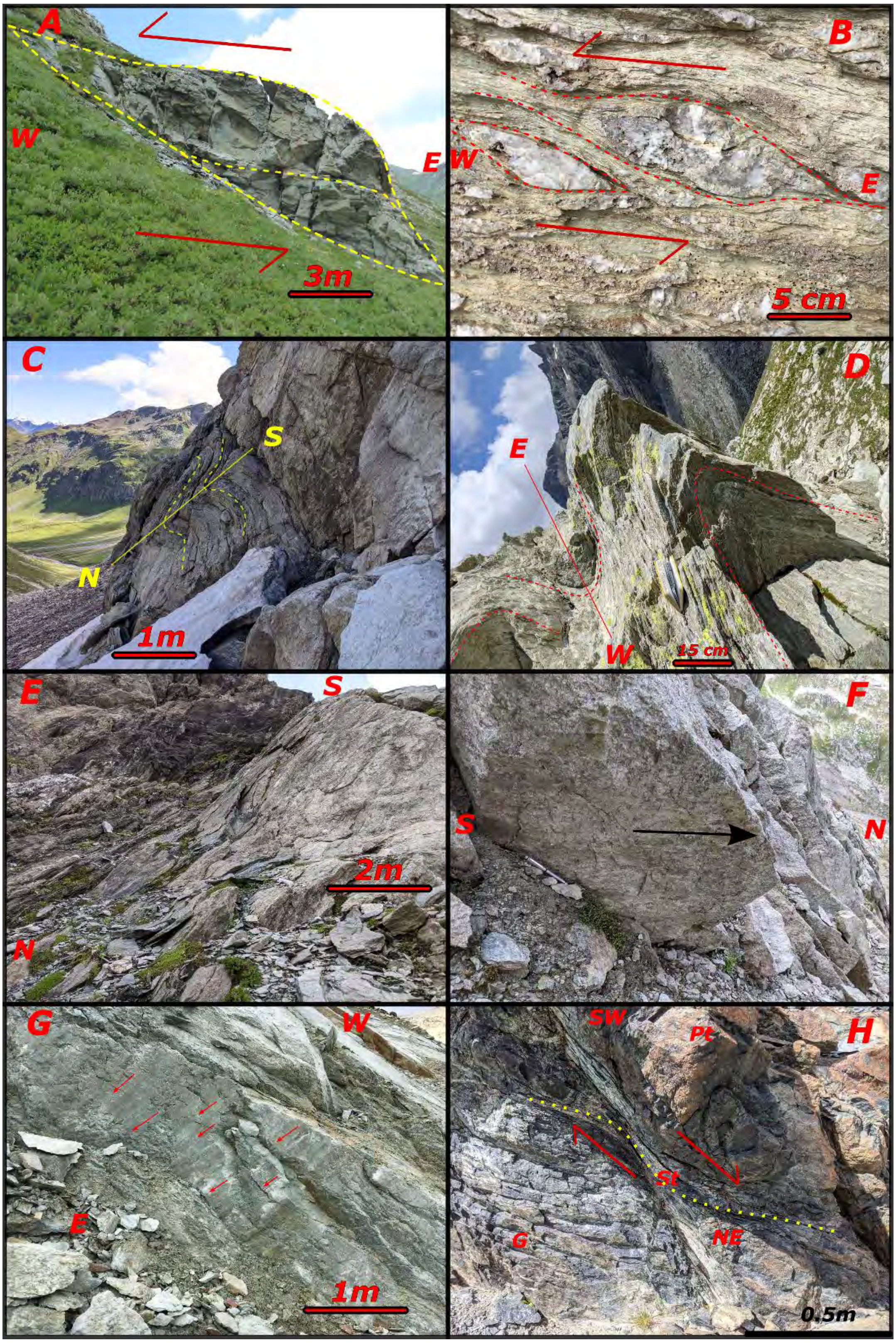

Figure 3.11, field images. Figure a displays a large-scale feature of intermediately deformed metagabbro indicating top W (sinistral) movement. Figure b show mylonitic metagabbro with carbonate boudins at the peak SE of Juferhorn, indicating top W shearing (sinistral). Figure c shows an intermediately deformed metagabbro folded by an NNW-trending, with a N dipping axial plane. Figure d shows a highly deformed metagabbro folded by W plunging axes with an N-dipping axial plane. Figure e displays the N-S striking Juferjoch fault. Figure f demonstrates a plethora of blocks that have suffered a cataclastic sinistral juxtaposition to one another adjacent to the Juferjoch fault. Each block is accompanied by sinistral shear-sense Figure G displays a large easterly steeply dipping normal fault surface adjacent to the Juferjoch fault. Figure g shows an NNE dipping normal fault between the massive peridotite and the metagabbro with bands of serpentine indicating top NE movement.

3.44 Folds

The discontinuity of outcrops observed in the field is interpreted as being caused by south-vergent asymmetrical folding forming a landscape where long limbs of moderately NNE-dipping foliation are folded every 100 metres along strike (figures 3.12 and 3.13). These south-verging folds have westerly plunging axes with north-dipping axial planes subparallel to the foliation (figures 3.11 c, d, and 3.12-3.14). The subsequent short limb is steeply southerly dipping and is frequently covered by soil.

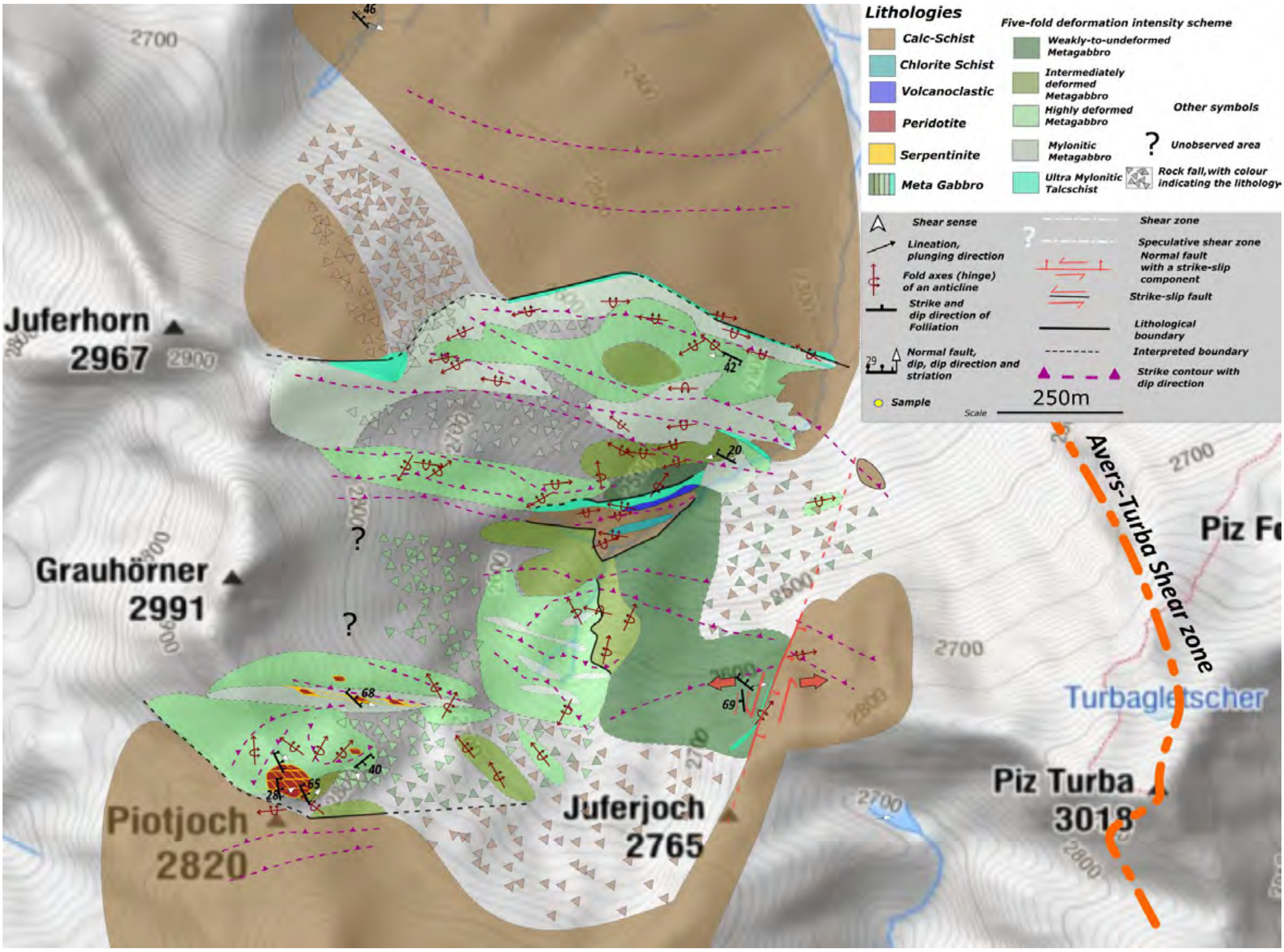

Figure 3.12. Fold axes and fault (dip and dip-direction) measurements are put onto the map.

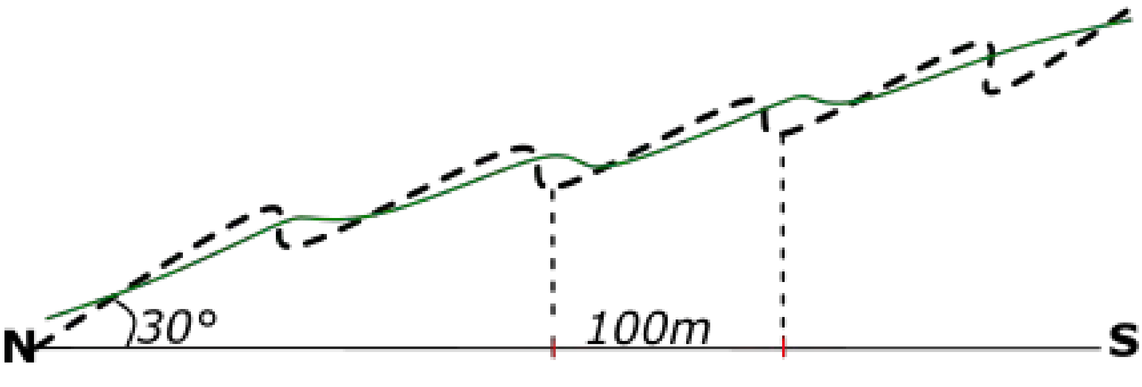

Figure 3.13. Schematic drawing of the slanted mountain-hillsides topography and its asymmetrical folds. The green line shows the topography, and the dotted line shows the extent of outcropping bedrock.

The folding are most prevalent in a zone stretching from NNE to SSW, causing the metagabbro's foliation to scatter (figure 3.14). These folds are pervasively influencing the metagabbro by folding the main foliation without any axial planar growth witnessed in the field; therefore, folding must have taken place after the development of the main foliation. The fold data reveal N-dipping axial planes with westerly plunging axes pervasively folding all lithologies (figure 3.14).

The mylonitic rocks show consistent N-dipping axial planes with westerly plunging axes; only the mylonitic metagabbro show some scatter ranging from WSW to WNW (figures 3.14 a, e, and f). The highly deformed metagabbro are expressing NE-SW trending axes with N-dipping axial planes. The highly deformed and mylonitic meta-gabbro's axial planes form a π-pole indicating a refolding event by fold axes trending towards NW (~ 310°) (figure 3.14b). This re-folding does not appear in any other stereonet, although the intermediately deformed and the weakly-to-undeformed metagabbro show a greater scatter than the mylonitic bedrock (Figures 3.14c and d).

Overall, most east-west trending fold axes are observed in the slice and the metagabbro north of the slice, whereas the area between Grauhörner and Juferjoch exhibits more NNE to NNW trending fold axes (figure 3.12). Although no structural measurements were achieved over the steep mountain ridge between Piotjoch and Grauhörner (figure 3.12), visual observation shows that it has suffered a high degree of folding with axes comparable to the measured data.

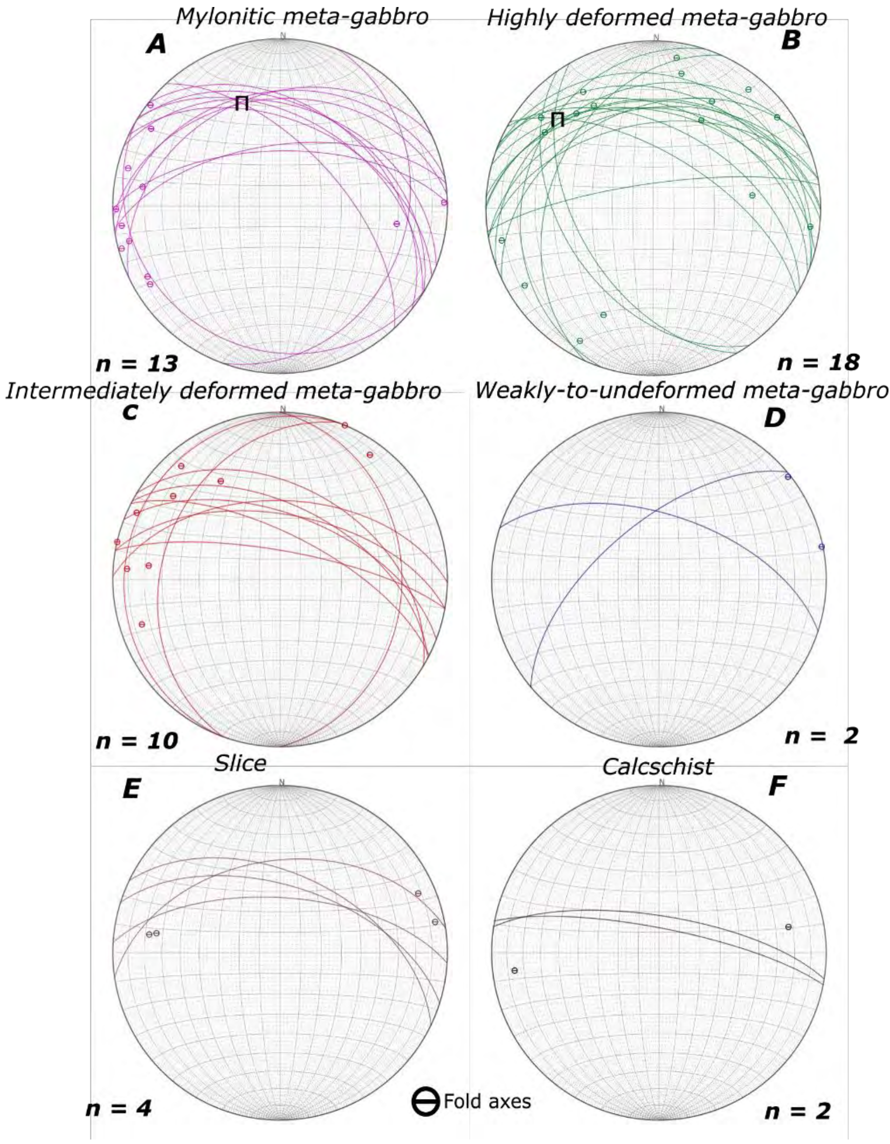

Figure 3.14. Showing stereonets (A-F) using the equal area to project dip, and dip direction data of axial planes as great-circles, and fold axes are shown as dots, n refers to the number of measurements shown in the plot. Figure b shows great circles converging into forming a Π-pole, indicating the re-folding of the axial planes.

3.45 Faults

The study area's south-eastern contact between the weakly-to-undeformed metagabbro and the calcschist is divided by the Juferjoch fault. This steep, easterly-dipping feature penetrates the main foliation (figure 3.11e). The Juferjoch fault is striking N-S, forming an extensive feature stretching from the saddle of Juferjoch down the valley, forming a steep cliff-face visible from a great distance (figure 3.12). Several fault surfaces are observed along with the primary fault contact: Normal fault surfaces dipping steeply towards the east, accompanied by easterly trending slicken striations (figure 3.11g). The second type of fault surface observed is either dipping to the west or the east, with slicken striations shallowly plunging to the N. These surfaces are accompanied by cataclastic sinistral strike-slip features (figure 3.11f). Therefore, the Juferjoch fault is an oblique fault with an E-W extensional component and a N-S sinistral strike-slip component. Within the Juferjoch fault, there is a 2-metre-thick talc-schist layer outcropping between the metagabbro and the calcschist.

Furthermore, several normal faults have been observed influencing the peridotite. These normal faults are moderately-to-steeply dipping towards the NE and dividing the undeformed peridotite pods. The faults are less extensive than the Juferjoch fault, with a top-to-the-E/NE displacement of sub-1-metre notable by the plastically deforming serpentine bands curving through the fault plane that is cataclastically offsetting the metagabbro and the peridotite (figure 3.3g and figure 3.11h). Thus, the normal faults are younger than the metagabbroic foliation but formed under plastic serpentine conditions. These faults represent less extensive fault surfaces that are coherent with the main Juferjoch fault. They both record normal top-to-the-E/NE movement proximal to the calcschist contact.

Two normal fault planes were recorded in the metagabbro NE of the slice: a shallowly NE dipping with plastically deformed westerly trending stretching lineations and one moderately southerly dipping foliation plane cataclastically offsetting the metagabbro towards the west.

3.5 Microscopic Analysis

In this chapter, the metamorphic reactions that produce the constituents of the main S_1 foliation and the penetrative W-trending stretching lineations are inferred from the weakly-to-undeformed metagabbro. After that, the metagabbro is described with increasing deformational intensity with textures indicating a gradual increase in fluid activity. Lastly, the other lithologies of the study area are detailed. The abbreviations used in figures are by Whitney and Evans, (2010), as following: Tur = Tourmaline, Aug = Augite, Cam = Calcic-amphibole, Pl = Plagioclase, Ep = Epidote; Tnt = Titanite, Hem = Hematite; Rbk = Riebeckite, Cal = Calcite; Qz = Quartz, Wm = White Mica; Chl = Chlorite, and Tlc = Talc.

Metagabbro

The overarching mineral assemblage of the Juf Gabbro main metamorphic phase is chlorite+talc+calcic-amphibole+epidote, with no high-pressure relicts observed. The weakly-to-undeformed metagabbro samples demonstrate the breakdown of porphyroclastic augite into the constituents of the S_1 foliation: Porphyroclastic augite crystals are rimmed by pale-pleochroic calcic-amphiboles (figure 3.15a-b), with pale-pleochroic chlorite and talc growing in the same prefered orientation as the augite crystals' cleavage planes (3.15a-b). Furthermore, figure 3.15c-d displays the crystal shape of a porphyroclastic augite, rimmed by calcic-amphiboles, with internal growth of chlorite and talc. These observations infer reaction 1 (R1): The breakdown of porphyroclastic augite produces rhombic calcic-amphibole, talc and chlorite – of which the two latter are the primary constituents of the S_1 foliation and stretching lineation. Presumably, the breakdown of igneous olivine also took part in the production of talc and chlorite, although this is not observed.

Augite + Water → Calcic-amphibole + Talc + Chlorite (R1)

Furthermore, the breakdown of porphyroclastic plagioclase to colourless-to-pale-yellow pleochroic epidote (R2) is observed in these samples (figures 3.15c-d and g). The epidote crystals are often zoned, with a higher birefringence in the core of the crystal compared to the rim.

Plagioclase + Water → Epidote (R2)

The intermediately deformed metagabbro comprises segments of porphyroclastic plagioclase, pre-deformational growth of rhombic calcic-amphibole crystals of low second-order birefringence and titanite (figure 3.16a). These segments are separated by a fine-grained mesh of quartz and epidote crystals, with calcic-amphiboles growing as syn-deformational elongated fibrous crystals of high second-order birefringence, elongated syn-deformational titanite, and hematite. These crystals grow alongside a foliation consisting of chlorite (figure 3.16b). Another intermediately deformed sample shows a penetrative foliation of chlorite and talc with elongated calcic-amphiboles and epidote-clusters resembling shapes of a plagioclase aggregate. In this thin section (G35s, figure 3.16c), some cracked rotated crystals of augite are preserved with talc, chlorite and hematite growing in the fractures, reflecting a sinistral top-to-the-W shear component.

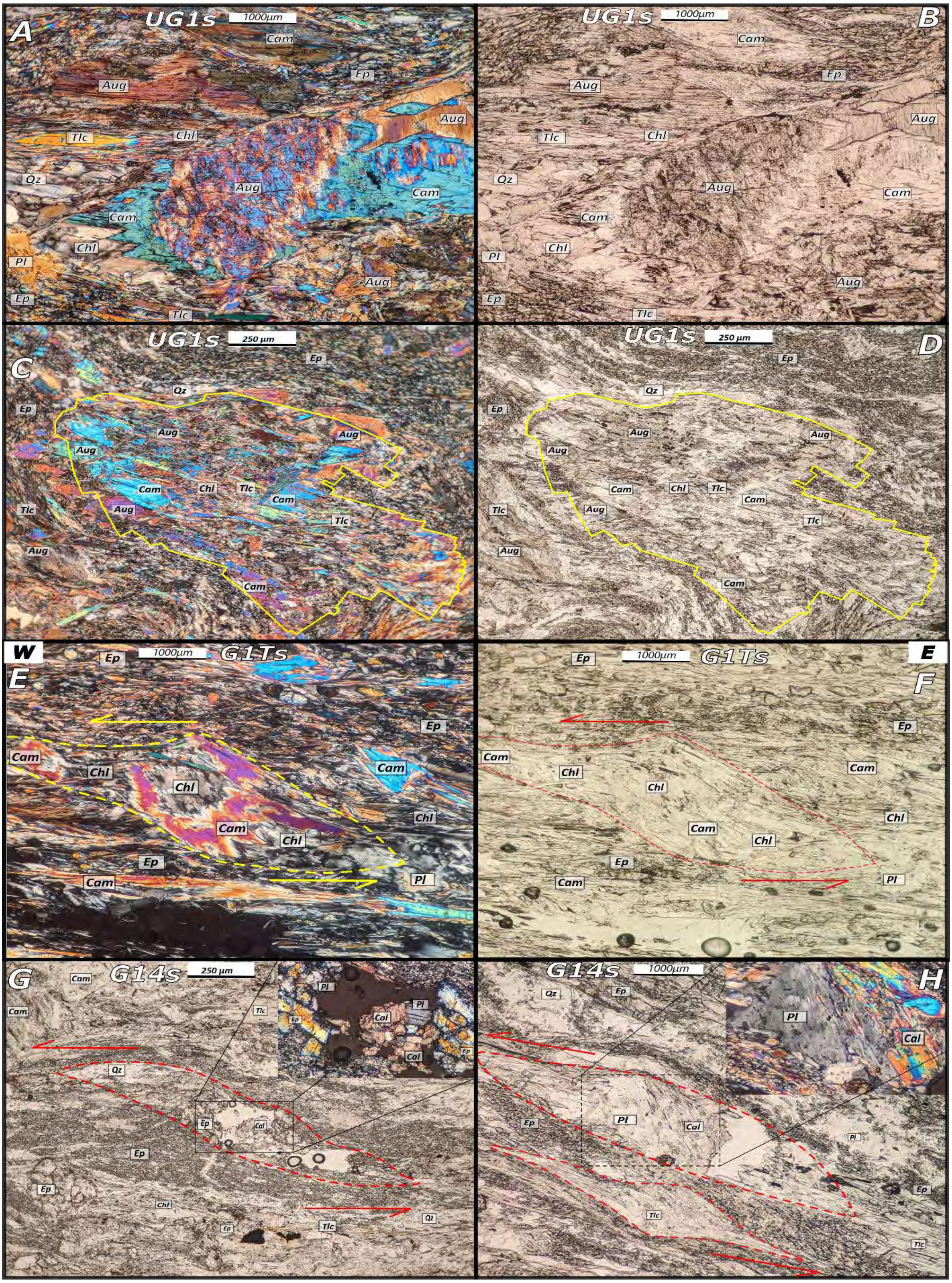

Figure 3.15 displays the reaction texture that is observed in the metagabbro in XPL, and PPL. Samples E-H are oriented W-E, whereas the first four (A-D) lack orientation. The first two reactions (R1 and R2) are observed in the weakly-to-undeformed sample UG1 (A-D); augite → calcic-amphibole + talc + chlorite, plagioclase→ epidote. Figures A-B are showing an augite crystal rimmed by calcic-amphiboles, and plagioclase being replaced by epidote (left-bottom corner). Figure C-D shows the outline of a relict augite crystal in red, its interior has been replaced by chlorite, talc and calcic-amphibole. Figure E-F displays the disequilibrium of calcic-amphibole crystals in an ultra-mylonitic talc-schist sample, calcic-amphibole is replaced by colourless pleochroic chlorite with a sinistral shear component. Figures G-H shows quartz-plagioclase boudins which successively develop into quartz-calcite boudins by calcite + epidote replacing Plagioclase. Figure H shows calcite exploiting and replacing fractured plagioclase crystal inside a Qz-Pl boudin.

The highly deformed metagabbro (figure 3.16c) consists of syndeformational growth of fine-grained quartz bands separated by a penetrative foliation of talc and chlorite. The foliation penetrates and breaks up the quartz bands with the growth of fine-grained epidote, indicating sinistral top-W shearing (figure 3.16c). In the foliated layers, rotated crystals of zoned epidote crystals, porphyroblastic calcic-amphiboles, and porphyroclastic plagioclase + quartz clusters experience asymmetrical growth chlorite – making up strain shadows and sinistral top-to-the-W shear-sense indicators (supplementary material, figures 4 and 9). At this stage, the reaction augite to calcic-amphibole has gone to completion, and most porhyroclastic plagioclase exhibit epidote inclusions. Epidote growth is observed as clusters or large crystals that resemble the shape of plagioclase aggregates.

The mylonitic metagabbro (figures 3.15 e-h and 3.16 e-f) show a penetrative foliation of chlorite and talc, with a pervasive sharing component. Shear-sense indicators frequently occur as asymmetrically-sheared out eye-shaped calcic-amphiboles (figures 15e-f). In the ultra-mylonitic samples, these colourless-pleochroic, 2nd-order birefringent calcic-amphiboles are being replaced by colourless-pleochroic chlorite growing inside it and in the strain shadows (R3). Calcic-amphiboles are also observed as needle-like, highly-elongated crystals with chlorite growth in the strain shadows (figures 15e-f).

Calcic-amphibole $\rightarrow$ Chlorite (R3)

Bands of quartz and plagioclase are broken up by top-to-the-W shearing into asymmetrical boudinaged shapes with chlorite growing in the strain shadows (figures 3.15 g-h, 3.16e). Epidote and calcite progressively replace the porphyroclastic plagioclase crystals within these boudins (R4). Other mylonitic samples such as G3 (figure 3.16f) and 20/9 (supplementary material figure 20) show a higher degree of carbonation being incorporated into more significant quartz + calcite boudins and the mylonitic foliation. However, plagioclase is still observed in these samples – expressing a disequilibrium with calcite frequently replacing it (R4, figure 3.16f). This observation helps explain the pitted weathering observed in the high-to-mylonitic deformational intensity in the field.

Plagioclase + CO_2 $\rightarrow$ Calcite (R4)

In all mylonitic samples, shearing is also expressed through highly asymmetrical talc clusters resembling a fish-eye shape indicating top-to-the-W movement (figure 3.16d and supplementary material figure 14). Furthermore, ultra-mylonitic samples (figure 3.16d) exhibit hematite growth. The hematite grows on second-order birefringent crystals of what could be calcic-amphiboles or augite relicts, with clusters of fine-grained epidote surrounding it. This forms an eye-shaped structure with chlorite penetrating and growing in the strain shadows – marking a top-to-the-W asymmetry. The microscopic analysis concludes that the meta-gabbro is depleted in Fe concentrations compared to Mg. This is based on the observations of colourless pleochroic calcic-amphiboles and chlorite – suggesting Mg-end-members. Furthermore, there is a higher proportion of colourless pleochroic epidote with an andalouse blue birefringence than yellow pleochroism epidote – suggesting a Fe depletion. This interpretation is consistent with the previously mentioned observation that the mylonitic metagabbro is white to light-green coloured in hand sample, lacking the yellowish tone of epidote.

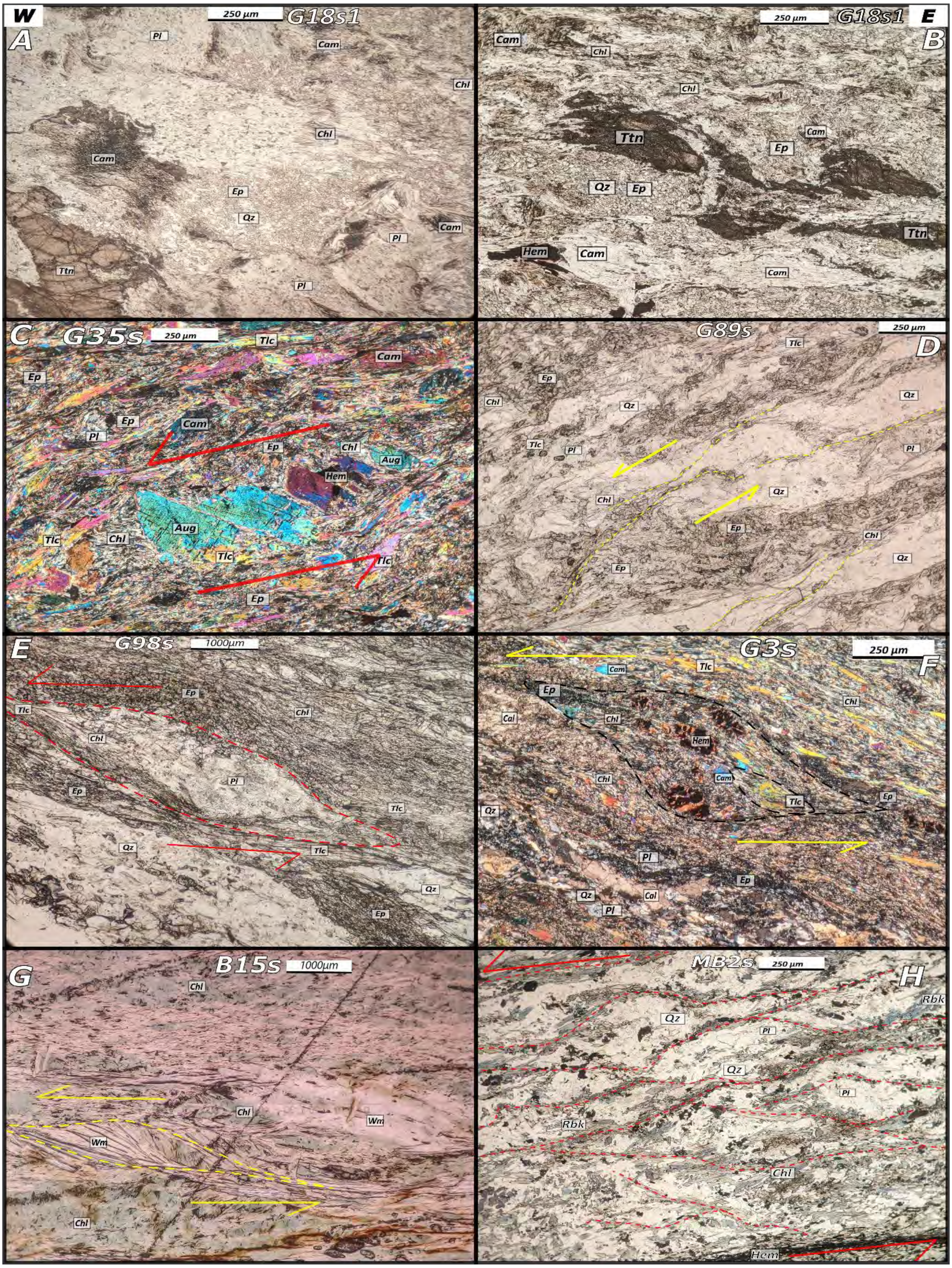

Figure 3.16 shows the progressive increase in deformational intensity and amount of strain observed in the samples A-F. The massive part of the intermediately deformed samples consists of the igneous texture observed in A. These massive parts eventually develop foliation planes of calcic-amphibole and chlorite with syndeformation growth of titanite in B. In sample G35s (C), the foliation planes are fully developed, comprising talc and chlorite rich with a small proportion of augite remaining, reflecting a sinistral shear-sense with talc and chlorite growing in its cracks. No augite remains in the highly deformed metagabbro (D); C shows fine-grained quartz bands making up a large portion of the rock with a few relict plagioclases remaining. Figure E shows how the porphyroclastic plagioclase and quartz bands are sheared into asymmetrical shapes indicating sinistral top-W shearing. Figure F shows a carbonated mylonitic metagabbro; plagioclase is replaced by epidote and carbonate, and a 2nd order calcic-amphibole is replaced by hematite and chlorite – with a top-W asymmetry. Asymmetrical talc-clusters indicate a top-W shear sense also. Figure G shows sinistral top-W shearing within the chlorite-schist. H displays the metavolcanoclastic as the Na-amphibole with its hematite-boundary to the chlorite-hematite-epidote-bearing layer at the bottom.

The schist and the meta-volcanoclastic rock

The calcschist consists of carbonate, plagioclase and quartz layers with green pleochroic chlorite and white mica making up a penetrative foliation. Within the foliation, asymmetrically sheared plagioclase crystals with chlorite growing as strain shadows and fish-eye clusters of white mica express top-to-the-W asymmetry (supplementary material figure 25, and figure 3.16f). The chlorite schist exhibits micaceous clusters and shear bands of chlorite and quartz, indicating a top-to-the-W shear sense.

The meta-volcanoclastic samples comprise centimetre-thick plagioclase-calcite-sodic amphibole layers interlayered with millimetre-thick chlorite-epidote-hematite layers (figures 3.16h). These sodic amphiboles are rhombic or elongated with pale yellow to blue-purple pleochroism and low first-order birefringence. Therefore, it is interpreted that these amphiboles are riebeckites. The sodic amphibole-bearing layer consists of asymmetrical lenses of quartz and plagioclase, with elongated riebeckite and chlorite growing in between, indicating top-to-the-W shearing (figures 3.16h). At the same time, top-to-the-W shearing is expressed by chlorite growing in asymmetrical shapes around rotated epidotes chlorite-epidote-hematite layers (supplementary material figure 24).

4. Precursor rocks

In this chapter, the quantitative point-counting results will be introduced to grasp the mineralogy of each sample. Mineral modes were then recalculated into mole percentages for each sample based on the end-member stoichiometry from Holland and Powell (1998). This was all done to explore the protolith of the Juf Gabbro. The quantification may also reveal if the bulk composition is controlling the heterogeneous deformation of the Juf Gabbro. For instance, if the Juf Gabbro consists of two bulk compositions, a leucogabbro and a melanogabbro, this may explain the heterogeneous deformation. On the other hand, a single bulk composition would point to fluid deficiency; thus, the fluid flow and deformation are localised. All point-counting results are shown in Table 4.1.

Textural evidence of interlocking-porphyroclastic augite crystals (figures 3.15 a-d and 3.16c) suggests that Juf Gabbro's precursor rock was a gabbro. Other mafics, such as metabasalts or a meta-volcanic mafic rock, would only show porphyroclastic plagioclase with pyroxenes making up the interstitial melt or the fine-grained matrix. In contrast, a metagabbro is expected to show relicts of interlocking porphyroclastic pyroxene and plagioclase. The compositional layering observed within the meta-volcanoclastic rock requires its protolith to include sedimentary layering, corroborating the interpretation.

The point-counting results reveal that although deprived of quartz, the ultra-mylonitic talc-schist has a mineral mode close to the rest of the metagabbro (table 4.1, G1T). This result, along with the previously stated textural evidence (figure 3.15e-f), suggests that the talc-schist originated from the metagabbro. Moreover, the area SE of Juferhorn exhibits carbonate-quartz boudins (previously described in the macroscopic and mesoscopic analysis), including carbonate concentrations of up to 30% and depletion in plagioclase concentrations (table 4.1 and figure 3.1). This further supports the textural evidence showing plagioclase being substituted by carbonate (figures 3.15g-h).

	Primary Minerals									Accesory minerals - not involved in any reactions			
	Reactants		Products										
Sample ID	Aug	Pl	Cam	Ep	Tlc	Chl	Qz	Cal	Hem	Rbk	Wm	Ttn	Tur
UG *	2%	17%	20%	31%	0%	11%	14%	3%	0%	0%	0%	2%	0%
UG1	13%	7%	17%	25%	3%	23%	12%	0%	0%	0%	0%	0%	0%
G18s	0%	5%	11%	29%	10%	20%	13%	0%	0%	0%	5%	1%	
G18s1	0%	12%	14%	26%	0%	25%	14%	0%	0%	0%	2%	6%	
G35s	2%	6%	9%	34%	13%	29%	4%	0%	0%	0%	1%	1%	0%
G7s	0%	14%	12%	32%	6%	18%	17%	0%	0%	0%	0%	0%	
G39s	1%	3%	13%	40%	2%	20%	20%	0%	0%	0%	0%	1%	
G89s	0%	4%	1%	39%	9%	23%	21%	0%	0%	0%	2%	0%	0%
G41s	0%	1%	4%	34%	18%	22%	14%	0%	2%	0%	2%	0%	1%
G4s	0%	17%	7%	25%	18%	22%	12%						
G3s *		5%	2%	20%	0%	22%	11%	31%	0%				
G14s	0%	4%	14%	30%	12%	24%	13%	2%	0%	0%	1%	0%	
G98s	0%	0%	4%	35%	8%	25%	26%	0%	0%	0%	1%	0%	0%
20/3	0%	15%	10%	29%	8%	25%	13%	0%	1%	0%	0%	0%	0%
20/1	1%	11%	16%	28%	3%	25%	15%	1%	0%	0%	0%	0%	0%
20/9 *	0%	7%	0%	3%	0%	25%	41%	23%	0%	0%	1%	1%	0%
20/11	0%	7%	13%	21%	1%	33%	25%	0%	0%	0%	0%	0%	0%
G68s	0%	13%	13%	13%	19%	36%	1%	0%	0%	0%	3%	1%	0%
G1T		10%	12%	21%	19%	38%							
G46s	0%	1%	0%	24%	2%	45%	26%	0%	1%	0%	1%	0%	0%
G101s *	0%	1%	0%	0%	2%	33%	15%	26%	0%	0%	19%	3%	0%
20/5	0%	18%	0%	30%	0%	23%	29%	0%	0%	0%	0%	0%	0%
MB1	0%	10%	0%	15%	0%	13%	2%	30%	9%	12%	1%	5%	3%
MB2 (G)	0%	4%	0%	28%	0%	36%	6%	0%	19%	1%	1%	3%	2%
MB2 (B)	0%	17%	0%	0%	0%	16%	19%	2%	3%	32%	4%	3%	3%
20/8	0%	10%	0%	3%	0%	23%	20%	28%	4%	0%	9%	3%	0%
815	0%	1%	0%	1%	0%	73%	7%	0%	1%	0%	4%	3%	10%

*Table 4.1 shows the point-counting results in percentage for each mineral. The sample ID is colour-coded according to the deformation intensity and lithologies on the map and cross-sections. MB2 (G) refers to the epidote-chlorite-hematite bearing metavolcanoclastic layer, and MB2 (B) are referred to the sodic-bearing metavolcanoclastic, which were counted separately. The * indicates a carbonated sample. 20/8 is a calcschist sample from past the northern boundary (map), and B15 is a chlorite schist sample from the slice.*

Mole percentages plotted on an ACF diagram show that samples group in three distinct ways (figure 4.1): (1) Most metagabbro samples show a slight enrichment in aluminium but otherwise plot close to an average basaltic composition (purple X in figure 4.1). (2) Carbonated samples group close to the C-corner with the mylonitic carbonated metagabbro is plotting close to the calcschist composition. (3) The compositionally layered meta-volcanoclastic rock is plotting distinctly different. The chlorite-epidote-hematite layer is Al-rich and Na-poor compared to the sodic-amphibole-bearing layer plotting closer to the F corner. Lastly, the sample MB1 is a carbonated meta-volcanoclastic rock, plotting between other meta-volcanic rocks on the A and F axes, but more towards the C axis.

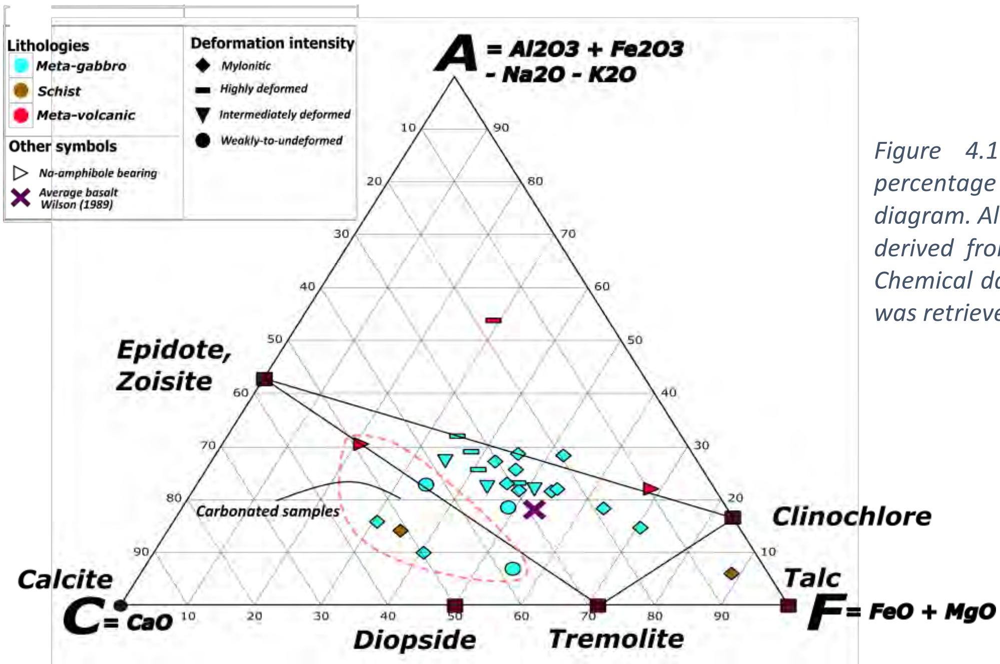

Figure 4.1 is showing all the mole percentage data compiled into an ACF diagram. All mineral compositions used are derived from Holland and Powell (1998). Chemical data for the average metabasalt was retrieved from Wilson (1989).

The ACF diagram shows no correlation between mole percentages and deformational intensities. Some mylonitic samples show close to identical bulk composition to the undeformed samples (figure 4.1) – suggesting that all the deformational intensities were derived from a similar bulk composition. However, all levels of the analysis suggest that the mylonitization along the northern boundary shows evidence of high fluid flow (e.g., deformation intensity increasing towards the northern boundary, the discontinuous talc-layer, asymmetrical carbonate-quartz boudins in figure 3.12, chlorite-rich samples; G46s and carbonation G3s (figure 4.1) in figure 3.15 g-h and 3.16f). Figure 4.2 reiterates the increase in deformational intensity towards the northern boundary and demonstrates that the highest volatile contents are found at the northern contact, supporting this interpretation. It should be acknowledged that the data does not validate a gradual increase in volatile content towards the northern contact, nor does it corroborate a correlation between the volatile content and deformational intensity (figure 4.2).

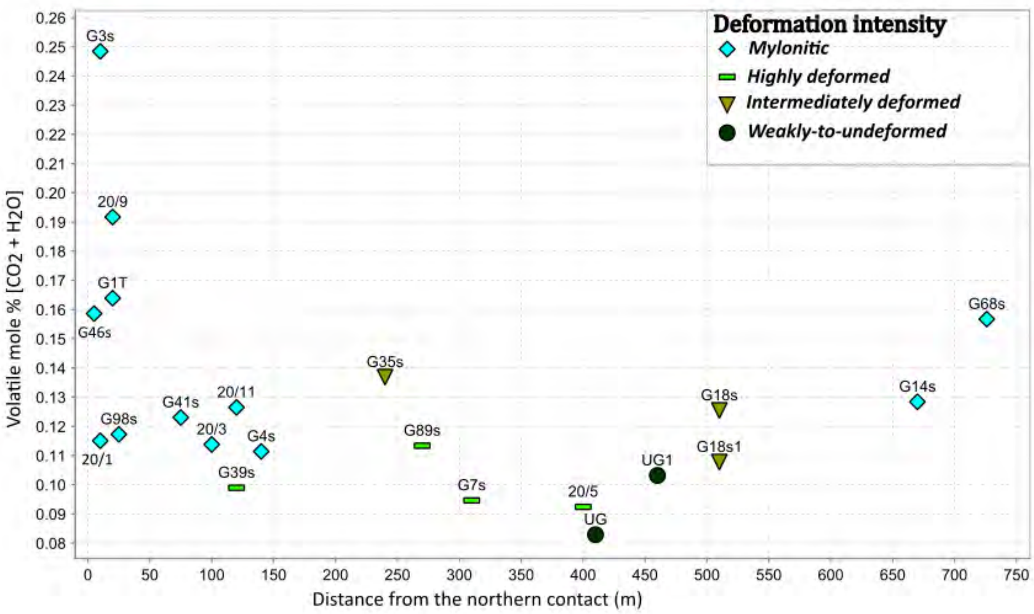

Figure 4.2 show mole percatage of volatile content in the metagabbro plotted against the distance away from the northern contact.

5. Discussion

5.1 Deformational stages

This chapter will present and discuss the deformational phases that influence the Juf Gabbro in chronological order.

5.11 The main tectonometamorphic stage (D1)

During the main tectonometamorphic stage (D1), the Juf Gabbro experiences the breakdown of porphyroclastic augite into calcic-amphibole, talc and chlorite – defining the S_1 foliation and the shallowly plunging WNW trending stretching lineation (figure 3.10). The early D1-stage is the only deformational stage that includes the growth of new minerals. Mylonitic fabrics of the D1-stage are accompanied by the top-to-the-WNW shear-sense indicators that reveal the direction of thrusting (Table 3.1). Moreover, the D1-stretching lineations and the top-to-the-W/WNW shear-sense indicators have been described in the Madris lense (Ring & Glodny, 2021) that experienced blueschist facies metamorphism of 9-12 kbar and 380 – 420°C (Ring, 1992; Engi et al., 2004). Although the mineral assemblage of the Juf Gabbro does not contain any high-P relicts, this study does not present enough evidence that corroborates the Juf Gabbro not being a part of the Avers Bündnerschiefer tectonic unit. Therefore, the D1-stage is suggested to have influenced the entire Avers Bündnerschiefer and occurred under high-P blueschist facies conditions of 9-12 kbar and 380-420°C (Ring, 1992; Engi et al., 2004). This D1 phase is the primary tectonometamorphic imprint of the Juf Gabbro and adjacent calcschist, whereas the rest of the Avers Bündnerschiefer has been overprinted by later orogenic events (e.g., the ATMZ).

The petrographic analysis of this study introduces a first-order tectonic problem within the Avers Bündnerschiefer: why is their evidence for blueschist metamorphism observed as a glaucophane-garnet ± chloritoid mineral assemblage and high-Si phengite in metabasites (Ring 1992) (Oberhänsli 1978), but no observable high-P minerals in the metagabbro. The Juf Gabbro only records mineral growth in the D1-stage, with no signs of a retrograde overprint. The lack of metamorphic mineral growth is often due to the absence of fluids causing low diffusion rates (Ague 2003). Although there are undeformed parts of the metagabbro showing disequilibrium textures (figure 3.15a-d), it is shown that the D1-stage involves fluid flow along the northern boundary. For instance, up to 30% carbonate concentration is observed at the peak, SE of Juferhorn, incorporated into the mylonitic foliation and top-to-the-WNW sheared boudins (figure 2.1). Moreover, hydration is observed in the ultra-mylonitic metagabbro with chlorite concentrations up to ~ 45% growing in strain shadows and replacing calcic-amphiboles (R3 and R4) (Table 3.2). Hence, any arguments involving low diffusion rates can be ruled out for mylonitic mineral growth. This leaves the bulk composition of the metagabbro as the most reasonable control. Therefore, the results suggest that an aluminium-magnesium-rich gabbro with a mineralogical assemblage of epidote+chlorite+talc+calcic-amphibole is stable at blueschist P-T conditions (9-12 kbar and 380-420°C; Ring, 1992) (figure 3.17).

Furthermore, glaucophane would be an amphibole anticipated to form at blueschist facies conditions. Experimental studies have demonstrated that Mg-end-member glaucophane is not stable at 12kbar and 400°C (Corona, 2005; Bang et al., 2021), placing Avers Bündnerschiefer at the reactant's side of the reaction (R5) (figure 4.1).

2 Albite + Talc → Glaucophane + 2 Quartz (R5)

It should be acknowledged that glaucophane's stability field increases to lower P-T conditions with increasing Fe^{2+} concentrations (Corona, 2005). However, a Fe-depletion in the Juf Gabbro's bulk composition is inferred by the colourless pleochroism of epidote, chlorite, and calcic-amphiboles in the Juf Gabbro. Therefore, it suggests that a close-to end-member glaucophane composition is required for glaucophane growth.

The older top-WNW tectonometamorphic imprint is also the primary phase of the calcschist surrounding the Juf Gabbro (figure 3.8), suggesting both to have experienced the same tectonic path. The ATMZ does not overprint this calcschist, despite its ductility and proximity to the ATMZ. This leaves two conclusions: either a lithologies ductility does not reveal whether or not it is likely to be overprinted, or the calcschist current proximity to the ATMZ cannot represent its position during the top-SE return flow event.

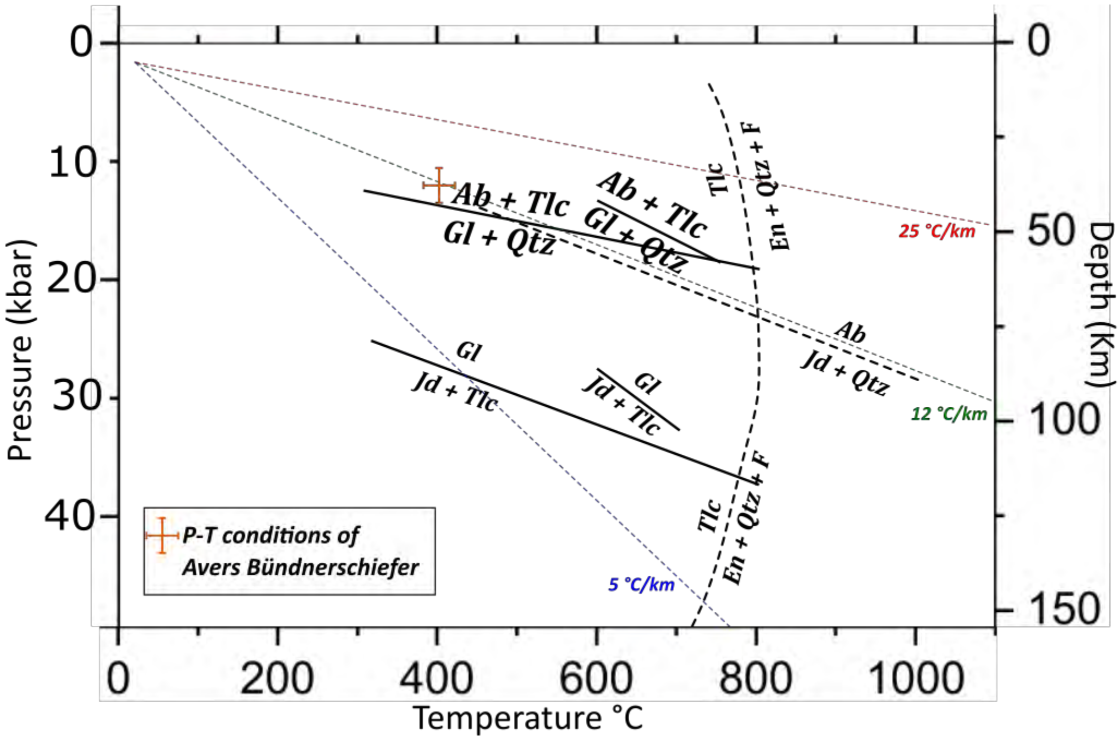

Figure 5.1 is a P-T diagram showing the stability field of the Mg-end-member glaucophane. The diagram was modified from Bang et al. (2021). Abbreviations used: Ab = Albite, Tlc = Talc, Gl = Glaucophane, Qtz = Quartz, En = Enstatite, F = Flourite and Jd = Jadite.

5.12 D2-folding and its influence over D1-structures

The S_1 foliation planes and stretching lineations are rotated by south-vergent folds with E-W trending fold axes and N-dipping axial planes – marking the D2 stage. These folds are rotating the early S_1 foliation into the N-dipping direction of the axial planes. The south-vergent nature of the folds (top-to-the-S) aligns with the kinematics of the overlying ATMZ. Therefore, the timing of this event would be expected to correlate with the top-to-the-SE-directed shearing of the ATMZ (45 – 34 Ma, Ring & Glodny, 2021). Moreover, the Juf Gabbro is deprived of fluids and lies tectonically below the ATMZ; therefore, the top-to-the-SE folding does not develop any axial planar mineral growth.

Some of the scatter observed in the highly deformed metagabbro's stretching lineations can be attributed to the D2 folding (figure 3.10). This stage shows variable fold axes at an angle to the earlier lineation; therefore, the earlier stretching lineation scatters around the fold axes. This relationship is seen in figure 4.2, where there is little overlap between fold axes and lineation trends in the highly deformed metagabbro. However, this does not seem to influence the mylonitic lithologies in the same way; suggestively, the higher anisotropy of the mylonitic lineation causes the fold axes to be parallel. At the same time, the weakly-to-intermediately metagabbro does not experience the same scatter because most folding was recorded in the foliated segments of the intermediately deformed metagabbro. Here, the folding remains parallel due to the foliated segment's position between the two more massive, cohesive metagabbro segments. Furthermore, some of the fold axes data variability is associated with the massive peridotite at Piotjoch (figure 3.12). The rigid peridotite does not deform ductilely; therefore, most deformation is accommodated to the surrounding metagabbro, subsequently folding it.

The folding of D1-stretching lineations implies an inversion of the shear-sense in the short limbs of the folds (figure 3.13). This inversion is hardly observed; instead, about 80% of the shear-sense-indicators are top-to-the-WNW (Table 3.1). This is due to most shear-sense indicators being retrieved from outcrops from the fold's long limbs – where the orientation of structures is not disturbed by folds. The closer one gets to the hinge of the fold, the frequency of parasitic folds increases. Hence, when an outcrop exhibiting pronounced folding is examined, shear-sense indicators are not recorded, and therefore inverted shear-sense in the fold's short limbs is not recorded. Moreover, a bi-product of the fold's asymmetry leads to higher availability of outcrops from the long limbs (figure 3.13). Therefore most outcrops in

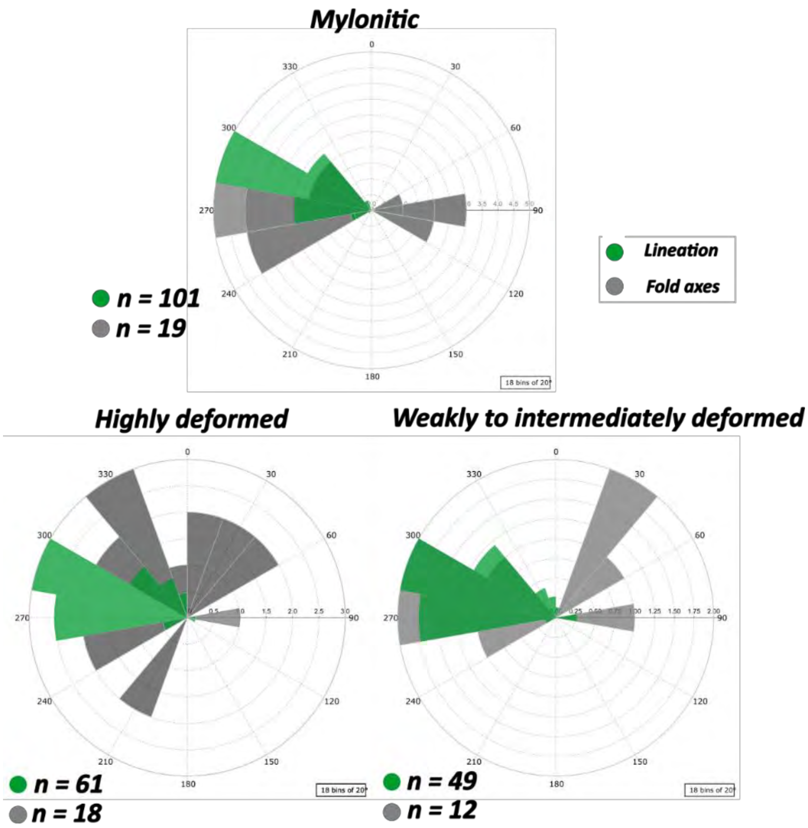

Figure 5.2 is a Rose plot containing trend data from stretching lineation and fold axes from all the different metagabbro deformational intensities capable of exhibiting such structures. Dark green is indicating overlap in lineation and fold axes data.

the study area are the folds' long limbs, which expect to have ordinary, top-to-the-WNW shear-sense.

5.13 The D3 folds and D4 faults

The third deformation phase (D3) is suggested by refolding N-dipping D2 axial planes by NW fold axes, observed in figure 3.14. This phase has previously been described north of the Engadine line by Liniger and Nievergelt (1990) as N-vergent folds with NE-SW trending axes causing the steepness of the ATMZ near Piz Turba (figure 1.5); therefore, it must have occurred after 34 Ma. Furthermore, some NE-SW trending axes influence both the highly and weakly-to-intermediately deformed intensity (figure 5.2). However, the axial plane data does divert significantly from the D2-N-dipping axial planes, and no overprinting relationship was observed in the field. Therefore, D3 folding must only have had a local influence.

The fourth deformational phase (D4) is defined by the cataclastic extensional top-E/NE normal faulting and sinistral strike-slip movement with its principal activity along the Juferjoch fault and minor displacements along other normal faults within the study area. This faulting can be correlated with the N-S striking sinistral normal faulting described in Platta nappe (Liniger and Nievergelt 1990).

5.2 Fluid-rock interaction

The macroscopic and microscopic results indicate that the Juf Gabbro is a fluid deficient mafic body, with incomplete reactions reflected by the porhyroclastic relicts in weakly deformed to mylonitic metagabbro. It is shown that the abundance of porphyroclastic relicts decreases with increasing deformation intensity. Therefore, the small amount of localised fluid flow penetrates fractures within the Juf Gabbro, facilitating the breakdown of augite to form an early foliation of planar talc and chlorite (figure 3.15). These regimes now accommodate most strain accumulation and shearing, as well as channelising fluid flow. The initial entry point of the fluid penetrating the gabbro must have been along with a permeable contact to the calcschist. This is why the highest amount of volatile content is observed at the northern boundary (figure 4.2), comprising a discontinuous ultra-mylonitic talc-schist layer.

Moreover, samples retrieved proximal to the northern boundary are generally depleted in plagioclase (e.g., G46 and G98; table 4.1 and figure 3.1). This is due to fluid facilitated mineral reactions such as porphyroclastic plagioclase → epidote fractures the rock due to the product having a higher density than the reactant, taking up a lower volume (Ague, 2003) – providing a mechanism of how an impermeable gabbro eventually fractures and is permeated by fluid.

Another query is why the high degree of carbonisation is localised to the peak SE of Juferhorn (figure 3.1)? The metagabbro's mineralogical composition controls the fluid-rock alteration during fluid flow. Table 4.1 reveals that hydrated metagabbro samples are more depleted in plagioclase compared to carbonates samples. This suggests that carbonation occurs where the metagabbro includes a higher plagioclase concentration from the primary bulk composition, or the carbonated samples experienced less prograde growth of epidote. The latter case implies that the main fluid flow event along the northern boundary occurred after the growth of epidote. This is corroborated by figures 3.15 g-h – showing plagioclase replacement by complete growth of large epidote crystal growth and an incomplete reaction of plagioclase →

calcite. In order to figure out this question in more detail, one would have to map out the chemical composition of the plagioclase to separate igneous anorthite from albite.

5.3 Tectonic interpretation

This study demonstrates that mylonitic top-WNW-shearing is the primary deformational phase influencing the Juf Gabbo. The top-WNW-shearing must have penetrated down to Upper Pennine basal structural levels and has, in part, incorporated mantle rocks. The event must be older than 45 Ma (Ring & Glodny, 2021) due to being crosscut by the ATMZ (figure 1.5). The top-WNW-shearing is kinematically sound with the overlying nappes formed through imbrication during the Cretaceous to Paleogene paleo-subduction zone (Handy et al., 1996) (Dallmeyer et al., 1998). The higher tectonostratigraphic nappes (The Err and Arosa-Platta nappes) experienced top-W-directed imbrication under greenschist conditions in the overriding plate. This is dated to 76-89 Ma in Platta-Err nappe (Handy et al. 1996), with the latest top-W-shearing dated to 50 Ma in the Arosa unit - interpreted as the abandonment of the paleo-subduction zone associated with dehydration and fluid activity (Bachmann et al., 2009). On the other hand, the Avers Bündnerschiefer experienced top-WNW-shearing during blueschist facies metamorphism within the subduction channel (Ring, 1992). According to Bachmann's interpretation, this must have occurred before 50 Ma.

These results directly conflict with the long-held tectonic model by Schmid et al. (1996), arguing for Avers Bündnerschiefer being formed due to N-S shortening during Paleogene convergence. In contrast, this study argues that the Piemont-Ligurian ocean is incorporated into the Cretaceous to Paleogene top-WNW-directed imbrication, ultimately forming the Avers Bündnerschiefer (figure 5.3) during the early Eocene. This suggests that the rotation in the Adria plate was WNW-directed for the period involving the Upper and Middle Pennine domain subduction, reworking Austroalpine and Upper Pennine domain through top-WNW-directed imbrication. Therefore, Avers Bündnerschiefer must have been a coherent tectonic unit once affected by the later N-S shortening.

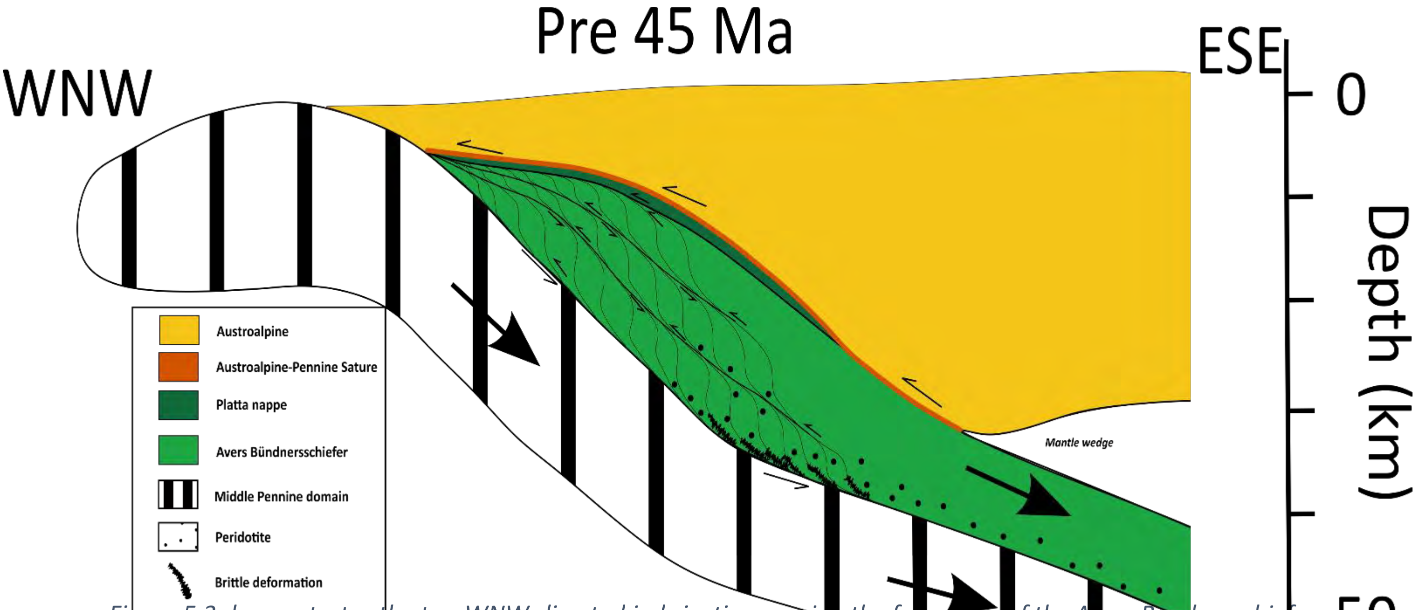

Figure 5.3 demonstrates the top-WNW-directed imbrication causing the formation of the Avers Bündnerschiefer and forming the lensiondal pattern through shear between major thrusts. This occurred prior to 45 Ma until the introduction of the backfolding event and the top-SE displacing ATMZ.

Moreover, the Juf Gabbros lensiodal pattern suggestively formed due to shear fabrics connecting major thrusts during the imbrication (figure 5.3). These thrusts must have, in part, cataclastically fractured the ultramafic peridotite base allowing for fluid flow, which promotes serpentine formation. The ductility of serpentine allows for rigid pods of peridotite to be transported and incorporated into the imbrication. Speculatively, the top-WNW-directed imbrication ceased once the orogen shifted from an accretionary to a collisional state and abandoned the paleo-subduction zone at 50 Ma due to the introduction of the European margin followed by the top-SE displacing folding.

This study, among others (e.g., Régnier et al., 2003; Compagnoni, 1977), has demonstrated that lithologies can retain early tectonometamorphic imprints as their primary phase despite being involved in several later overprinting events. Therefore, seeking further evidence for these early Alpine kinematics within the Pennine domain can determine how deep the tectonometamorphic imprint reaches down the tectonic pile. Moreover, a further inquiry into how and why early tectonometamorphic imprints are retained would alleviate exploring the early tectonic stages of an orogen.

6. Conclusions

1. The early top-WNW kinematics characteristic of the Cretaceous to Paleogene imbrication is the main tectonometamorphic imprint of the Juf Gabbro.
2. The high-P Madris-metabasalt, the calcschist and the Juf Gabbro share the same tectonic history and, therefore, formed together under blueschist facies conditions as a part of the top-WNW-directed imbrication of the Piemont-Ligurian ocean during the early Eocene. The Juf Gabbro does not develop a high-P mineral assemblage due to its Al-Mg-rich bulk composition.
3. The Juf Gabbro remains largely unaffected by later orogenic events.

Acknowledgements

Stockholm University funded this master thesis. I would like to thank my supervisor, Uwe Ring, for the continuous support, productive arguments, structural guidance and supervision during the thesis. I would like to thank Alasdair Skelton for the productive sorting of the metamorphic story. Paola Manzotti and Francesco Nosenzo for their thoughts on mineral identification. Robert Dunst for introducing me to Alpine literature. Sandra Morawiecki and William Westin for the continual moral support and the rest of the department.

References

Ague, J. J., & Rudnick, R. L. (2003). Fluid flow in the deep crust. *The crust*, *3*, 195-228.

Bachmann, R., Glodny, J., Oncken, O., & Seifert, W. (2009). Abandonment of the South Penninic–Austroalpine palaeosubduction zone, Central Alps, and shift from subduction erosion to accretion: constraints from Rb/Sr geochronology. *Journal of the Geological Society*, *166*(2), 217-231.

Bang, Y., Hwang, H., Kim, T., Cynn, H., Park, Y., Jung, H., ... & Lee, Y. (2021). The stability of subducted glaucophane with the Earth's secular cooling. *Nature communications*, *12*(1), 1-7.

Butler, J. P., Jamieson, R. A., Steenkamp, H. M., & Robinson, P. (2013). Discovery of coesite–eclogite from the Nordøyane UHP domain, Western Gneiss Region, Norway: field relations, metamorphic history, and tectonic significance. *Journal of Metamorphic Geology*, *31*(2), 147-163.

Carminati, E., & Doglioni, C. (2012). Alps vs. Apennines: the paradigm of a tectonically asymmetric Earth. *Earth-Science Reviews*, *112*(1-2), 67-96.

Compagnoni, R. (1977). The Sesia-Lanzo Zone: high pressure-low temperature metamorphism in the Austroalpine continental margin. *Rendiconti della Societa Italiana di Mineralogia e Petrologia*, *33*, 335-378.

Corona, J. C. (2005). *An experimental investigation of the reaction: glaucophane+ 2 quartz= 2 albite+ talc*. State University of New York at Binghamton.

Dallmeyer, R. D., Handler, R., Neubauer, F., & Fritz, H. (1998). Sequence of thrusting within a thick-skinned tectonic wedge: Evidence from 40Ar/39Ar and Rb-Sr ages from the ANC of the Eastern Alps. *The Journal of geology*, *106*(1), 71-86.

Engi, M., Bousquet, R., & Berger, A. (2004). Explanatory notes to the map: metamorphic structure of the Alps. In *Central Alps. Mitt. Österr. Miner. Ges*.

Froitzheim, N., Pleuger, J., & Nagel, T. J. (2006). Extraction faults. *Journal of Structural Geology*, *28*(8), 1388-1395.

Froitzheim, J., Meier, G. H., Niewolak, L., Ennis, P. J., Hattendorf, H., Singheiser, L., & Quadakkers, W. J. (2008). Development of high strength ferritic steel for interconnect application in SOFCs. *Journal of Power Sources*, *178*(1), 163-173.

Gianola, O., Schmidt, M. W., von Quadt, A., Peytcheva, I., Luraschi, P., & Reusser, E. (2014). Continuity in geochemistry and time of the Tertiary Bergell intrusion (Central Alps). *Swiss Journal of Geosciences*, *107*(2), 197-222.

Gregory, C. J., McFarlane, C. R., Hermann, J., & Rubatto, D. (2009). Tracing the evolution of calc-alkaline magmas: in-situ Sm–Nd isotope studies of accessory minerals in the Bergell Igneous Complex, Italy. *Chemical Geology*, *260*(1-2), 73-86.

Handy, M. R., Herwegh, M., Kamber, B. S., Tietz, R., & Villa, I. M. (1996). Geochronologic, petrologic and kinematic constraints on the evolution of the Err-Platta boundary, part of a fossil continent-ocean suture in the Alps (eastern Switzerland). *Schweizerische Mineralogische und Petrographische Mitteilungen*, *76*(3), 453-474.

Holland, T. J. B., & Powell, R. T. J. B. (1998). An internally consistent thermodynamic data set for phases of petrological interest. *Journal of metamorphic Geology*, *16*(3), 309-343.

Liati, A., Gebauer, D., & Fanning, M. (2000). U-Pb SHRIMP dating of zircon from the Novate Granite (Bergell, Central Alps); evidence for Oligocene-Miocene magmatism, Jurassic/Cretaceous continental rifting and opening of the Valais Trough. *Schweizerische mineralogische und petrographische Mitteilungen*, *80*(3), 305-316.

Liniger, M. und Nievergelt, P. (1990). Stockwerktektonik im südlichen Graubünden. Schweiz. Mineral. Petrogr. Mitt. 70, 95–101.

Lippitsch, R., Kissling, E., & Ansorge, J. (2003). Upper mantle structure beneath the Alpine orogen from high-resolution teleseismic tomography. *Journal of Geophysical Research: Solid Earth*, *108*(B8).

Malusà, M. G., Faccenna, C., Garzanti, E., & Polino, R. (2011). Divergence in subduction zones and exhumation of high-pressure rocks (Eocene Western Alps). *Earth and Planetary Science Letters*, *310*(1-2), 21-32.

Malusà, M. G., Faccenna, C., Baldwin, S. L., Fitzgerald, P. G., Rossetti, F., Balestrieri, M. L., ... & Piromallo, C. (2015). Contrasting styles of (U) HP rock exhumation along the Cenozoic Adria-Europe plate boundary (Western Alps, Calabria, Corsica). *Geochemistry, Geophysics, Geosystems*, *16*(6), 1786-1824.

Manzotti, P., Ballèvre, M., Pitra, P., Putlitz, B., Robyr, M., & Müntener, O. (2020). The growth of sodic amphibole at the greenschist-to blueschist-facies transition (Dent Blanche, Western Alps): bulk-rock chemical control and thermodynamic modelling. *Journal of Petrology*, *61*(4), egaa044.

Mohn, G., Manatschal, G., Masini, E., & Müntener, O. (2011). Rift-related inheritance in orogens: a case study from the Austroalpine nappes in Central Alps (SE-Switzerland and N-Italy). *International Journal of Earth Sciences*, *100*(5), 937-961.

Mohn, G., Manatschal, G., Beltrando, M., & Haupert, I. (2014). The role of rift-inherited hyper-extension in Alpine-type orogens. *Terra Nova*, *26*(5), 347-353.

Natland, J. H., Dick, H. J. B., Miller, D. J., & Von Herzen, R. P. (2002). 12. Major and Trace Element Evolution of Hole 735B Gabbros.

Oberhänsli, R. Von. (1978). Chemishe Untersuchungen an Glaukophan-Führenden basishen Gesteinen aus den Bünderschiefern Graubünden. Schweiz mineral petrology. Mitt. 58, 139-156.

Peacock, S. M. (1989). Thermal modeling of metamorphic pressure-temperature-time paths: A forward approach. *Metamorphic Pressure-Temperature-Time Paths*, *7*, 57-102.

Platt, J. P. (1986). Dynamics of orogenic wedges and the uplift of high-pressure metamorphic rocks. *Geological society of America bulletin*, *97*(9), 1037-1053.

Price, J. B., Wernicke, B. P., Cosca, M. A., & Farley, K. A. (2018). Thermochronometry Across the Austroalpine-Pennine Boundary, central Alps, Switzerland: Orogen-perpendicular normal fault slip on a major "overthrust" and its implications for orogenesis. *Tectonics*, *37*(3), 724-757.

Price, J. B., Wernicke, B. P (Unpublished, Manuscript 80957). Kinematic analysis of the upper and lower boundaries of the Pennine Zone, Oberhalbstein and Vorderrhein regions, Switzerland, and implications for orogenesis. The Journal of Geology.

Régnier, J. L., Ring, U., Passchier, C. W., Gessner, K., & Güngör, T. (2003). Contrasting metamorphic evolution of metasedimentary rocks from the Cine and Selimiye nappes in the Anatolide belt, western Turkey. *Journal of Metamorphic Geology*, *21*(7), 699-721.

Ring, U. (1992). The Alpine geodynamic evolution of Penninic nappes in the eastern Central Alps: geothermobarometric and kinetic data. Journal of metamorphic Geology,10, 33-53.

Ring, U., & Glodny, J. (2021). The importance of tangential motion in the Central Alps: Kinematic analysis and RbSr dating of mylonitic rocks from the Pennine nappes in the eastern Central Alps. Earth-Science Reviews, 103644.

Schenker, F. L., Schmalholz, S. M., Moulas, E., Pleuger, J., Baumgartner, L. P., Podladchikov, Y., ... & Müntener, O. (2015). Current challenges for explaining (ultra) high-pressure tectonism in the Pennine domain of the Central and Western Alps. *Journal of Metamorphic Geology*, *33*(8), 869-886.

Schlunegger, F., & Castelltort, S. (2016). Immediate and delayed signal of slab break-off in Oligo/Miocene Molasse deposits from the European Alps. *Scientific reports*, *6*(1), 1-11.

Schmid, S. M., Pfiffner, O. A., Froitzheim, N., Schönborn, G., & Kissling, E. (1996). Geophysical-geological transect and tectonic evolution of the Swiss-Italian Alps. *Tectonics*, *15*(5), 1036-1064.

Schmid, S. M., & Kissling, E. (2000). The arc of the western Alps in the light of geophysical data on deep crustal structure. *Tectonics*, *19*(1), 62-85.

Schmid, S. M., Fügenschuh, B., Kissling, E., & Schuster, R. (2004). Tectonic map and overall architecture of the Alpine orogen. *Eclogae Geologicae Helvetiae*, *97*(1), 93-117.

Schreurs, G. (1993). Structural analysis of the Schams nappes and adjacent tectonic units; implications for the orogenic evolution of the Penninic Zone in eastern Switzerland. *Bulletin de la Société géologique de France*, *164*(3), 415-435.

Selverstone, J. (2005). Are the Alps collapsing?. *Annual Review of Earth and Planetary Sciences*, *33*.

Stampfli, G. M., Mosar, J., Marquer, D., Marchant, R., Baudin, T., & Borel, G. (1998). Subduction and obduction processes in the Swiss Alps. *Tectonophysics*, *296*(1-2), 159-204.

Trommsdorff, V., Evans, B.W., 1974. Alpine Metamorphism of Peridotitic Rocks. Schweiz. Mineral. Petrogr. Mitt. 54, 333–352.

Tullis, J. (2018). Deformation of feldspars. In *Feldspar mineralogy* (pp. 297-323). De Gruyter.

Whitney, D. L., & Evans, B. W. (2010). Abbreviations for names of rock-forming minerals. *American mineralogist*, *95*(1), 185-187.

Wilson, M. (1989) Igneous Petrogenesis: A Global Tectonic Approach. Unwin Hyman, London, 466 p.

Supplementary Material

Thin section observations

Here are all the thin-section descriptions used for the Masters thesis. The abbreviations used in figures are by Whitney and Evans, (2010), as following: Tur = Tourmaline, Aug = Augite, Cam = Calcic-amphibole, Pl = Plagioclase, Ep = Epidote; Tnt = Titanite, Hem = Hematite; Rbk = Riebeckite, Cal = Calcite; Qz = Quartz, Wm = White Mica; Chl = Chlorite, and Tlc = Talc.

G1T

- **Lithology**: Metagabbro
- **Field measurements: 46°25'12"N, 09°34'59"E** and Mylonitic texture.
  - stretching lineation trend = 280W
- **Hand sample:** A turquoise green flaky rock whose layers fall apart without effort is easily scratched by a fingernail. The core of the layer is harder and is, therefore, what ended up in the thin section.
- **Mineralogy:** Tlc, Chl, Ep, Cam, and Pl.
- **Texture:** Mylonitic
  - A mylonitic texture encompasses porphyroblasts of Pl, Cam and Ep rotating between shear bands of Chl and Tlc. The porphyroblasts show strain-shadows of Chl and asymmetrical clusters of Tlc reflecting a sinistral top-W. Subrounded and randomly oriented crystals of Ep are rotating within the micaceous matrix. These ep crystals are pale-pleochroic and reflect a blue-birefringence. Furthermore, pale-pleochroic cam crystals are replaced by pale-pleochroic Chl (figure 1).
  - **Sense of shear: Top-to-the-west**
- **Sequence summary:**
  - Igneous relics are not present here
  - Pre deformational growth of Pl and Cam.
  - Syn deformational growth of Chl and Tlc.
  - Post deformational growth of Ep.

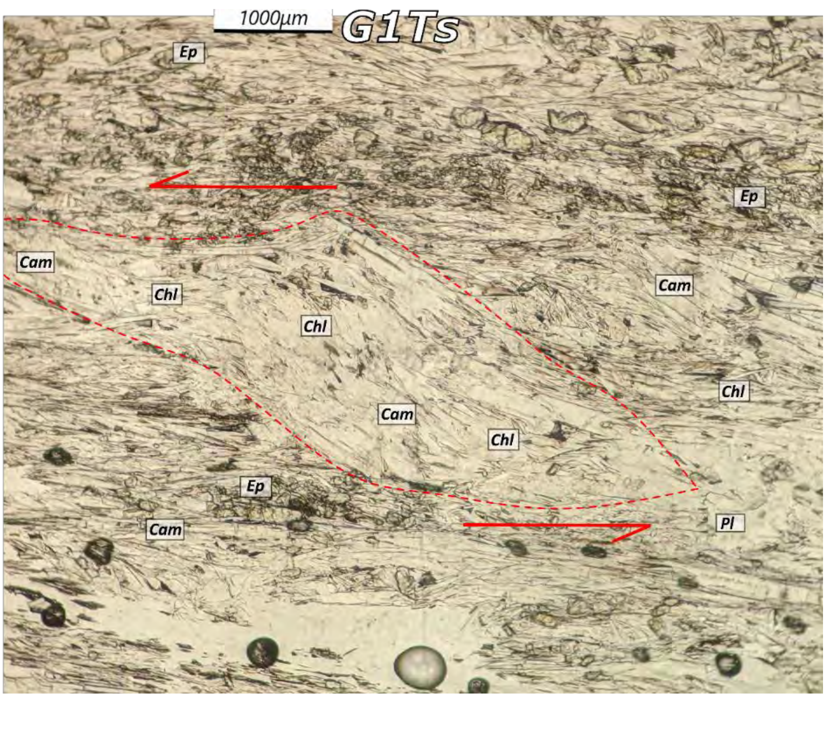

Figure 1 displays the disequilibrium of calcic-amphibole crystals in an ultra-mylonitic talc-schist sample, calcic-amphibole are replaced by colourless pleochroic chlorite with a sinistral top-W shear component. W is to the left.

G3s

- **Lithology**: Metagabbro
- **Field measurements: 46°25’10”N, 09°34’58”E**. Mylonitic texture.
    - Stretching lineation trend = 285W
- **Hand Sample:** Mylonitic rock with slightly curved carbonate layers in it (mm thickness).
- **Mineralogy:** Cal, Ep, Chl, Pl, Qz and Tlc, with minor Cam, Ttn and Hem.
- **Texture:** Mylonitic
    - Mylonitic texture with larger crystals of Cal, Qz and Ep. Ep, Tlc, Cal and Qz all grew contemporaneous with mylonitization. The deformation is concentrated in high strain top W shear bands containing Cal and Chl with rotated Ep-crystals reflecting top-W shear sense. Larger asymmetrical clusters of Tlc also reflect top-W movement. Pl are only observed in disequilibrium being replaced by Cal and Ep. Cal, fine-grained Ep and Qz form bands, dividing the more micaceous layers (figure 2).
    - **Sense of shear: Top-to-the-west**
- **Sequence summary:**
    - Pre deformational growth of Pl, Cam and Hem.
    - Syn deformational growth of Cal, Ep, Chl and Ttn
  - Post deformational growth of fine-grained Ep.

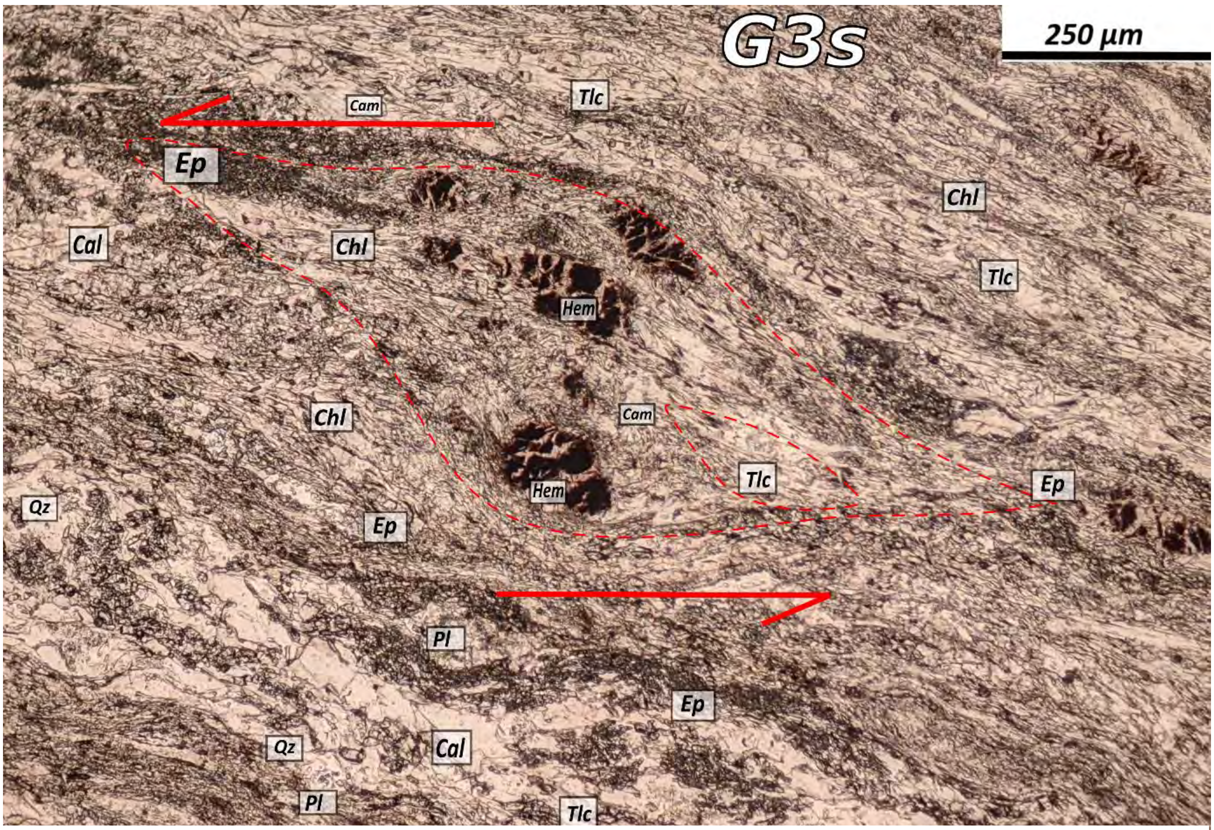

Figure 2 is a carbonated mylonitic metagabbro showing plagioclase replaced by epidote, and carbonate, in addition to a 2nd order calcic-amphibole being replaced by hematite; all indicating a top-W sinistral shear-sense. W is to the left.

G4s

- **Lithology**: Metagabbro
- **Field measurements: 46°25′09″N, 09°35′08″E**. Mylonitic texture.
    - Stretching lineation trend = 269W
- **Hand sample:** A highly deformed white rock with greenish layers in it.
- **Mineralogy:** Pl, ep, Cam, tlc, chl and ep
- **Texture:** Mylonitic
    - The deformation is focused on a foliation of fine-grained pale-pleochroic ep, chl and tlc layers growing around porhyroclastic Pl-crystals. Growth of Ep is rimming and internally replacing porphyroclastic Pl. Pl is also present as more anhedral elongated forms within the high strain layers consisting of fine-grained Ep, Tlc, Chl and Qz. Chl makes up strain shadows of rotated cam-crystals reflecting top-W shearing. Conflicting shear-sense are observed in the thin section, however, a majority still reflect top-W (sinistral) asymmetry (figure 3).
    - **Sense of shear: Somewhat conflicting, but majority top-to-the-west**
- **Sequence summary:**
    - Igneous relics: poikilitic Pl.
    - Pre deformational growth of Cam and Pl
    - Syn deformational growth of Ep, Chl and Tlc.
    - Post deformational growth: not clear

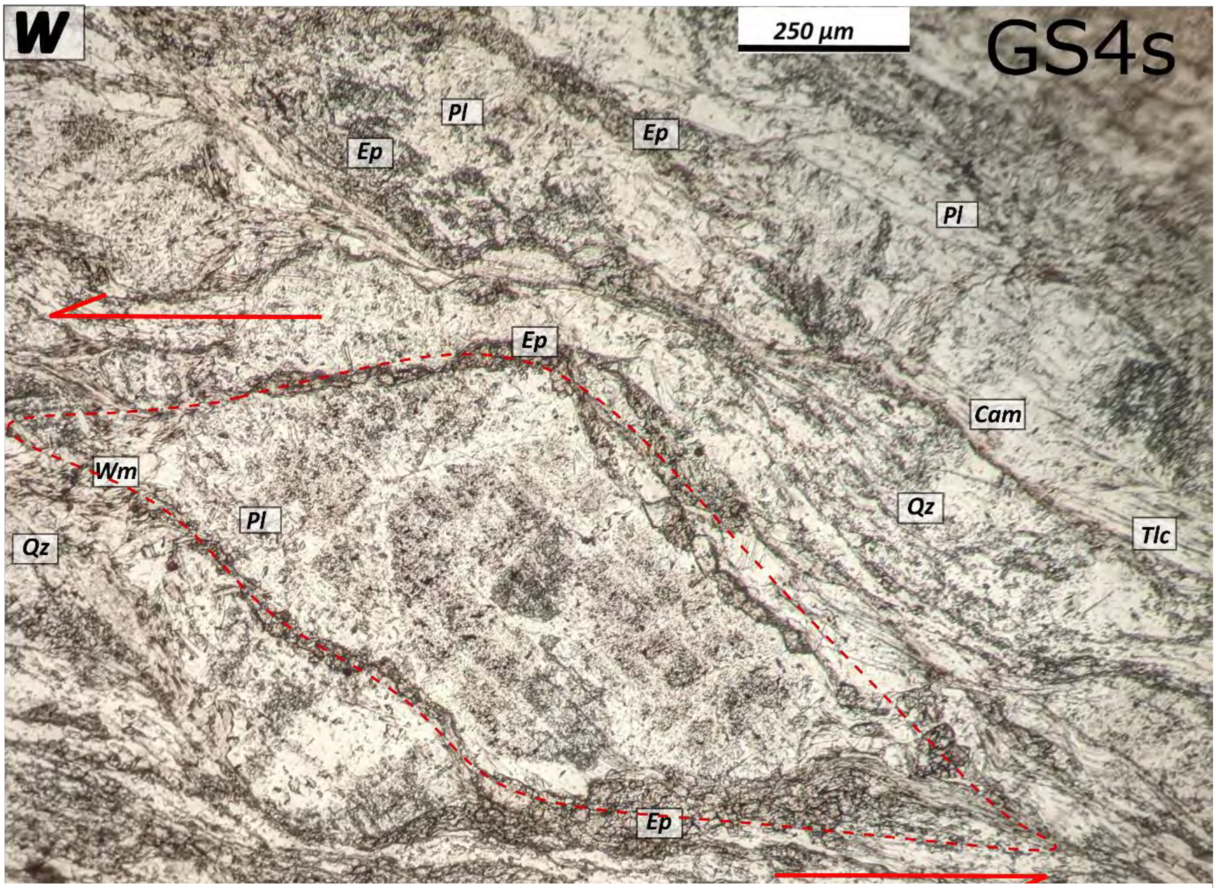

Figure 3 showing porhyroclastic plagioclase rimmed by epidote reflecting a sinistral top-W assymetry.

G7s

- **Lithology**: Metagabbro
- **Field measurements: 46°25’07”N, 09°35’24”E.** Highly Deformed,
    - Stretching lineation trend = 272W
- **Hand Sample:** Pitted weathering, clear but wavy foliation with a greenish-yellow sheen to it.
- **Mineralogy:** Ep, Chl, Qz, Pl, Cam, tlc, Wm and ttn
- **Texture:**
    - The deformation is concentrated in discontinuous top-W shear bands of Chl and fine-grained Ep with some anhedral elongated Pl incorporated. Within the discontinuity of the layers, there are cam-crystals rotated from the main foliation direction among with porphyroclastic growth of pl. All of these porphyroclastic Pl have inclusions of Ep. SW dipping folds are visible throughout the thin section. Chl is making up strain-shadows of asymmetrically top-W sheared Pl (figure 4)
    - **Sense of shear: Top-to-the-west**
- **Sequence summary:**
    - Igneous relics are poikilitic Pl.
    - Pre deformational growth of Pl and Cam
    - Syn deformational growth of Chl, Tlc, Ep and Plg
    - Post deformational growth of Ep and Qz

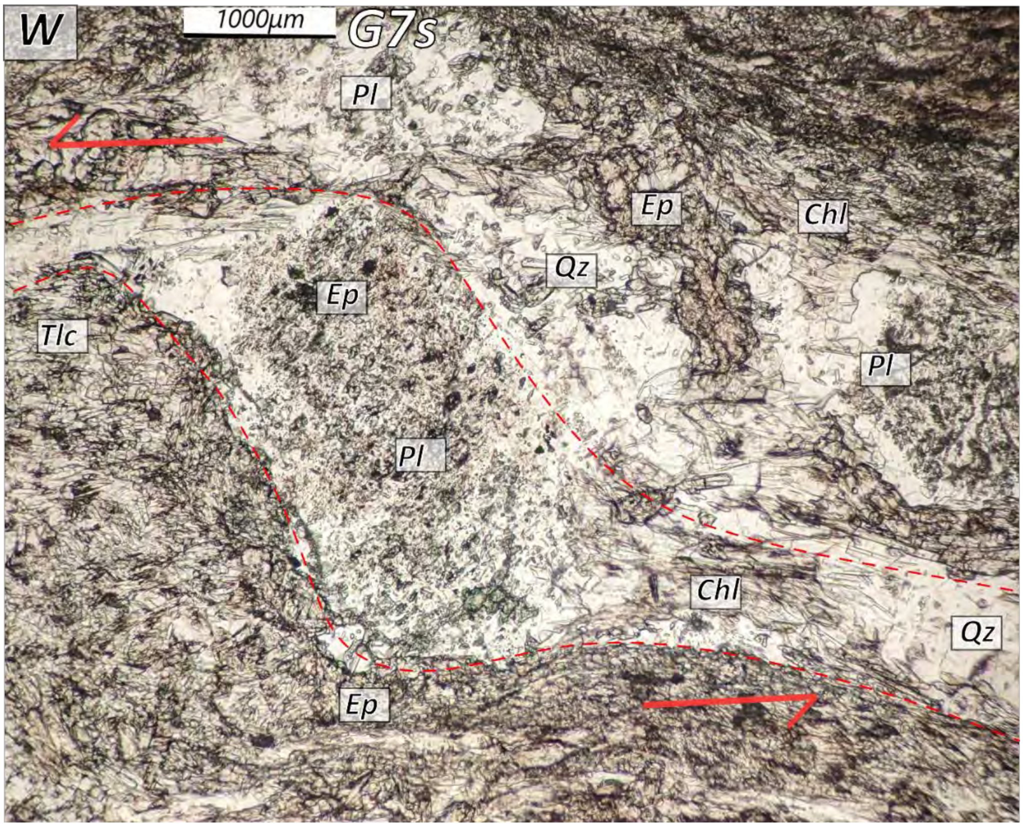

Figure 4 showing a assymetrically top-W (sinistral) sheared plagioclase crystal with chlorite making up strain shadown.

G14As

- **Lithology**: Metagabbro
- **Field measurements: 46°24’51.62”N, 09°35’08.48”E.** Mylonitic texture.
  - Stretching lineation trend = 296W
- **Hand Sample:** White mylonitic rock with whitish-yellow and whitish-green fine layers.
- **Mineralogy:** Ep, Pl, Qz, Cam, Chl, Tlc, and Wm
- **Texture:** mylonitic
  - Deformation is concentrated in shear bands of fine-grained Ep, Tlc, Chl and minor Wm with some Qz-bands incorporated. In between the shear bands, porphyroblasts of Ep and Cam are growing, with more fine-grained clustered growth of Chl, Tlc and Wm in between, all displaying top-W sheering. Calcite is replacing Pl in Qz + Pl boudins (figure 5). An Ep-crystal with andalose-blue birefringence inclusions reflects a top-W asymmetry (figure 5). Chl is the main constituent of strain shadows around porphyroblasts. Cam is rotated to an angle of ~ 30° from the foliation.
  - **Sense of shear: Top-to-the-west**
- **Sequence summary:**
  - Igneous relics are not visible.
  - Pre deformational growth of amphiboles, larger zoisite and epidote crystals.
  - Syn deformational growth of clinozoisite, Ccl, Wm and Ta.
  - Post deformational growth is unclear.
  -

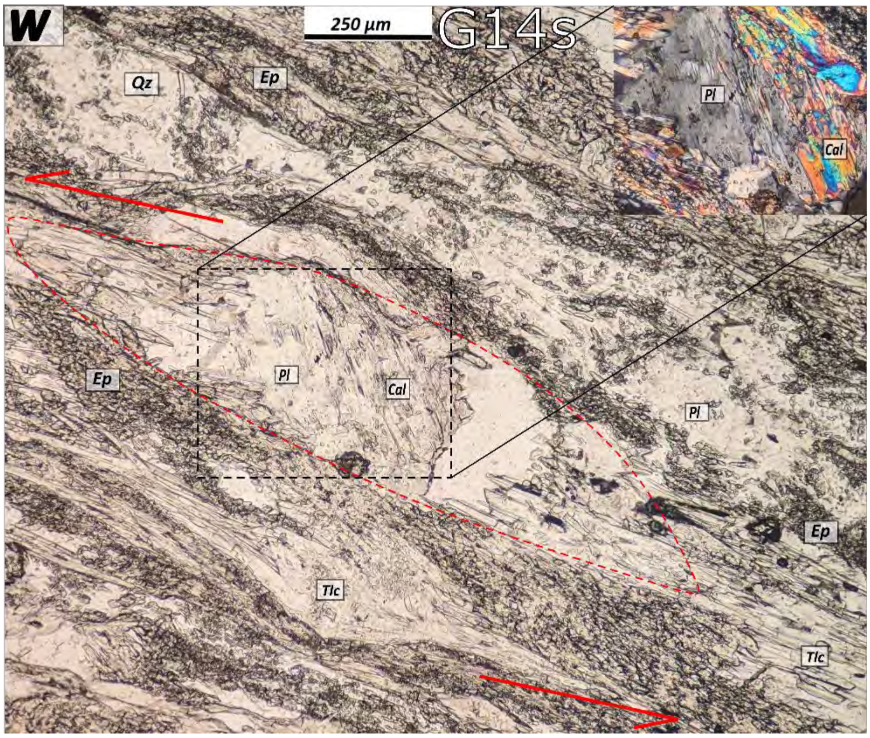

Figure 5 shows a Pl-Qz-boudin, with a Pl-crystal being cataclastically fractured and replaced by Cal. The entire boudin asymmetry indicates top-W (sinistral shearing).

G18s

- **Lithology**: Metagabbro
- **Field measurements: 46°25’00.34”N , 09°35’29.03”E.** Highly Deformed,
    - Stretching lineation trend = 294 W
- **Hand Sample:** Coarse-grained foliation with thick layers of a yellowish-green colour and thinner layers of green. Pitted weathering is observed.
- **Mineralogy:** Ep, Tlc, Chl, Cam, Pl, Wm, and Qz
- **Texture:**
    - The thin section does not exhibit a clear cohesive foliation. A preferred orientation is only observed in tlc and chl rich regimes within a matrix consisting primarily of Ep and Qz (figure 6). The deformation is concentrated in larger Ep-crystals, in addition to Tlc and Cam layers. Two calcic-amphiboles are identified. The first is pale-pleochroic, anhedral to subhedral in shape, and reflects an equilibrium with Chl, Ep and tlc, whereas the second type is rhombic crystals that are partly replaced by chl. Pl only appear in shear bands displaying a disequilibrium by being replaced by Ep. The thin section displays northerly dipping folds with no axial planar growth of minerals.
    - **Sense of shear: No clear asymmetry visible.**
- **Sequence summary:**
    - Igneous relics are not visible.
    - Pre deformational growth of Cam
    - Syn deformational growth of Ep, Chl, Tlc, and Wm.
    - Post deformational growth is unclear.

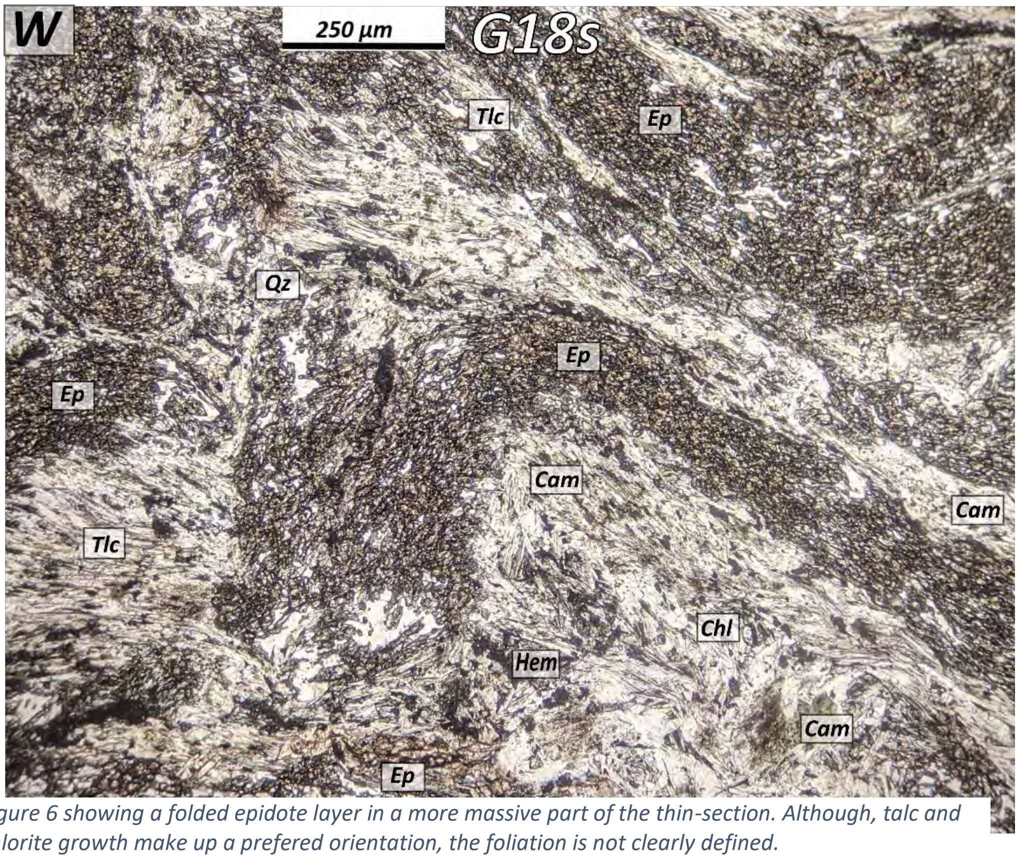

Figure 6 showing a folded epidote layer in a more massive part of the thin-section. Although, talc and chlorite growth make up a prefered orientation, the foliation is not clearly defined.

G18s1

- **Lithology**: Metagabbro
- **Field measurements: 46°25'00.34"N, 09°35'29.03"E.** Highly Deformed.
  - Stretching lineation trend = 294W
- **Hand sample:** Coarse-grained foliation with thick layers of a yellowish green colour and thinner layers of green.
- **Mineralogy:** Pl, Cam, Ttn, Chl, Ep, Wm, Qz and minor Hem
- **Texture:**
  - The majority of the thin section is largely undeformed with considerable subhedral growth of porthyroclastic Pl and rhombic hornblende dominate the thin section's massive sections. The massive sections are split up by the growth of Chl, elongated Cam and Ttn, and minor Wm - making up the main foliation, with fine-grained Ep and Qz growing alongside it (figure 7). Furthermore, Chl grows in the pressure shadows of porphyroblastic elongated Cam, which are often rotated to 30° from the main foliation and show green pleochroism. The fine-grained matrix consists of Ep and Q, which show no clear signs of deformation. This rock is largely undeformed, showing no apparent asymmetry.
  - **Sense of shear: Asymmetry not clear.**
- **Sequence summary:**
  - Igneous relics of Pl and hornblende
  - Syn deformational growth of Ttn, Chl, Elongated Cam, Wm and Ep.
  - Post deformational growth of Ep and Qz

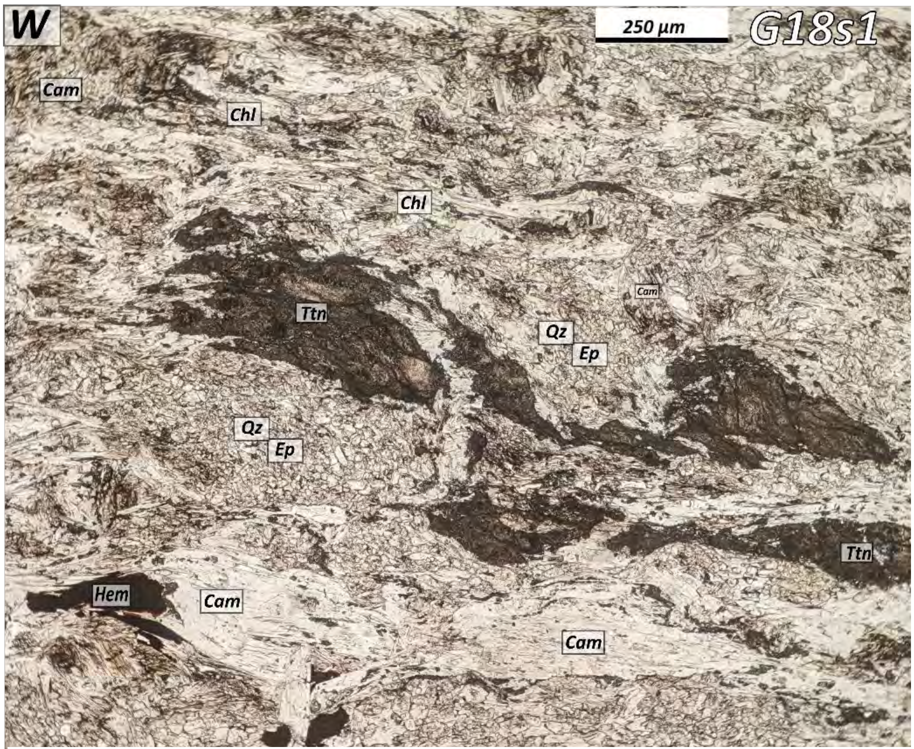

Figure 7 showing a foliation of elongated calcic-amphiboles, chlorite and titinite porphyroblasts. Rhombic calcic-amphiboles are situated as rotated grains amongst fine-grained epidote and quartz.

G35s

- **Lithology**: Metagabbro
- **Field measurements: 46°25’06.75”N, 09°35’23.06”E.** Intermediately Deformed,
    - Stretching lineation trend = 320W
- **Hand sample:** Fine grained whiteish-green rock with laminated layers and visible crystals.
- **Mineralogy:** Ep, Pl, Chl, Cam, Qz, Wm, Tlc, Hem and minor Aug.
- **Texture:**
    - The thin section is separated into a low-strain matrix containing rotated crystals of Ep, Cam and Aug, and a well-defined foliation consisting of Chl, Tlc, elongated Cam and Wm. Ep is replacing Pl and exists as inclusions within Pl and Cam. The asymmetry of shear bands and Chl-strain-shadows of rotated grains reflect a top-W shear sense (figure 8). Furthermore, Augite crystals and rhombic Cam display a disequilibrium by being rimmed by Tlc and Chl.
    - **Sense of shear: Top-W**
- **Sequence summary:**
    - Pre deformational growth of rhombic Cam, Pl and Aug.
    - Syn deformational growth of Tlc, Chl and Wm.
    - Post deformational growth are not clearly defined.

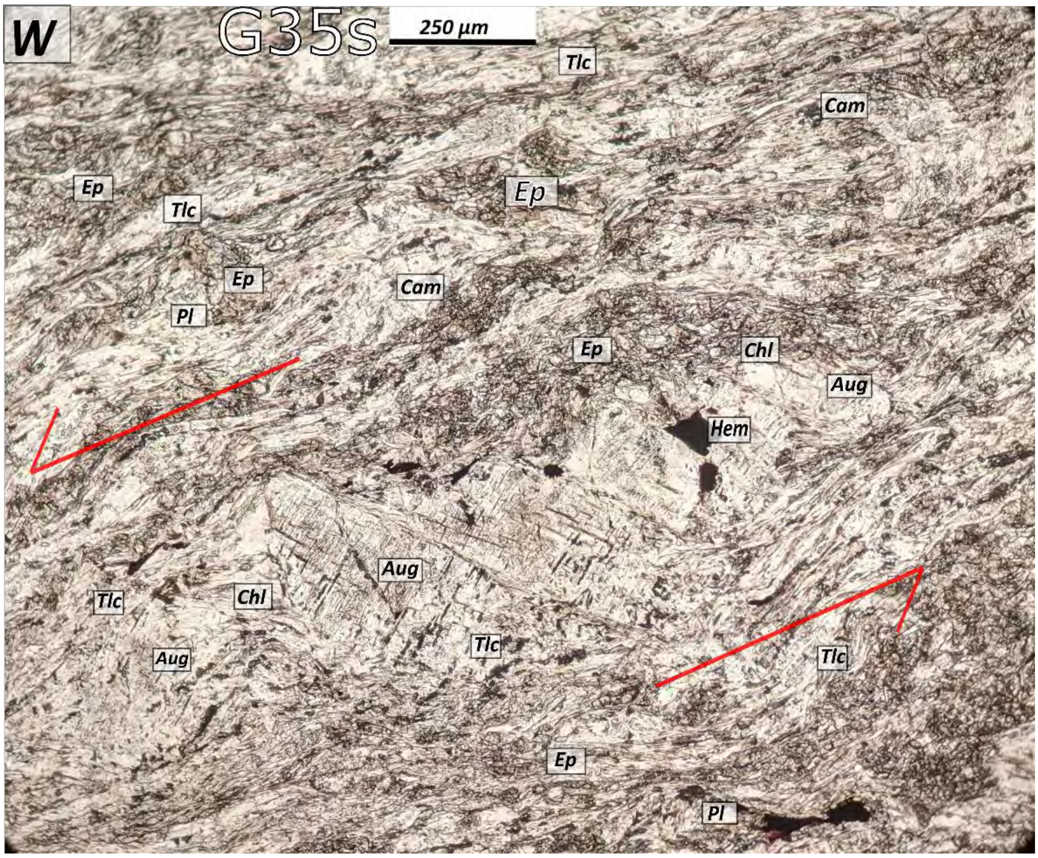

Figure 8. G35s foliation planes are defined by talc, and chlorite rich. Here, augite is displaying a disequilibrium and a sinistral shear-sense with talc and chlorite growing in its cracks.

G39s

- **Lithology**: Metagabbro
- **Field measurements: 46°25’10.13”N, 09°35’25.2”E.** Highly Deformed.
    - Stretching lineation trend = 296W.
- **Hand Sample**: Pitted weathering, laminated foliation green to greenish-yellow. Porphyroblasts are visible in hand sample.
- **Mineralogy:** Cam, Ep, Qz, Pl, Chl, Tlc and Wm
- **Texture:**
    - A well-defined foliation of Chl, elongated Cam, and minor Tlc growing in a matrix of Ep and Qz. Porhyroclastic Pl and porphyroblastic Cam are showing a top-W asymmetry with Chl growing in the strain shadows (figure 9). This is also observed in small grains of Ep and elongated Cam. Ep is growing as inclusions of Pl, and some Ep grains are in the form of Pl-aggregates, indicating a reaction texture.
    - **Sense of shear: Top-W**
- **Sequence summary:**
    - Igneous relics are Pl.
    - Pre deformational growth of rhombic Cam and Pl.
    - Syn deformational growth of Tlc, Ttn, elongated Cam, Qz, Wm and Chl.
    - Post deformational growth of Ep.

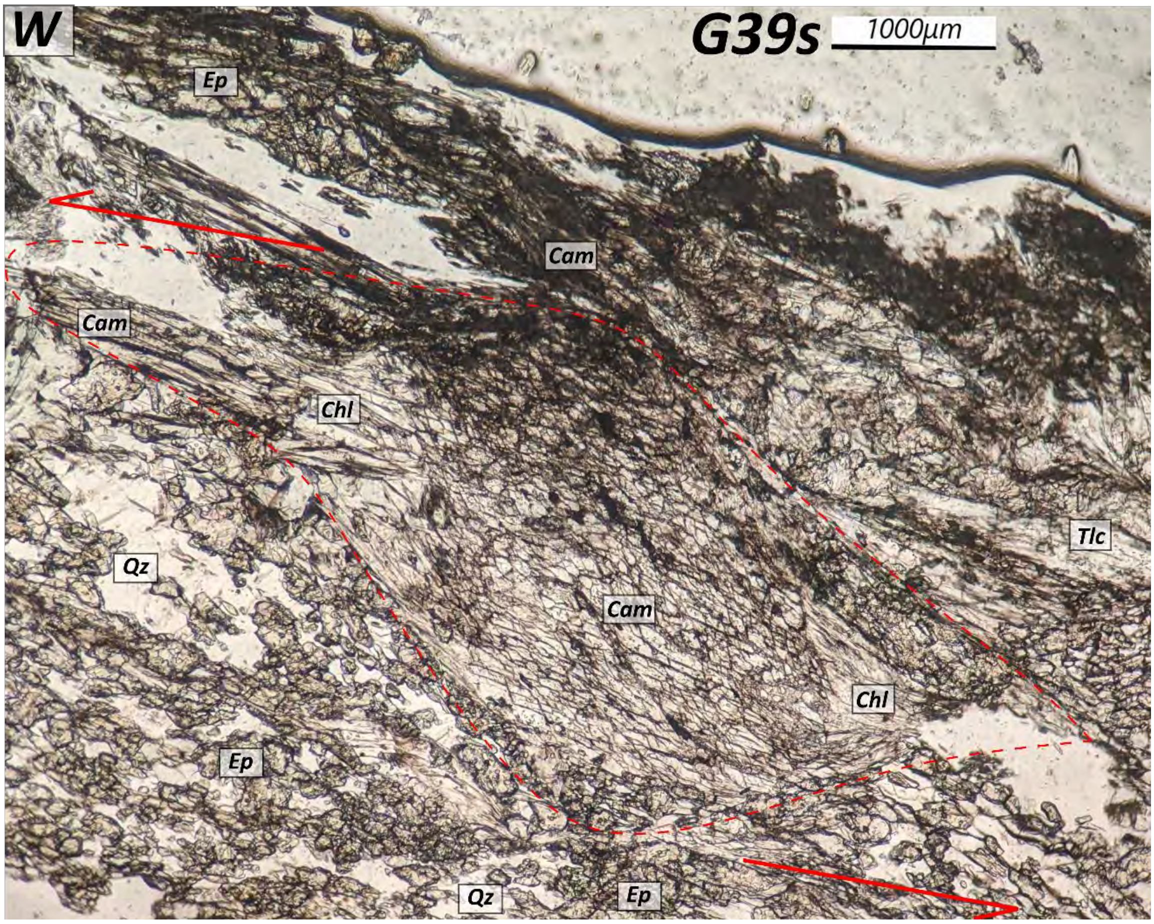

Figure 9. A porphyroblastic Calcic-amphibole crystal are displaying a top-W shear-sense.

G41s

- **Lithology**: Metagabbro
- **Field measurements: 46°25'11.78"N, 09°35'23.79"E.** Mylonitic texture.
    - **S**tretching lineation trend = 330W
- **Hand Sample:** A white mylonitic rock with finely laminated whiteish-green layers interlayered clusters of white layers.
- **Mineralogy:** Pl, Ep, Cam, Tlc, Chl, Qz, and minor Ttn.
- **Texture:** Mylonitic
    - The thin section consists of the fine-grained foliation of Chl and Tlc, separating fine-grained Ep and Qz layers. The fine-grained Ep is pale-pleochroic with a blue-birefringence and is observed as inclusions with larger crystals of amphibole and is observed in the shape of Pl-aggregates. Hence, reaction Pl → Ep must almost have gone into completion. Fine-grained Ep and Chl form top-W asymmetrical shear bands around Cam, and Cam also reflects a disequilibrium being partly replaced by Tlc and Chl. Some talc crystals are in the shape of rhombic-calcic-amphiboles, displaying a top-W asymmetry (figure 10).
    - **Sense of shear: Top-W**
- **Sequence summary:**
    - Igneous relics are not clear.
    - Pre deformational growth Cam and Pl.
    - Syn deformational growth fine-grained Ep, Tlc, Chl, Ttn, elongated Cam, and Qz.
    - Post deformational growth is not clearly defined.

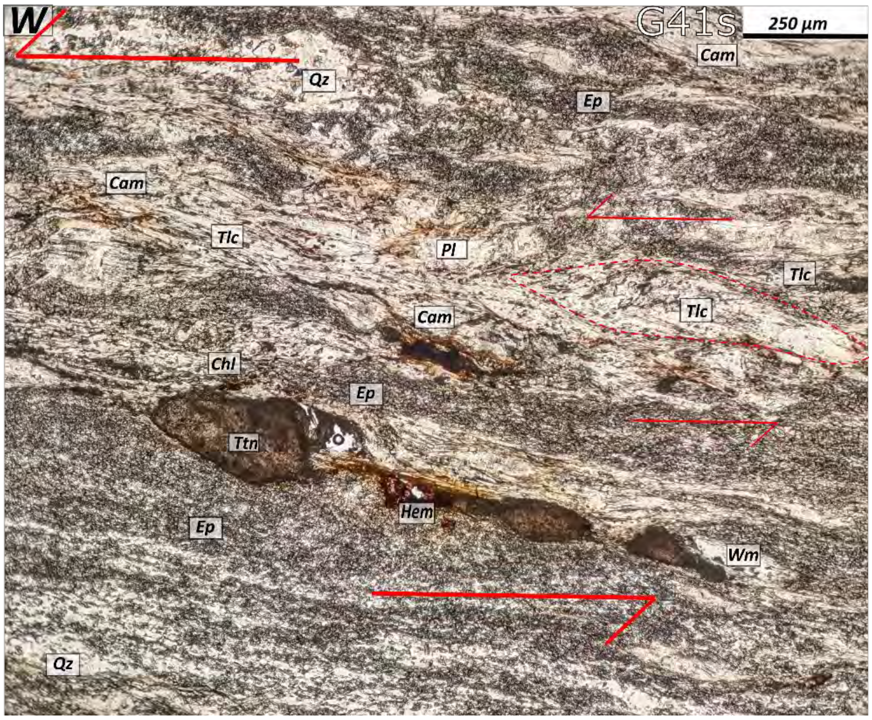

Figure 10 shows a talc-rich layer with titanite and calcic-amphibole; sheared in sinistrally top-W.

G46s

- **Lithology**: Metagabbro
- **Field measurements: 46°25’07.87”N, 09°35’43.58”E.** Mylonitic texture.
    - Stretching lineation trend = 308W
- **Hand sample:** A white mylonitic rock with a vague hint of a greenish-yellow sheen, accompanied by mm large black Fe-oxide crystals.
- **Mineralogy:** Chl, Hem, Ep, Wm, Tlc, and minor Cam.
- **Texture:** Mylonitic
    - The entire thin section comprises tight foliation planes of fine-grained Ep, Tlc, Chl with minor Wm. Within these planes, there are zoned epidote crystals (higher birefringence in the core), Pl-aggregates (replaced by fine-grained Ep, (figure 11), and aggregates of rhombic Cam; now consisting of a core of Hem rimmed by Chl. Pl and Qz clusters are sheared into asymmetrical shapes, indicating top-W movement. These larger crystals show a sinistral top-W asymmetry with Chl growing in the strain shadows.
    - **Sense of shear: Top-W**
- **Sequence summary:**
    - Igneous relics are not clear.
    - Pre deformational growth of Cam and Pl.
    - Syn deformational growth Ep, Chl, Tlc, and minor Wm.
    - Post deformational growth of Ep.

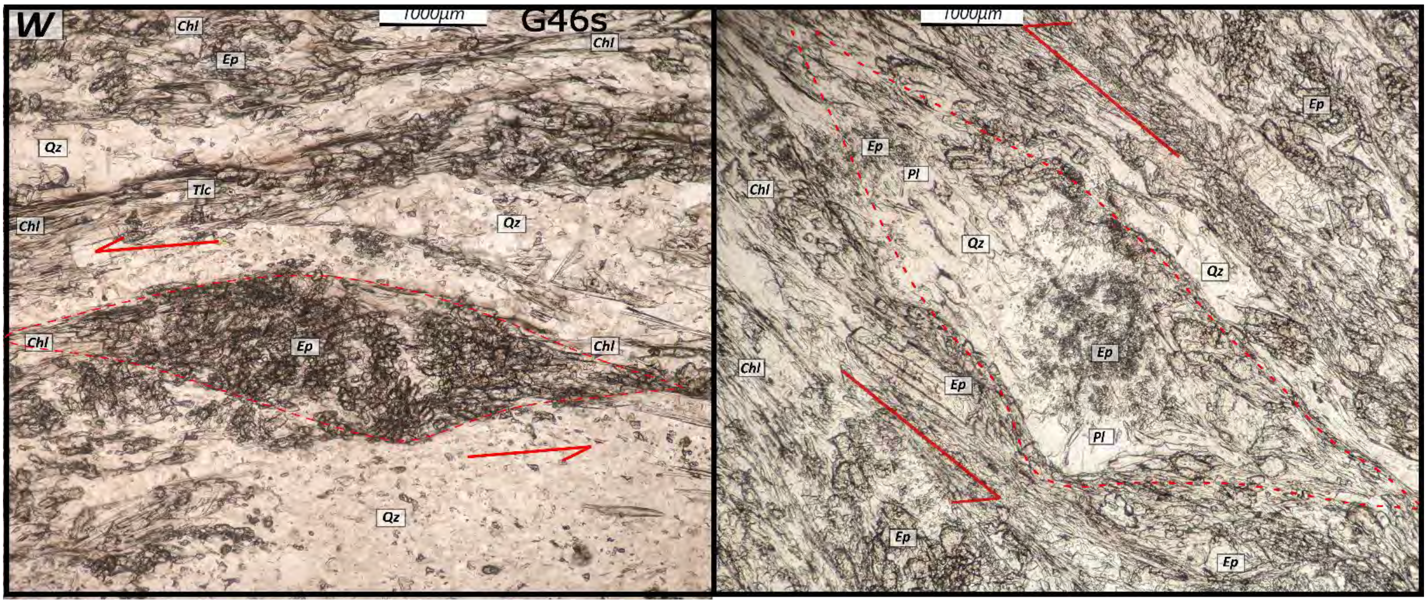

Figure 11 showing a Top-W sheared out plagioclase aggregate, now completly replaced by fine-grained Ep, with Chl growing in the strain shadows.

G68s

- **Lithology**: Metagabbro
- **Field measurements: 46°24’50.76”N, 09°35’18.25”E.** Highly Deformed.
    - Stretching lineation trend = 290W
- **Hand Sample:** Whitish mylonitic laminated rock with turquoise layers and some visible crystals.
- **Mineralogy:** Pl, Cam, Chl, Tlc, Ep, Wm and Ttn
- **Texture:** Mylonitic
    - The deformation is concentrated in thick mylonitic shear bands comprising Tlc, Chl, and Wm, with rotated porphyroblastic layers. The porphyroblasts of Cam and rectangular Ep display a top-to-the-W asymmetry with Chl and Tlc growing in strain shadows. Larger asymmetrical clusters of Tlc with Ep-inclusions and elongated albites are growing in the high strain Chl-layers, reflecting a top-to-the-W shear-sense (figure 12). Anheadral Pl-crystals with pale-pleochroic Ep inclusions form discontinued layers together with Q and Ep clusters; these are then broken up by Tlc + Chl shear bands – reflecting a top-W shear-sense. The majority of Ep is growing without a preferred orientation.
    - **Sense of shear: Top-W**
- **Sequence summary:**
    - Igneous relics are not clear.
    - Pre deformational growth of Pl, Qz, Cam and porphyroblastic Ep.
    - Syn deformational growth Chl, Wm, Tlc and Ttn.
    - Post deformational growth of Ep.

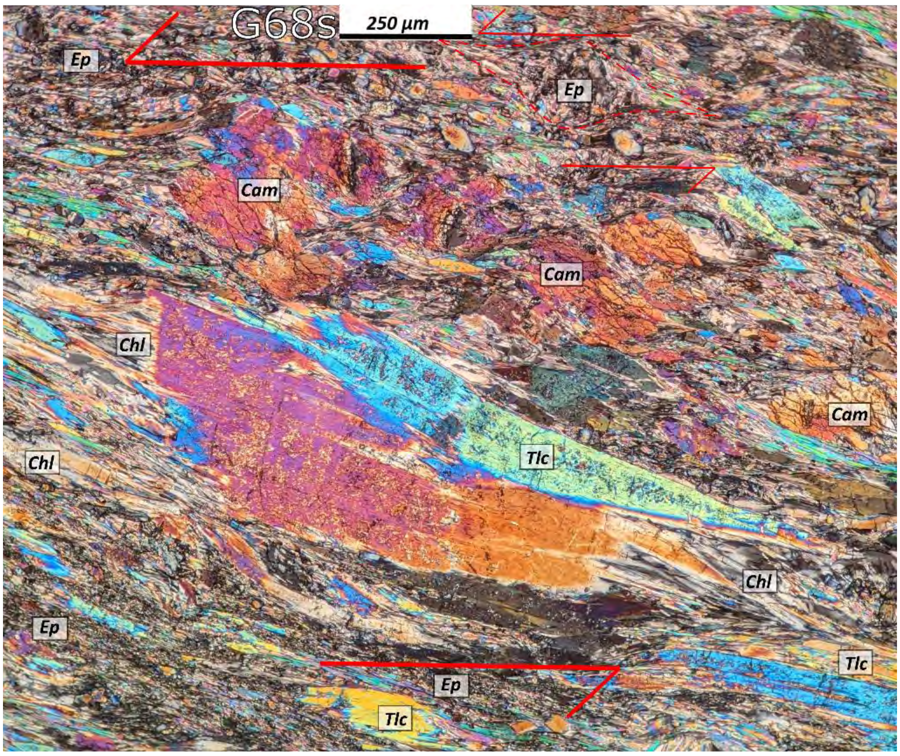

Figure 12 shows a talc-cluster reflecting a top-W asymmetry with chlorite growing in the strain shadows. Calcic-amphiboles are also reflecting top-W movement.

G89s

- **Lithology**: Metagabbro
- **Field measurements: 46°24'59.76"N, 09°35'44.02"E.** Highly Deformed.
  - Stretching lineation trend = 310W
- **Hand sample:** Laminated foliation, yellowish-green layers alternating with white quartz bands.
- **Mineralogy:** Ep, Pl, Qz, Tlc, Chl, Cam, and Ttn.
- **Texture:** Highly deformed rock with the primary deformation concentrated into high strain layers.
  - Qz + Pl-bands are discontinuous as they are broken up by Wm + Chl + ep shear bands, reflecting a top-to-the-W shear-sense. Larger crystals of Ep are in the form of Pl-aggregates with little-to-no Pl left. High strain layers consist of fine-grained, blue-birefringent Ep, Tlc, Chl and minor Wm. A brittle fault is cataclastically breaking up quartz bands, with sinistral displacement – associated with talc growth. Asymmetrical top-W folding is pervasive throughout the thin section (figure 13).
  - **Sense of shear: Top-W**.
- **Sequence summary:**
  - Igneous relics are not clear.
  - Pre deformational growth of Pl, Qz and Cam.
  - Syn deformational growth of Ep, Tlc, Chl, Ttn and Wm.
  - `Post deformational growth of Ep.

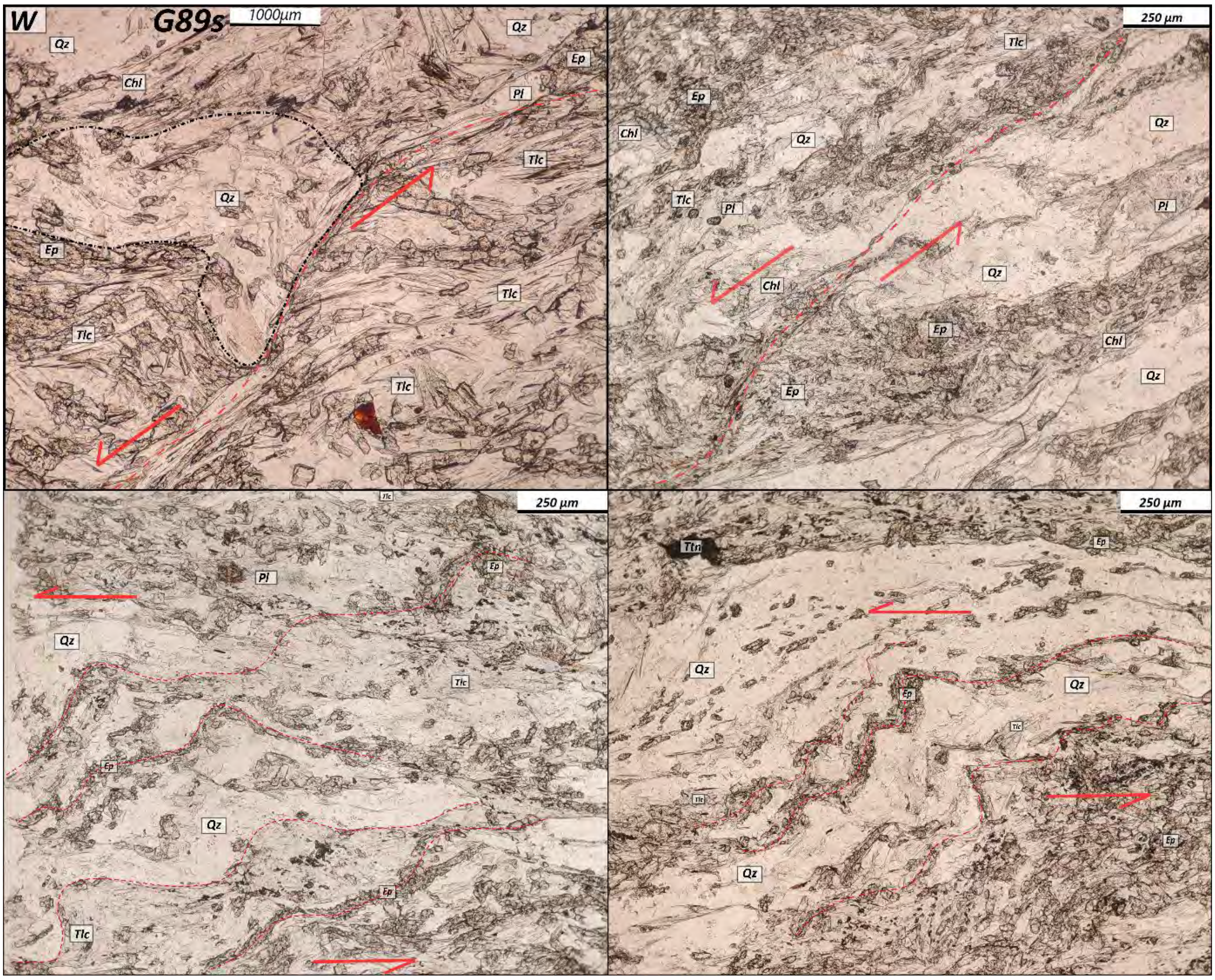

Figure 13 showing quartz bands being broken up by a sinistral normal fault. The faulting is associated with plastic talc-growth.

G98s

- **Lithology**: Metagabbro
- **Field measurements: 46°25'13.37"N, 09°35'17.93"E.** Mylonitic texture.
    - Stretching lineation trend = 290W
- **Hand Sample:** Mylonitic lamination, thinly layered white rock with a greenish hint to it.
- **Mineralogy:** Ep, Qz, Chl, Tlc, Cam, Pl, and minor Wm
- **Texture:** Mylonitic
    - Strain is concentrated in layers comprising Chl and fine-grained Ep, which flows with the foliation. There are larger crystals of elongated pale-pleochroic Ep, elongated Cam, and Tlc-clusters within these layers, indicating a top-W asymmetry. The high-strain layers are separated by Q-bands, which are broken up by shear bands of Wm and Tlc growth. Fine-grained Ep reflects an andalose-blue birefringence and has replaced most of the Pl observed. Furthermore, rhombic Cam shows an equilibrium by being replaced by Chl and Tlc.
- **Sequence summary:**
    - Igneous relics is not clear.
    - Pre deformational growth of Pl, Qz, Cam.
    - Syn deformational growth of Ep, Chl, Tlc and Wm.
    - Post deformational growth of Ep.

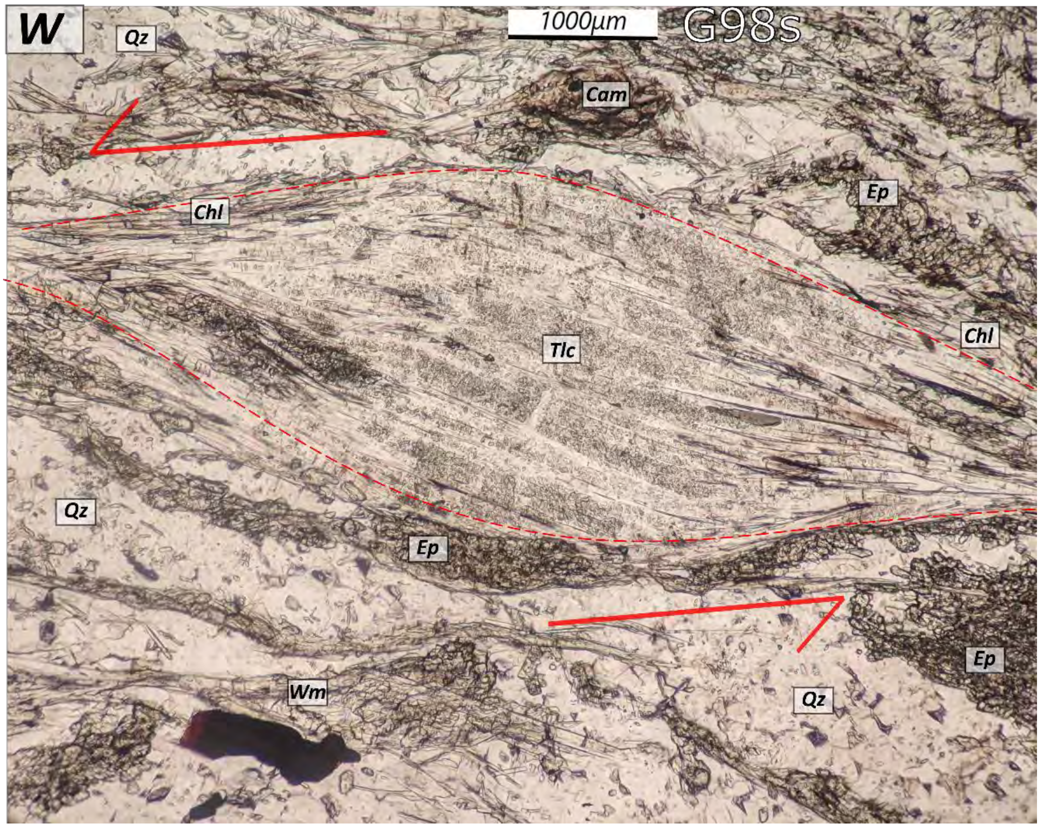

Figure 14 showing a asymmetrically sheared talc cluster – indicating top-W movement.

G101s

- **Lithology**: Metagabbro
- **Field measurements: 46°25’13.88”N, 09°35’12.25”E.** Intermediately Deformed.
    - Stretching lineation trend = 310W
- **Hand Sample:** A massive, roughly undeformed rock, sitting within the mylonite, with a whitish lustre to its otherwise green appearance.
- **Mineralogy:** Cal, Ttn, Pl, Wm, Chl, and Ep
- **Texture:** Intermediately deformed
    - The rock encompasses a foliation consisting of Wm and chlorite. Pl-crystals are either rimmed or fully replaced by Cal. No shear-sense-indicators are observed. Porphyroblastic Ttn are observed.
- **Sequence summary:**
    - Igneous relics of Alb and Mg-hbl
    - Pre deformational growth
    - Syn deformational growth of Ti, Wm, Ccl
    - Post deformational growth of Ca, Ep

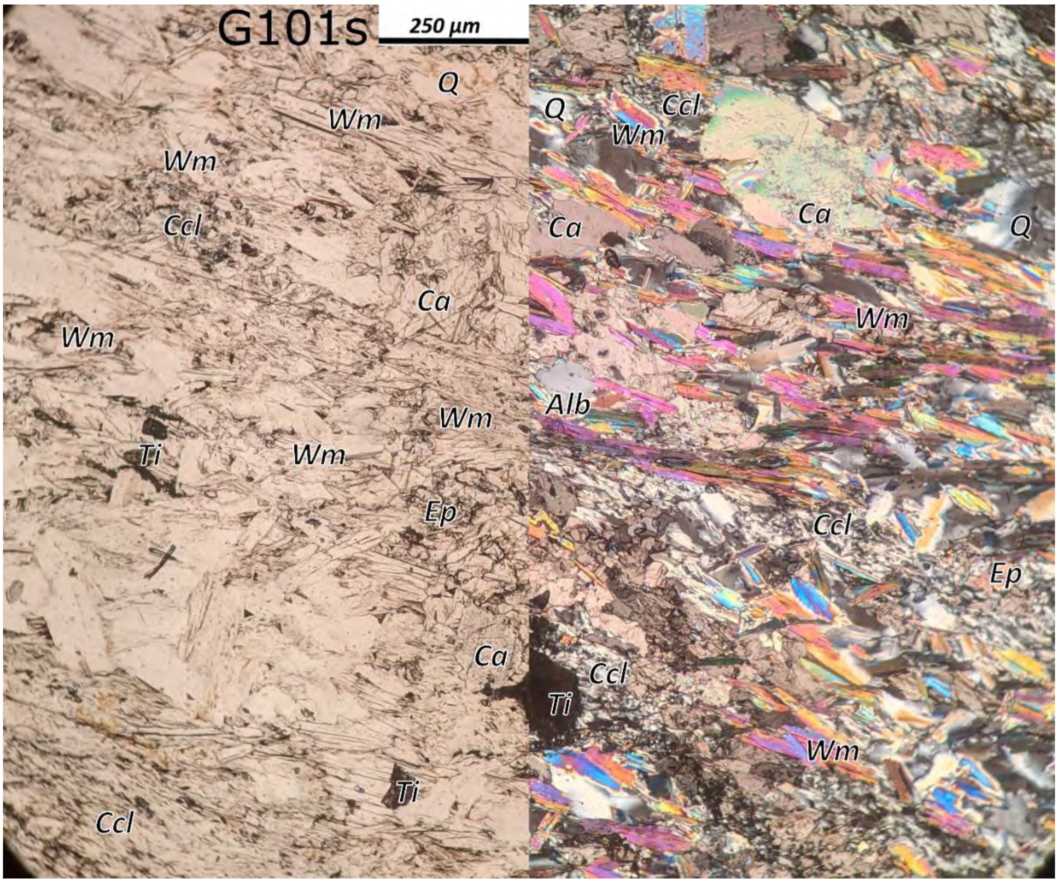

Figure 15 showing the general mineralogy of G101s.

20/5

- **Lithology**: Metagabbro
- **Field measurements**: **46 25 00 N, 9 35 26 E.** Top-W asymmetry.
- **Hand Sample:** A green rock with clusters and layers of quartz. Clear but coarse foliation.
    - Stretching lineation trend: 281W
- **Mineralogy:** Pl, Qz, Ep, and Chl.
- **Texture:** Highly deformed with relicts of poikilitic texture
    - The rock is layered into a highly deformed regime consisting of Qz-bands and Chl. These are separated by a thicker layer of Ep-Chl-Pl showing igneous poikilitic textures. Pl-crystals have inclusions of Ep, with Chl + Ep growing in a matrix. The texture resembles Pl's cumulate growth, with a mafic interstitial melt, now being Chl.
- **Sequence summary:**
    - Igneous relicts: Pl.
    - Syn deformational growth of Qz and Chl.
    - Post deformational growth was not observed.

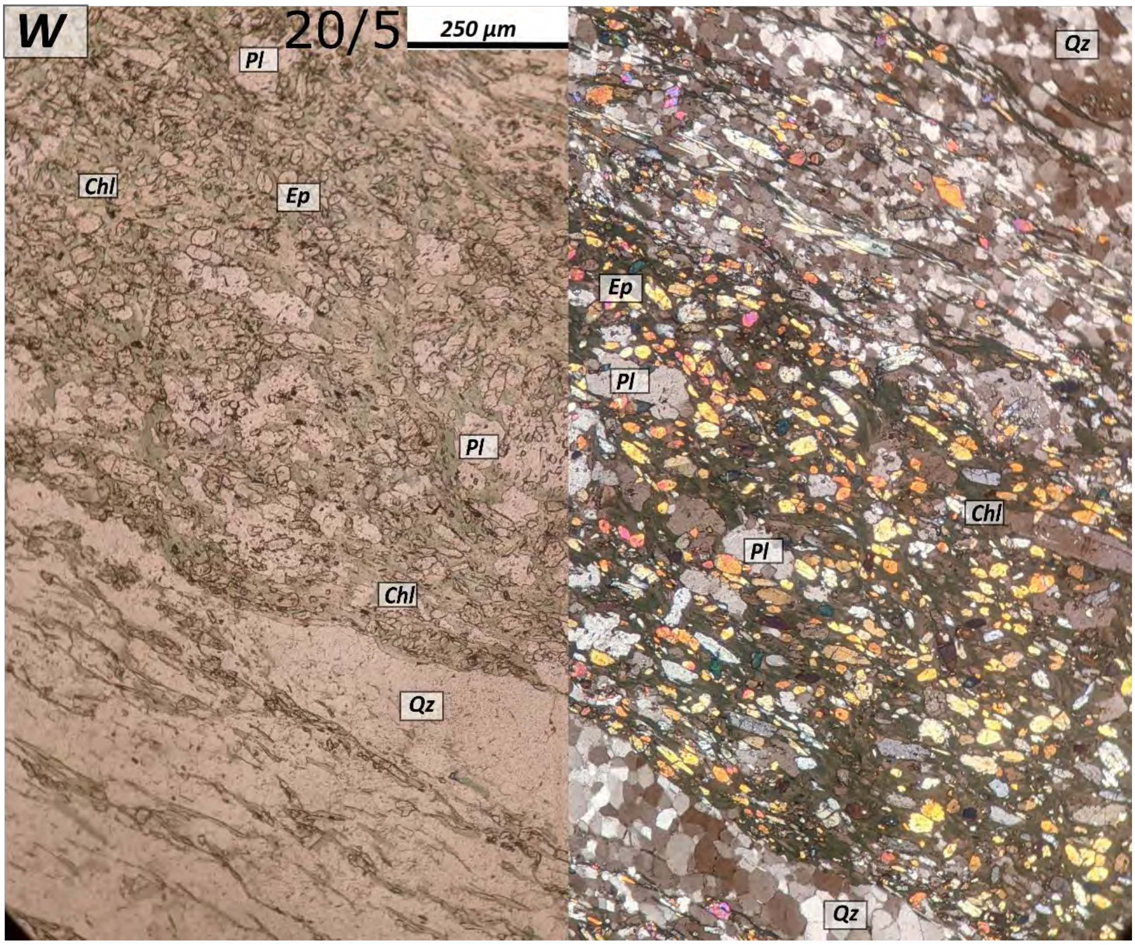

Figure 16 showing the general mineralogy of Ep-Chl-Pl-Qz

20/3

- **Lithology**: Metagabbro
- **Field Measurements**: 46°25'10.9"N 9°35'31.4"E. Mylonitic texture.
    - Stretching lineation trend: 272W
- **Hand Sample:** Mylonitic rock with lamination with green to white layers.
- **Mineralogy:** Cam, Pl, Ep, Qz and Chl
- **Texture:** Mylonitic
    - The thin section comprises layers of elongated Ep, asymmetrically stretched Cam and Pl with strain shadows of Chl – indicating top-W movement (figure 17). High-strain layers of Tlc, Chl and Pl, are flowing between asymmetrical Qz-bands, indicating top-W shearing. There are also Cam and Pl-crystals between these high strain layers that are rotated to 30° from the foliation.
- **Sequence summary:**
    - Pre deformational growth of Pl, Cam.
    - Syn deformational growth of Tlc, Chl, and Ep.
    - Post deformational growth not observed.

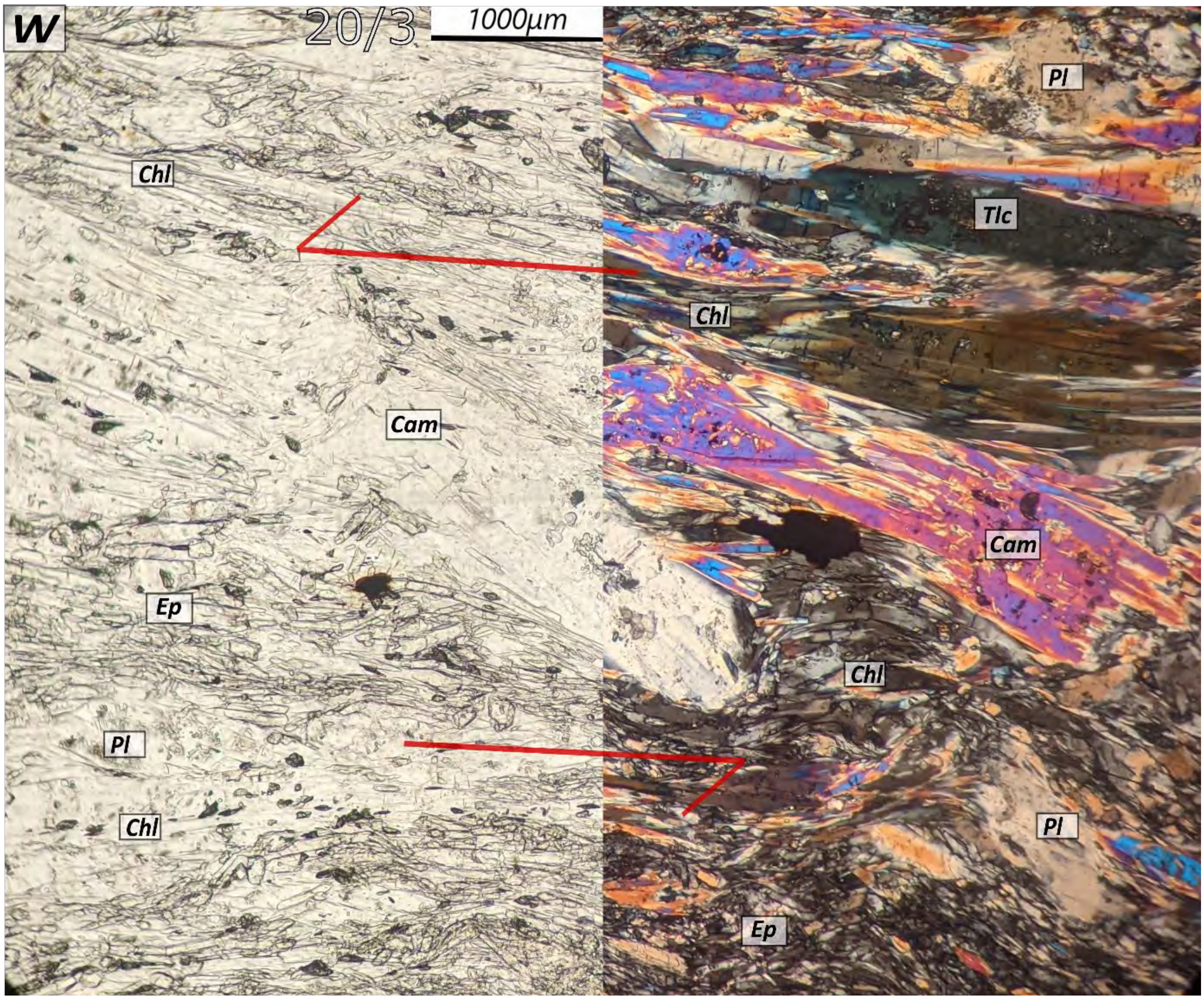

Figure 17. Showing asymmetrically top-to-the-W sheared calcic-amphibole, and plagioclase aggregates.

20/1

- **Lithology**: Metagabbro
- **Field measurement: 46°25'10.9"N 9°35'34.2"E.** Top-W asymmetry.
    - Stretching lineation trend: 291W
- **Hand Sample:** Mylonitic rock with lamination of green and white layers with large calcite clusters connected to it.
- **Mineralogy:** Cam, Pl, Ep, Qz, Ttn, and Chl.
- **Texture:** Mylonitic
    - The thin section comprises layers of Ep interlayered with asymmetrically stretched Cam and Pl with strain shadows of Ccl indicating top-W movement. Some prismatic rhombic Cam-crystals accompany these. Highly stretched layers of Tlc and Chl incorporate elongated Pl and thin Qz-bands. Shear senses are somewhat conflicting between layers; however, most are sinistral, top-W.
- **Sequence summary:**
    - Pre deformational growth of Pl, elongated Cam and rhombic Cam.
    - Syn deformational growth of Tlc, Chl and Ep.
    - Post deformational growth not observed.

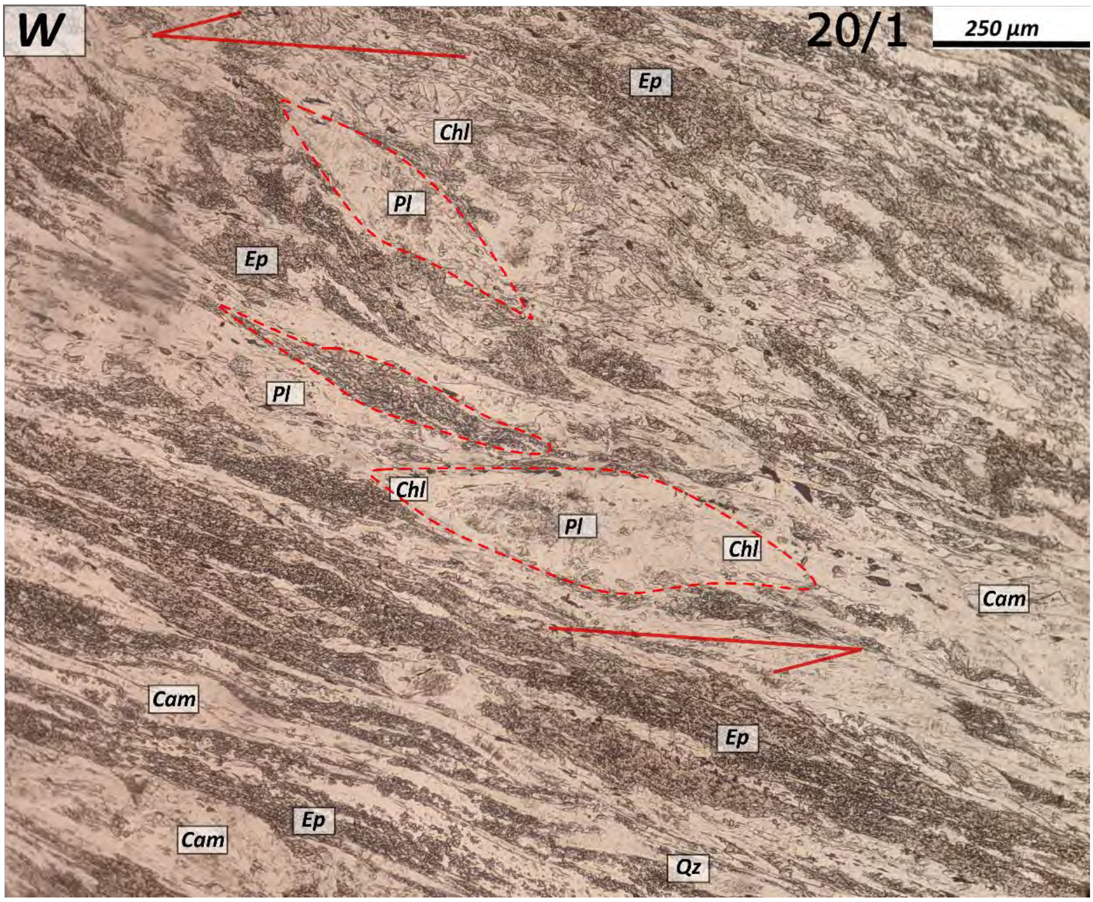

Figure 18 shows asymmetrical clusters of Pl-aggregates with Chl strain shadows.

20/11

- **Lithology**: Metagabbro
- **Field measurements**: 46°25'09.7"N 9°35'05.5"E. Top-W shear bands
    - Stretching lineation trend = 272W
- **Hand Sample:** A white mylonitic rock with thinly laminated layers of green and white.
- **Mineralogy:** Cam, Pl, Ep, Qz and Chl with minor carbonate located in a thin cross-cutting vein.
- **Texture:** Mylonitic
    - Fine-grained Qz, Ep and Chl form a high strain fabric between larger Cam, Tlc and Pl crystals. Pl-aggregates are sheared symmetrically, whereas Qz-clusters and Cam show a conflicting shear sense with Chl growing in the strain shadows (figure 19).
    - **Sense of shear:** A confident sense of movement cannot be determined.
- **Sequence summary:**
    - Pre deformational growth of Pl, elongated Cam and rhombic Cam.
    - Syn deformational growth of Tlc, Chl and Ep
    - Post deformational growth of carbonate.

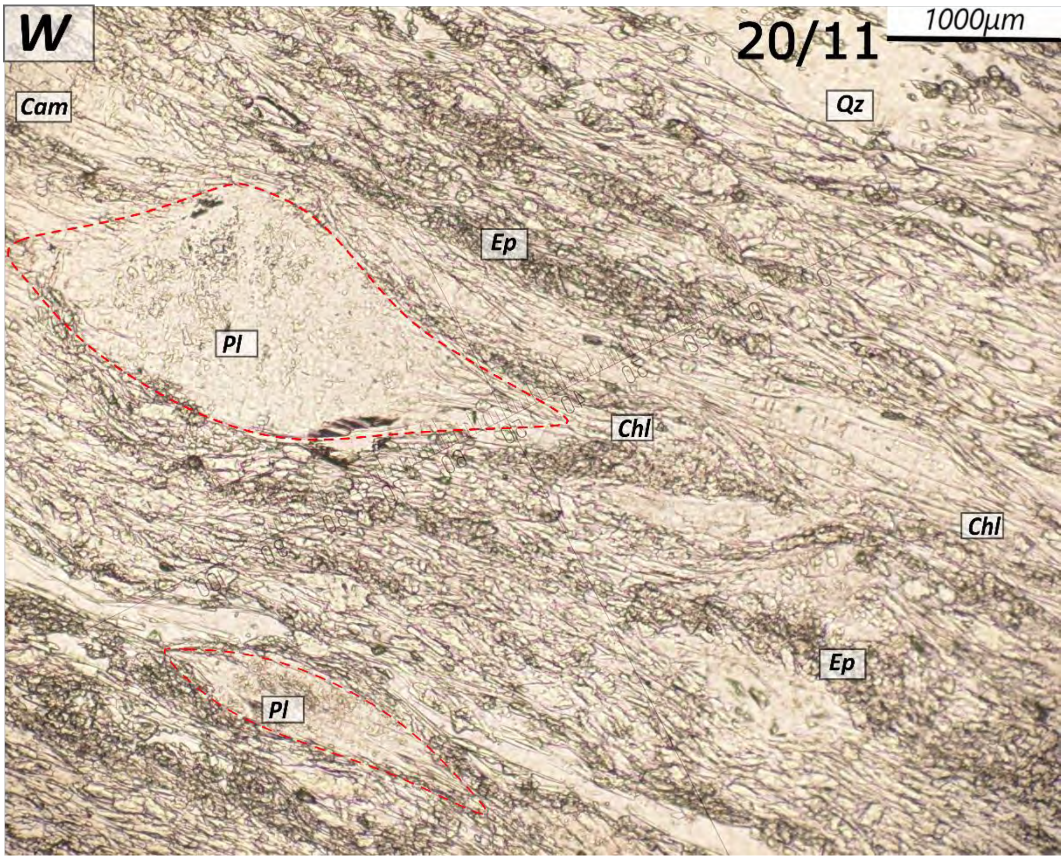

Figure 19 showing symmetrically sheared plagioclase aggregates.

20/9

- **Lithology**: Metagabbro
- **Hand Sample:** A white mylonitic rock with thinly laminated layers of green and white.
- **Field measurements:** 46°25'09.0"N 9°35'00.1"E. Top-W sheared carbonate boudins.
    - Stretching lineation trend = 283W
- **Mineralogy:** Cal, Qz, Pl, Ep, Wm, Tlc, Chl, and Ttn.
- **Texture:** Mylonitic
    - Fine-grained Qz + Pl-bands, in which Cal replaces Pl frequently. High strain layers of micaceous Tlc, Chl and Wm grow in between and split the bands into clusters with conflicting shear sense. There is no simple preferred shear sense due to some of the Qz + Pl bands being completely symmetrical; however, in the thickest micaceous high strain layer, both larger Pl and Qz bands are sheared sinistrally (figure 20).
- **Sequence summary:**
    - Pre deformational growth of Pl and Ep
    - Syn deformational growth of Tlc, Wm, Cal, Chl and Qz
    - Post deformation growth is not observed.

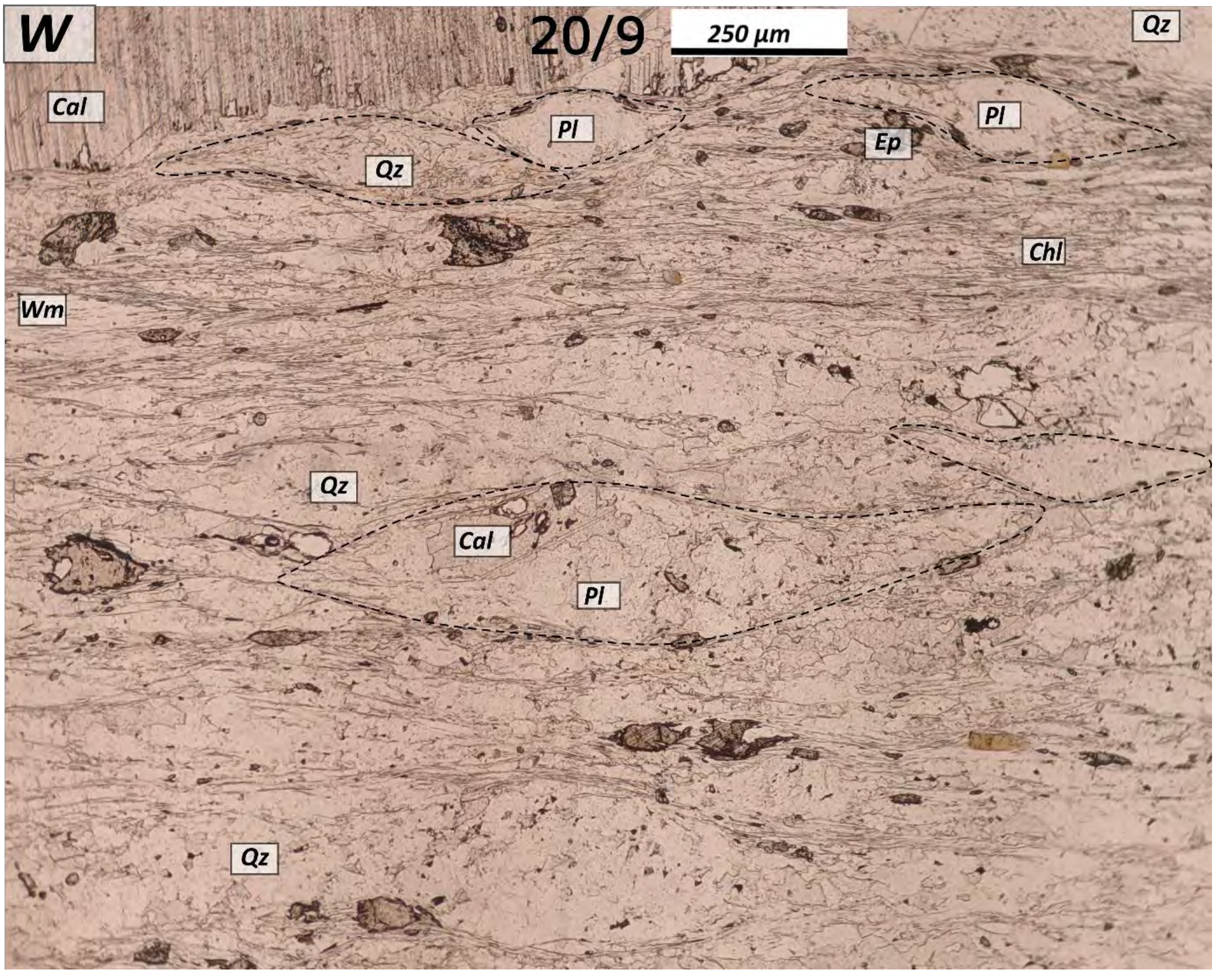

Figure 20 showing symmetrical Alb + Qz-bands with only Pl-aggregates in a Chl-rich layer indicating a top-W asymmetry.

UG

- **Lithology**: Metagabbro
- **Hand sample**: A massive green rock with a spotted yellowish-green colour throughout and coarse quartz.
- **Field measurements: 46°24'59.5"N 9°35'30.1"E.** Weakly-to-undeformed.
- **Mineralogy:** Cam, Ep, Cal, Pl, Chl, Ttn, and Qz.
- **Texture:** Undeformed.
    - The rock exhibits a poikilitic texture with Pl-crystals with Ep inclusions. Most Pl is getting replaced by Cal and Ep. Two different Cam are observed: Green-pleochroic fibrous actinolitic amphibole and rhombic-amphiboles with well-defined cleavage planes interpreted as magnesio-hornblende. An early foliation is observed consisting of green-pleochroic Chl and fibrous amphiboles. Porphyroblastic Ep reflects a yellow pleochroism.
- **Sequence summary:**
    - Igneous relics are rhombic Cam and Pl.
    - Syn deformational growth of fibrous amphibole and Chl.
    - Post deformational growth was not observed.

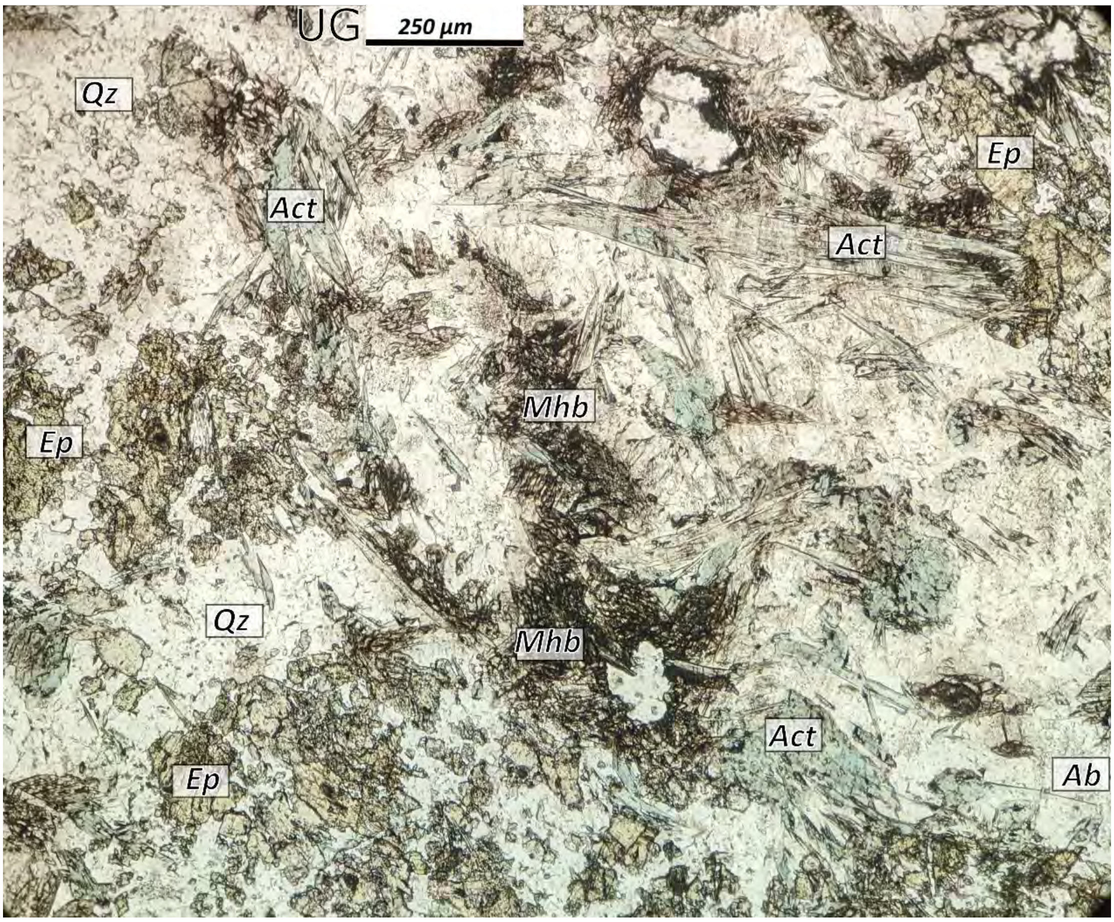

Figure 21 showing two dinstinctly different calcic-amphiboles: Rhombic magnesio-hornblende (Mhb), and green-pleochroic fibrous actinolitic amphibole (Act).

UG1

- **Lithology**: Metagabbro
- **Field measurements:** Weakly-to-undeformed.
- **Hand sample: 46°24'57.15"N, 09°35'28.55"E.** It is a massive green rock with a spotted yellowish-green tone and a green wave foliation.
- **Mineralogy:** Ep, Ep, Tlc, Cam, Aug and Chl
- **Texture:** Coarse-grained with a thick but visible foliation.
    - Porphyroclastic Aug-crystals display a distinct disequilibrium texture by being rimmed by Cam and internally replaced by Tlc and Chl (figure 22). The reaction products Tlc and Chl are the main constituents of the foliation. Fine-grained Ep-Qz is growing – making up the matrix of the rock. Ep replaces Porphyroclastic Pl. Furthermore, Augite shows an exsolution lamellae with Calcic-amphibole + Chl growing within its cleavage planes.
- **Sequence summary:**
    - Igneous relics of Aug and Pl.
    - Pre deformational growth of rhombic Cam.
    - Syn deformational growth of Elongated fibrous Cam, Chl, Tlc and Ep.
    - Post deformational growth of Ep.

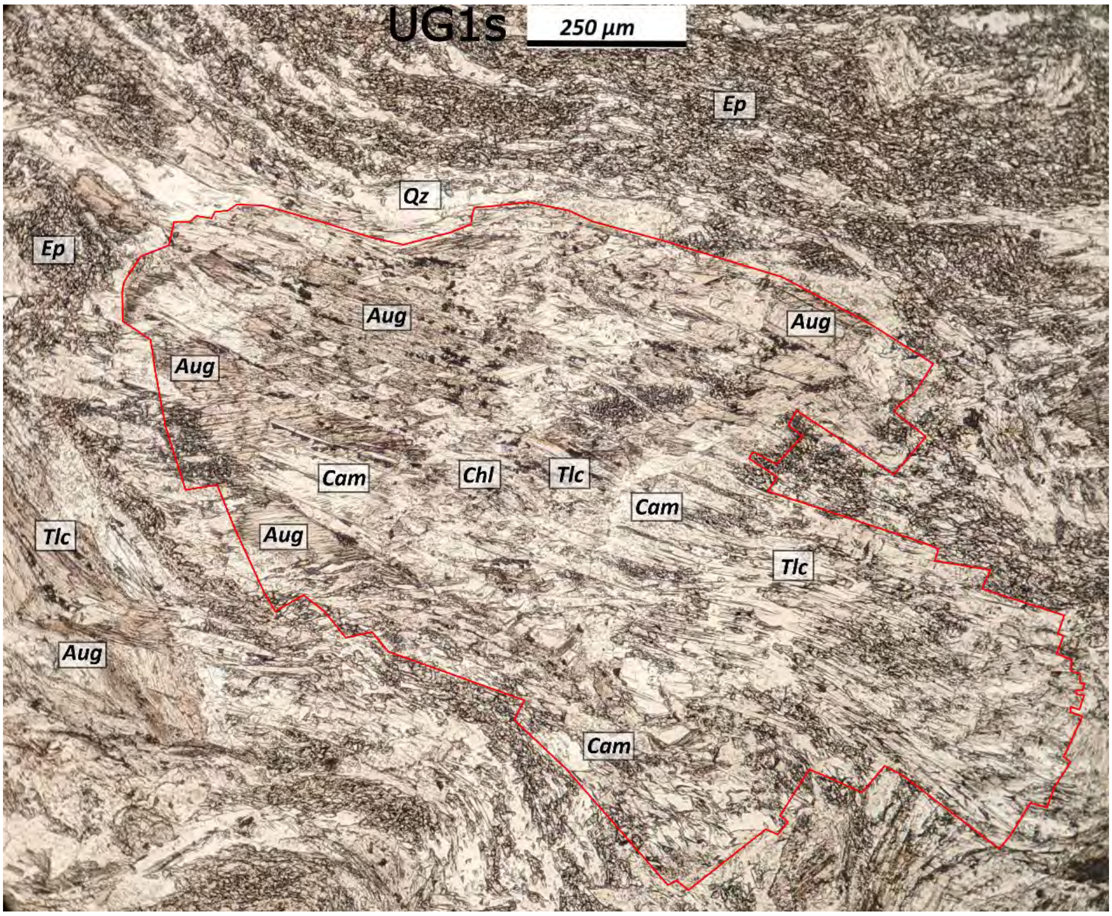

Figure 22 showing the disequilibrium of a porphyroclastic augite crystal – being replaced by Tlc + Chl + Cam.

MB1

- **Lithology**: Meta volcanoclastic rock
- **Field measurements: 46°24'58.41"N, 09°35'25.37"E -** sampled from an anticlinal fold hinge.
  - Stretching lineation trend = 92E.
- **Mineralogy:** Cal, Ep, Pl, Rbk, Chl and Ttn.
- **Texture:**
  - Blue-to-purple pleochroic amphiboles with a weak-1st-order birefringence are interpreted as Riebeckite. The Riebeckites are rimmed by green-pleochroic Chl, which makes up the principal foliation planes (figure 23). Yellow-pleochroic porphyroblastic Ep is elongated with the foliation. This foliation divides layers Cal, Ep, Wm, Ttn and minor Qz with Cal replacing Pl-crystals.
- **Sequence summary:**
  - Pre deformational growth of Ep.
  - Syn deformational growth of Chl, Rbk and Ttn.
  - Post deformational growth of Cal.

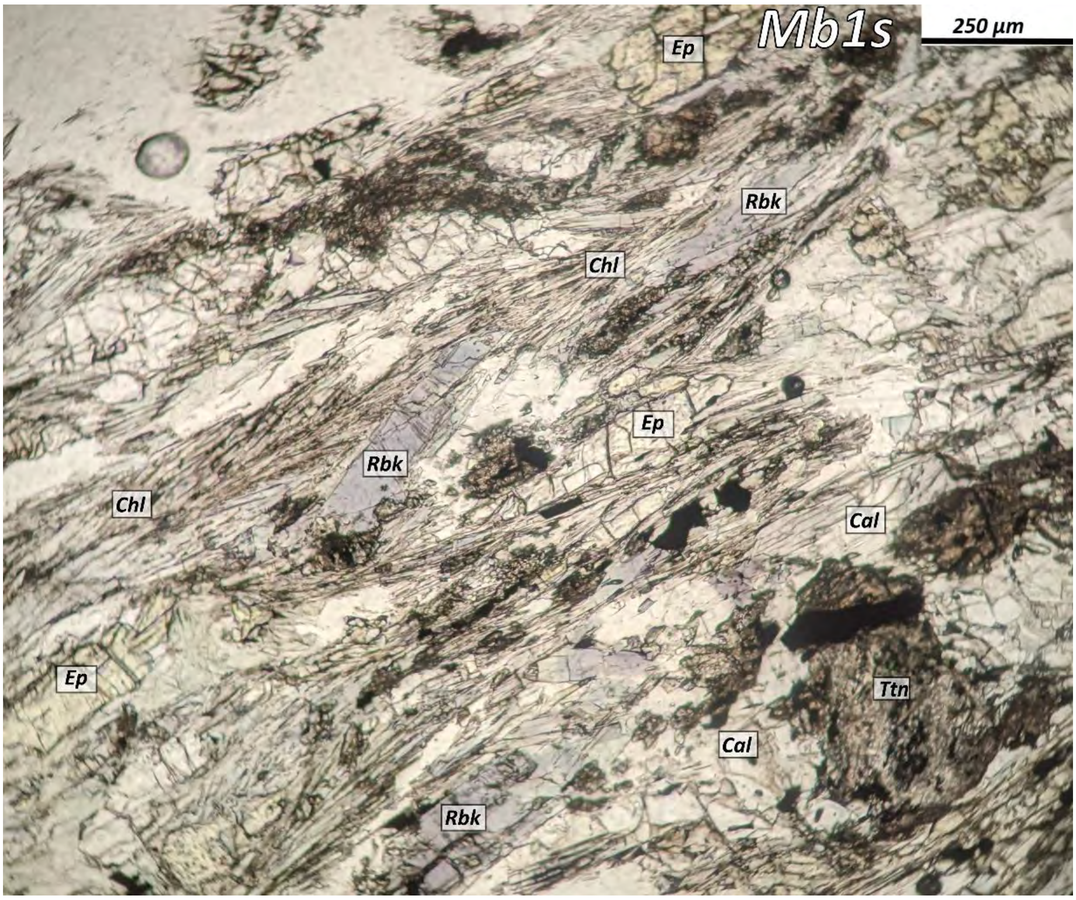

Figure 23 showing the mineralogy of the meta volcanoclastic layer with blue-pleochroic riebeckite rimmed by green-pleochroic chlorite.

MB2

- **Lithology**: Meta volcanoclastic rock
- **Field measurements: 46°24’59”N, 09°35’25.92”E.**
    - Stretching lineation trend = 290W
- **Hand sample:** A fine-grained blue look with a clear foliation, cut through green layers.
- **Mineralogy:** This rock is compositionally layered; thus, respective layers are described separately.
    - Blueschist: Pl, Rbk, Wm, Qz, and Cal with minor Chl and Hem.
    - Greenschist: Chl, Ep, Pl, Ttn and Hem.
- **Texture:**
    - The rock comprises centimetre-thick blue layers, cut by millimetre-thick green-clearly foliated layers. The blue layer comprises a foliation of blue-to-purple pleochroic Rbk, accompanied by Wm and Chl. Rbk is also observed as a rhombic crystal shape. This foliation is cutting through asymmetrically sheared Qz-Pl aggregates with a top-W sense of movement (figure 24). Cal replaces some Pl-aggregates.
    - The border between the green layer and the blue comprises elongated Hem crystals. These also make up a large volume in the main foliation consisting of Chl with rotated Ep, elongated Pl and Ttn. Minor Rbk is observed as elongated and rhombic crystals within the foliation; however, these are often rimmed by Chl. Rotated grains of Ep, Pl and Hem are showing an asymmetry to the west, with Chl growing in the strain shadows (figure 24).
- **Sequence summary:**
    - Pre deformational growth of Albite and Q
    - Syn deformational growth
        - Phase 1: Na-amphiboles
    - Phase 2: Cl, Ti and EpPost deformational growth of Py and Ep

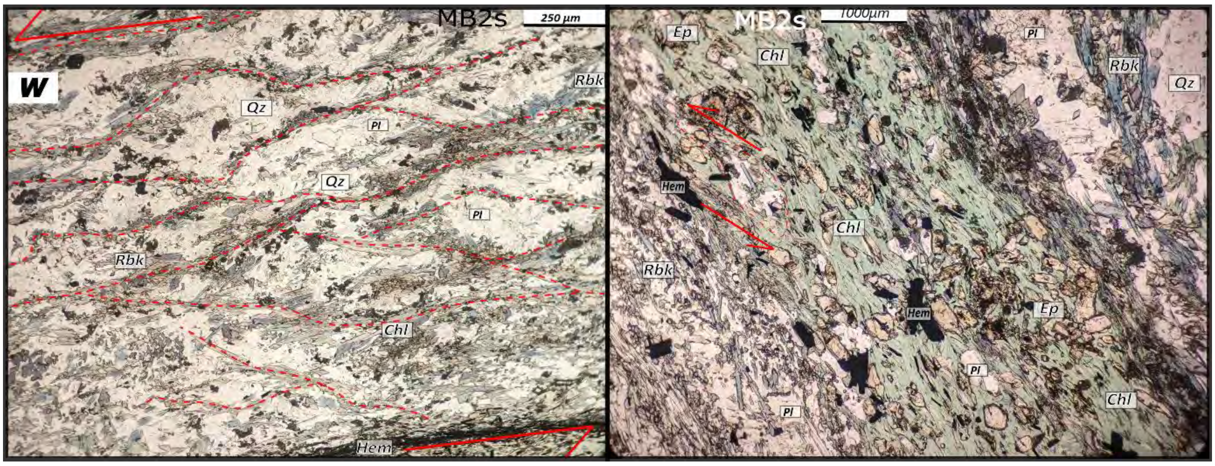

Figure 24 showing the blue-layer to the left, and the green layer to the right. Note that the scales are different.

20/8

- **Lithology**: Calcareous schist
- **Field measurements**: 46°25'14.9"N 9°35'15.2"E. Top-W carbonate boudins.
    - Stretching lineation trend = 267W
- **Mineralogy:** Cal, Qz, Wm, Chl, Pl, and Hem
- **Texture:** Mylonitic
    - The calcschist comprises a thin micaceous foliation of Chl + Wm with asymmetrically sheared Pl-aggregates and Qz-clusters with Chl as strain shadows, indicating a top-W movement. The primary foliation is separated by layers of Qz + Pl, where Cal replaces most Pl.
    - Pre deformational growth of porphyroblastic Pl-crystals.
    - Syn deformational growth of Chl, Wm, Qz, and Cal.
    - Post deformational growth of Hem.

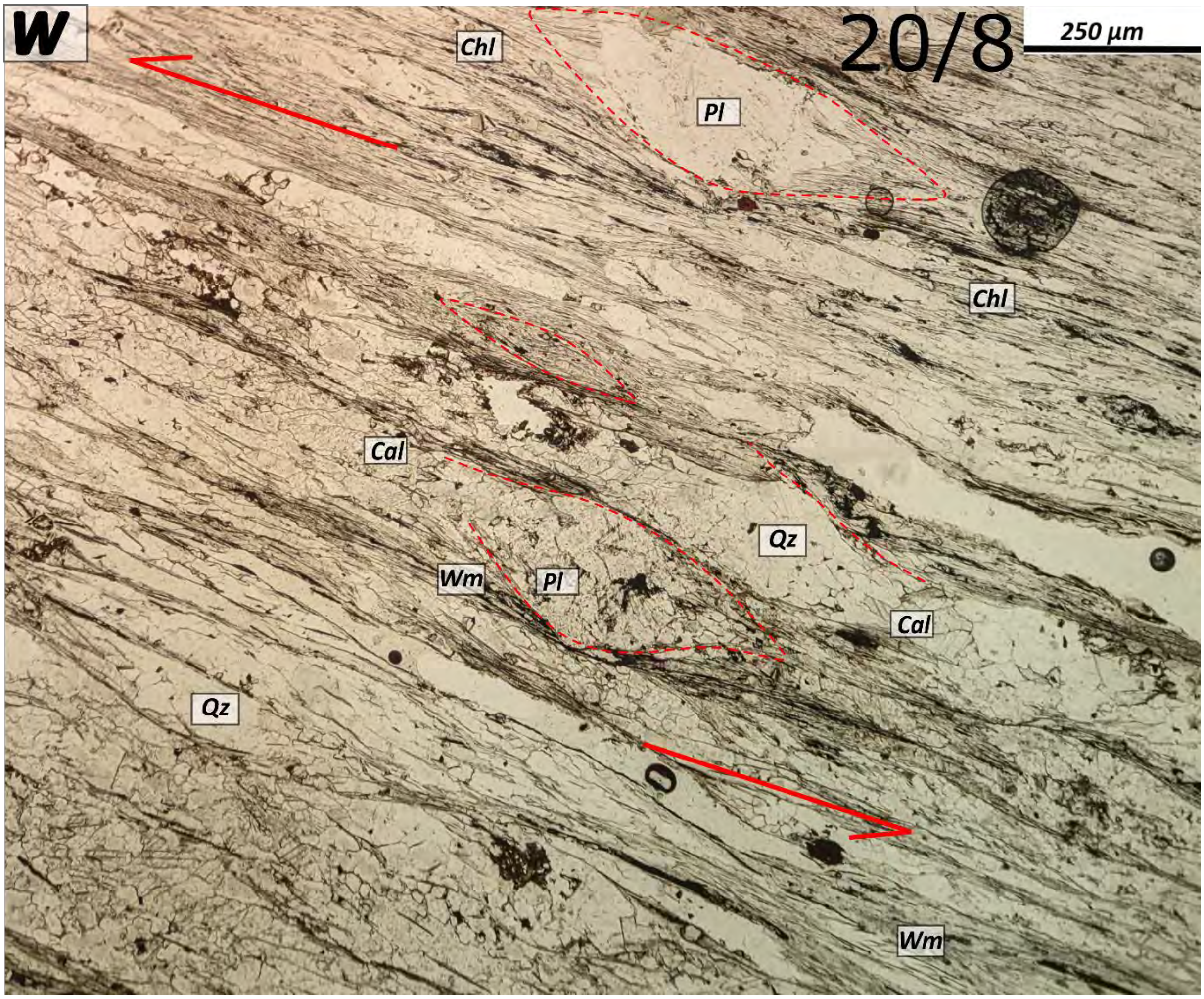

Figure 25 showing asymmetrical Pl and Qz-aggregates within the calcschist.

B15

- **Lithology**: Chlorite schist
- **Field measurements: 46°24'56.51"N, 09°35'22.94"E.** Asymmetrical carbonate boudins indicate top-W movement.
    - Stretching lineation trend = 260 W
- **Hand sample:** Green, finely foliated schist with clusters of quartz.
- **Mineralogy:** Chl, Qz, Wm, Tur, Ep with minor Ttn and Pl.
- **Texture:** Mylonitic
    - The chlorite schist comprises green-pleochroic Chl almost exclusively. The foliation is highly sheared with asymmetrical clusters of Chl and Wm, indicating top-W movement (figure 26). This foliation covers the entire thin section except for an area comprising Qz-bands. Fine-grained epidote and turmaline grow all over the thin section with no preferential orientation.
- **Sequence summary:**
    - Pre deformational growth is not clear
    - Syn deformational growth of Chl, Wm, Qz, and Ti
    - Post deformational growth of Ep

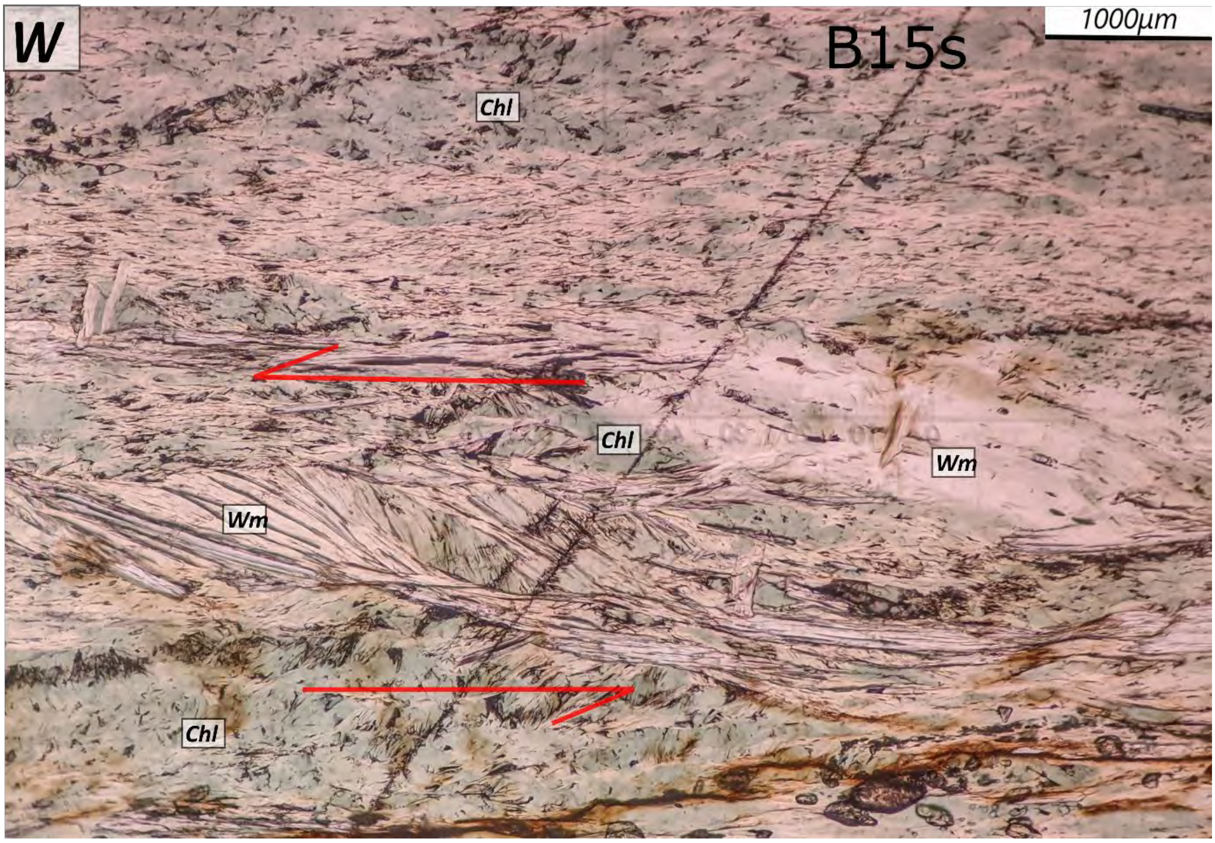

Figure 26 showing an asymmetrical Wm-cluster within the chlorite-schist.